Hannes Hinterbichler, BSc

An experimental investigation on ternary liquid drop collisions

MASTERARBEIT

zur Erlangung des akademischen Grades

Diplom-Ingenieur

Masterstudium Maschinenbau

eingereicht an der

Technischen Universität Graz

Betreuer

Univ.-Prof. Dr.-Ing. habil. Günter Brenn
Institut für Strömungslehre und Wärmeübertragung

Dr. Carole Planchette (Zweitbetreuerin)
Research Center Pharmaceutical Engineering GmbH

Graz, April 2015

EIDESSTATTLICHE ERKLÄRUNG
AFFIDAVIT

Ich erkläre an Eides statt, dass ich die vorliegende Arbeit selbstständig verfasst, andere als die angegebenen Quellen/Hilfsmittel nicht benutzt, und die den benutzten Quellen wörtlich und inhaltlich entnommenen Stellen als solche kenntlich gemacht habe. Das in TUGRAZonline hochgeladene Textdokument ist mit der vorliegenden Masterarbeit identisch.

I declare that I habe authored this thesis independently, that I have not used other than the declared sources/resources, and that I have explicitly indicated all material which has been quoted either literally or by content from the sources used. The text document uploaded to TUGRAZonline is identical to the present master's thesis.

Datum / Date	Unterschrift / Signature

Acknowledgement

The present investigation on binary and ternary liquid drop collisions has been performed between May 2014 and April 2015 at the Institute of Fluid Mechanics and Heat Transfer at Graz University of Technology. The research was funded by the Research Center Pharmaceutical Engineering GmbH.

First of all, I would like to express my gratitude to my advisor Prof. Dr.-Ing Günter Brenn for providing me the interesting topic of this work and for the excellent supervision of this thesis.

Special thanks I want to address to my second advisor Dr. Carole Planchette for always taking time to debate on the thesis and for providing valuable scientific advice.

Furthermore, I gratefully thank the entire staff of the Institute of Fluid Mechanics and Heat Transfer, especially the staff of the workshop, for always bearing a helping hand.

Most importantly, I would like to express my special thanks to my parents Ulrike and Franz who supported me unconditionally during my studies. You made it possible.

Thank you!

Abstract

Binary liquid drop collisions have been studied extensively during the past decades. Initially because of meteorological interests and later on for the investigation of spray combustion. Recent studies have set the attention on binary drop collisions of two immiscible liquids. Thus, a wide range of applications is opened, for example at production processes in life sciences, such as encapsulating one liquid within another. In order to encapsulate additional liquids, collisions of more than two droplets may be performed. To date, there are no studies on this topic in the literature.

The current study aims to close the scientific gap in the literature by investigating ternary drop collisions, where all three droplets consist of the same liquid. The main goals are to examine the fundamental collision mechanisms occurring at ternary drop collisions and to identify differences and similarities to binary drop collisions. Therefore, collisions of two and three droplets are investigated experimentally at well-defined conditions, such as relative velocity and impact parameter. In addition, other relevant parameters like droplet diameter and dynamic viscosity are varied. On the one hand, similar to binary collisions, four main regimes are observed in the ternary case, namely coalescence, bouncing, reflexive separation and stretching separation. On the other hand, significant differences between binary and ternary drop collisions are observed, especially during the first period of the collision after the impact. Moreover, it is shown that the transition from coalescence to separation at ternary head-on collisions cannot be predicted by established binary collision models.

Kurzfassung

Binäre Tropfenkollisionen wurden in den vergangenen Jahrzehnten ausgiebig erforscht. Zunächst hauptsächlich wegen meteorologischer Interessen und später zur Beschreibung von Sprays in Verbrennungsanlagen. Aktuelle Studien untersuchen Kollisionen zweier Tropfen deren Flüssigkeiten nicht mischbar sind. Dies ermöglicht eine Vielzahl neuartiger Anwendungen, beispielsweise bei Produktionsprozessen in der Medizintechnik, wo durch Mikroverkapselung eine Flüssigkeit von einer Zweiten ummantelt wird. Um zusätzliche Flüssigkeiten einzukapseln können Kollisionen von mehr als zwei Tropfen eingesetzt werden. In der Literatur gibt es zu diesem Thema jedoch keinerlei Studien.

Die vorliegende Arbeit setzt sich zum Ziel, diese wissenschaftliche Lücke zu schließen. Dazu werden ternäre Tropfenkollisionen untersucht, wobei die Flüssigkeit bei allen drei Tropfen dieselbe ist. Ziel ist es, die grundlegenden Mechanismen von ternären Tropfenkollisionen zu erforschen und diese mit jenen von binären Kollisionen zu vergleichen. Dazu werden Kollisionen zweier und dreier Tropfen bei genau definierten Bedingungen, gegeben durch Relativgeschwindigkeit und Stoßparameter, experimentell untersucht. Weiters werden andere wichtige Parameter wie die Tropfengröße und die dynamische Viskosität der Flüssigkeit variiert. Auf der einen Seite werden, analog zu binären Kollisionen, bei ternären Tropfenkollisionen vier verschiedene Kollisionstypen beobachtet: Koaleszenz, Bouncing, reflexive Separation und streifende Separation. Andererseits werden signifikante Unterschiede zwischen binären und ternären Tropfenkollisionen aufgezeigt, insbesondere während der ersten Phase der Kollision direkt nach dem Aufprall. Außerdem wird gezeigt, dass der Übergang von Koaleszenz zu Separation bei frontalen ternären Kollisionen nicht mit Hilfe etablierter binärer Kollisionsmodelle dargestellt werden kann.

Contents

Nomenclature

Latin symbols

Symbol	Description	Dimension
A	droplet area in photograph	[px^2]
ΔA	error at estimation of the droplet area	[px^2]
b	impact parameter	[m]
d	diameter of a cylinder	[m]
D	droplet diameter	[m]
D_{max}	diameter of the disk at maximum extension	[m]
D_{or}	orifice diameter	[m]
E_{ini}	initial droplet energy	[J]
ΔE	change of surface energy	[J]
$\vec{f^B}$	specific body force vector	[m s^{-2}]
f	frequency	[Hz]
F	force	[N]
l	length of a cylinder	[m]
$\vec{l}$	length vector	[m]
L	length	[m]
p	pressure	[Pa]
Δp	Laplace pressure	[Pa]
R_1, R_2	principal radii of curvature	[m]
S	surface area	[m^2]
ΔS	change of surface area	[m^2]
$\hat{S}$	non-dimensional surface area	[−]

Symbol	Description	Dimension
t	time	[s]
T	temperature	[K]
u	flow velocity	$[\mathrm{m\,s^{-1}}]$
$\vec{u}$	velocity vector	$[\mathrm{m\,s^{-1}}]$
U	relative velocity or drop velocity	$[\mathrm{m\,s^{-1}}]$
U_J	jet velocity	$[\mathrm{m\,s^{-1}}]$
V	volume	$[\mathrm{m^3}]$
w	width of the disk at maximum extension	[m]
x, y, z	Cartesian coordinates	[m]
X	non-dimensional impact parameter	[−]

Greek symbols

Symbol	Description	Dimension
α	angle between trajectories	[rad]
$\hat{\alpha}$	dissipation coefficient	[−]
β, γ	angles	[rad]
δ	droplet size ratio	[−]
ϵ	empirical factor	[−]
ζ	aspect ratio of a cylinder	[−]
λ	wavelength	[m]
λ_{min}	minimum wavelength	[m]
λ_{opt}	optimum wavelength	[m]
ρ	density	$[\mathrm{kg\,m^{-3}}]$
σ	surface tension	$[\mathrm{N\,m^{-1}}]$
τ	viscous stress	[Pa]
ϕ	viscous dissipation function	$[\mathrm{kg\,m^{-1}\,s^{-3}}]$
Φ	viscous dissipation	[J]
$\vec{\nabla}$	vector of spatial derivatives	$[\mathrm{m^{-1}}]$

Subscripts

Symbol	Description
0	onset of fragmentation
c	coalescence
C	central droplet
L	left droplet
LC	between left and central droplet
m	centre of mass
PF	parameters according to Pasandideh-Fard *et al.* (1996)
R	right droplet
RC	between right and central droplet
s	separation
∞	characteristic quantity of the flow field

Superscripts

Symbol	Description
$()^*$	non-dimensionalised

Non-dimensional parameters

Symbol	Description	Definition
Oh	Ohnesorge number	$\mu\,(\rho\,\sigma L)^{-1/2}$
Re	Reynolds number	$\rho\,U D\,\mu^{-1}$
We	Weber number	$\rho\,U^2 D\,\sigma^{-1}$
We^*	transition Weber number	$We/48$

1 Introduction

Droplet collisions are a well investigated field of research for which earliest work dates back to the late 19th century (Rayleigh, 1896). Interest in meteorological phenomena, especially in the formation of precipitation, led to studies on binary water drop collisions in an atmospheric environment beginning in the 1960s (Montgomery, 1970; Brazier-Smith *et al.*, 1972; Ashgriz & Poo, 1990). In the last decade of the 20th century, focus has been set on the investigation of binary collisions of hydrocarbon droplets (Brenn & Frohn, 1989; Jiang *et al.*, 1992; Qian & Law, 1997), helping to understand the process of spray combustion. It has been shown that the collision outcome of water and hydrocarbon droplets differs fundamentally, as summarised in the work of Orme (1997). Later, studies with other liquids have been performed in order to determine the influence of viscosity on the droplet collision outcome (Willis & Orme, 2000; Willis & Orme, 2003; Gotaas *et al.*, 2007).

All studies mentioned above are limited to the case where the two colliding droplets are made of the same liquid. Recent studies have focused on the collision behaviour of two droplets consisting of two different, possibly immiscible, liquids (Gao *et al.*, 2005; Chen & Chen, 2006; Planchette *et al.*, 2010; Planchette *et al.*, 2012). There are several promising applications for drop collisions of immiscible liquids, for example, by encapsulating a liquid by another immiscible liquid, a protective shell can be generated preserving the core liquid and its ingredients. In order to increase the number of different liquids inside such a capsule, collisions of more than two droplets are required. All studies in the literature mainly consider binary drop collisions, except for the works of Saroka (2001) and Planchette (2011), where ternary drop collisions were investigated.

The current study aims to enlighten the scientific field of ternary drop collisions. To observe and understand the fundamental collision phenomena at ternary drop collisions, collisions of droplets consisting of the same liquid are investigated in this master's

thesis work. Afterwards, the collision outcomes observed for ternary drop collisions are compared to the ones for binary drop collisions. Moreover, the stability limit defining the transition between coalescence and separation at head-on collisions is investigated.

As a first step, the collision regime maps, where the collision outcome is classically represented as a function of the non-dimensional impact parameter and the Weber number, are obtained for binary and ternary drop collisions using a glycerol-water solution as the liquid at an average droplet diameter of 370 μm. Secondly, the stability limit for the transition between coalescence and separation at head-on collisions is investigated. Several parameters are varied: the droplet diameter ranges from 130 to 550 μm, the dynamic viscosity using several aqueous glycerol solutions at different concentrations and the surface tension using silicon oils. All the experiments are performed in an atmospheric environment at constant pressure and temperature. Finally, the results are interpreted and compared.

The structure of the thesis is as follow: In chapter 2, the fundamentals required to understand and describe drop collisions are presented. This includes the process of drop formation and an overview of the state of the art at binary droplet collisions. In addition, two separation criteria from the literature, describing the transition between coalescence and separation for head-on collisions, are introduced.

The used liquids and experimental configurations are presented in chapter 3. Moreover, the experimental set-up and the software used for image processing are introduced. Afterwards, the sought quantities like relative velocity U and non-dimensional impact parameter X are derived.

In chapter 4 the results are presented and discussed. Binary and ternary drop collisions are compared to each other as well as to results from the literature.

Modelling attempts are provided in chapter 5 in order to explain the experimental stability limits theoretically. For this purpose, the collision is divided into two periods, in the first phase the droplets collide and expand into a disk shaped complex while during the second phase, this disk retracts into a cylindrical shaped rod, which may break up. In addition, the use of a fragmentation criterion analogously to the work of Ashgriz & Poo, 1990 is evaluated.

A summary closes this work.

2 Fundamentals

Essential knowledge to understand and describe droplet collisions is provided in this chapter. First, general information is provided starting with basic fluid mechanic concepts and ending with a description of the different mechanisms of drop formation. We then focus on binary drop collision of the same liquid. More precisely, an insight into the collision outcome classification is given, followed by the presentation of two separation criteria determining the transition between coalescence and reflexive separation.

2.1 Theoretical background

2.1.1 Fluid properties

In order to describe liquid drop collisions at constant temperature and constant ambient pressure mathematically, three fluid properties, namely density ρ, dynamic viscosity μ and surface tension σ, are required. The latter two are defined below.

Dynamic viscosity

The dynamic viscosity μ is a fluid property, which defines its resistance against deformation. This phenomenon can be illustrated for shear stress by the idealized situation given in figure 2.1. The liquid is trapped between two parallel horizontal plates, separated by a distance H, where the one on the bottom is fixed and the one on the top is dragged by a force F and therefore moves at a constant velocity U. It is assumed that the flow is laminar and that there is no slip at the plates. Under

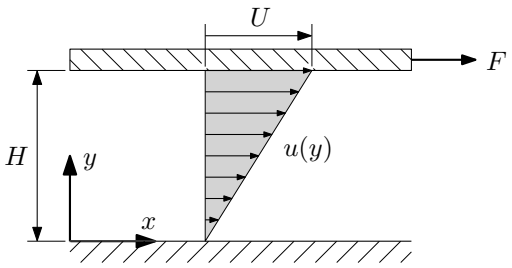

Figure 2.1: Shear strain between two parallel plates (adapted from Spurk & Aksel, 2007).

these conditions the liquid velocity u increases linearly between the two plates with $u(y = 0) = 0$ and $u(y = H) = U$, see figure 2.1. The shear stress is given by

$$\tau = \frac{F}{A} = \mu \frac{U}{H} = \mu \frac{\partial u}{\partial y}\,, \tag{2.1}$$

where A is the area of each plate, u the velocity of the fluid along x and y the coordinate normal to the plate (see figure 2.1). The proportionality factor μ is called dynamic viscosity with its physical unit $[\mathrm{kg\,m^{-1}\,s^{-1}}]$. For a Newtonian fluid μ is constant and not a function of $\partial u/\partial y$, whereas it may vary for non-Newtonian fluids. For liquids, the dynamic viscosity decreases with increasing temperature, whereas for gases, the dynamic viscosity increases with increasing temperature.

Surface tension

The phenomenon of surface tension takes place at the fluid interface, classically liquid/vapour, and can be explained by intermolecular interactions. On the one hand, a molecule in the bulk of the liquid is affected by cohesive forces, which are equal in all directions. Thus, the resulting net force is zero. On the other hand, a molecule at the interface does not have the same molecules on all sides of it leading to a net force

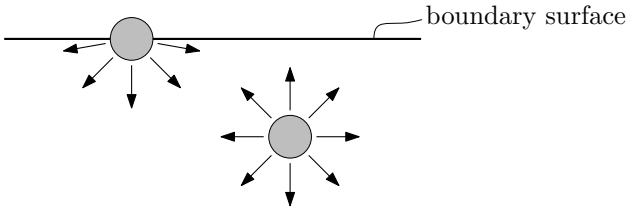

Figure 2.2: Schematic illustration of forces on molecules of a liquid (adapted from de Gennes *et al.*, 2004).

towards the centre of the liquid. This phenomenon is illustrated in figure 2.2, where a molecule at the interface and a molecule inside the liquid can be seen. The arrows represent the cohesive forces acting on the molecules.

In order to increase the liquid surface, energy has to be supplied to work against the inward-looking force. The required energy ΔE is proportional to the number of molecules that are moved to the surface and therefore to the additional surface area ΔS which leads to the following definition of surface tension:

$$\sigma = \lim_{\Delta S \to \infty} \frac{\Delta E}{\Delta S} \,. \tag{2.2}$$

It is usually expressed in units of $[\mathrm{N\,m^{-1}}]$, or sometimes of $[\mathrm{J\,m^{-2}}]$.

2.1.2 Dimensionless numbers

In this section, the three non-dimensional quantities relevant for the description of droplet collisions are defined.

Reynolds number

The Reynolds number can be derived by non-dimensionalising the incompressible Navier-Stokes equations, which read

$$\frac{\partial \vec{u}}{\partial t} + (\,\vec{u} \cdot \vec{\nabla}\,)\,\vec{u} = -\frac{1}{\rho}\vec{\nabla} p + \frac{\mu}{\rho}\vec{\nabla}^2 \vec{u} + \vec{f^B}\,, \tag{2.3}$$

where $\vec{u}$ is the velocity vector, p the pressure and $\vec{f^B}$ the specific body force vector. Denoting U_∞ and L a characteristic velocity and typical length scale of the flow field and introducing in equation (2.3) the following non-dimensional quantities

$$\vec{u}^* = \frac{\vec{u}}{U_\infty}\,, \quad t^* = \frac{t\,U_\infty}{L}\,, \quad \vec{\nabla}^* = L\vec{\nabla}\,, \quad p^* = \frac{p}{\rho\,U_\infty^2}\,, \quad \vec{f^B}^* = \frac{L}{U_\infty^2}\vec{f^B}\,, \tag{2.4}$$

we obtain the non-dimensional Navier-Stokes equations:

$$\frac{\partial \vec{u}^*}{\partial t^*} + (\,\vec{u}^* \cdot \vec{\nabla}^*\,)\,\vec{u}^* = -\vec{\nabla}^* p^* + \underbrace{\frac{\mu}{\rho U_\infty L}}_{Re^{-1}} \vec{\nabla}^{*^2} \vec{u}^* + \vec{f^B}^*\,. \tag{2.5}$$

Reynolds number, which can be found on the right hand side, is defined by

$$Re = \frac{\rho U_\infty L}{\mu}\,, \tag{2.6}$$

which can be interpreted as the ratio of inertial forces to viscous forces. Since we expect $Re \gg 1$ for droplet collisions (typically $100 < Re < 1000$), an inertial regime is assumed for non-dimensionalising time and pressure (see equation (2.4)). Assuming a viscous regime these quantities can be non-dimensionalised as follows:

$$t^* = \frac{t\,\mu}{\rho\,L^2}\,, \quad p^* = \frac{p\,L}{\mu\,U_\infty}\,. \tag{2.7}$$

In this case Re can be found in front of $(\,\vec{u}^* \cdot \vec{\nabla}^*\,)\,\vec{u}^*$ in equation (2.5).

Weber number

The Weber number represents a non-dimensional quantity, which can be interpreted as the ratio of inertial energy to surface energy. It is given by

$$We = \frac{\rho\,U_\infty^2\,L}{\sigma} = \frac{\rho\,U_\infty^2\,L^3}{\sigma L^2} = \frac{\text{inertial energy}}{\text{surface energy}}\,. \tag{2.8}$$

Ohnesorge number

The Ohnesorge number is a dimensionless group, which is important for the description of capillary systems with viscosity. It was discovered as relevant in the atomization of liquid jets (von Ohnesorge, 1936). It is defined by

$$Oh = \frac{\mu}{\sqrt{\rho\,\sigma L_\infty}} = \frac{\text{viscous forces}}{\sqrt{\text{inertia} \cdot \text{surface tension}}}\,. \tag{2.9}$$

2.1.3 Laplace pressure

Due to the effect of surface tension, a pressure difference exists between the inside and the outside of a curved interface (liquid/vapour), which is called the Laplace pressure. According to Laplace's theorem, this pressure difference Δp can be calculated as the

product of surface tension and the sum of principal curvatures of the interface, which leads to the Young-Laplace equation

$$\Delta p = \sigma \left(\frac{1}{R_1} + \frac{1}{R_2} \right) , \tag{2.10}$$

where R_1 and R_2 are the principal radii of curvature of the surface. For a plane interface the pressure difference vanishes, as R_1 and R_2 tend towards infinity.

2.2 Drop formation

In this section, several mechanisms of drop formation are briefly reviewed. The Rayleigh jet breakup mechanism is described in more detail, since it corresponds to the principle on which the drop generators used in this master's thesis work (Brenn *et al.*, 1996) are based.

In general, there are four mechanisms of drop formation (Walzel, 2010):

- **Dripping** is the simplest process of drop formation. Due to gravity a drop is formed on a solid surface or at the outlet of a thin circular tube. When the gravitational force exceeds the surface tension force, the drop detaches and falls to the ground. The drop size depends on the surface tension, the liquid density and the gravitational acceleration. At dripping from capillary tubes, the capillary tube diameter and the liquid/nozzle wetting additionally influence the droplet diameter. A typical droplet diameter for water dripping from a horizontal wetted surface is 9 mm (Lefebvre, 1989).

- **Jet breakup** occurs when a liquid jet in a gaseous atmosphere or in a vacuum is subjected to disturbances. After emerging from the nozzle, the cylindrical jet surface exhibits perturbations and oscillations. Under proper circumstances, the disturbances are amplified and the jet disintegrates into droplets. This phenomenon, which includes Rayleigh jet breakup, is discussed in section 2.2.1.

- **Sheet breakup** is another mechanism of drop formation. According to Fraser & Eisenklam (1953), there are three different modes of sheet disintegration.

  - In the *rim* mode, due to surface tension forces, the free edge of a liquid sheet is contracted into a thick rim. This rim disintegrates similarly to a liquid jet.

  - The *wave* mode is a result of the generation of wave motions on the sheet. Thus, areas corresponding to the half or full wavelength of the disturbance are contracted into irregular structures, which disintegrate into droplets.

  - During *perforated-sheet* disintegration, ligaments are formed due to holes in the liquid sheet. These ligaments then break up into droplets.

- **Dispersion of liquids by gas** occurs when a gas jet strikes a liquid surface. If the relative velocity is sufficiently high, the dynamic pressure of the gas exceeds the internal pressure of the drops and the liquid is dispersed. Viscous stresses also contribute to this mechanism.

2.2.1 Breakup of liquid jets

As briefly mentioned above, a liquid jet may disintegrate due to oscillations and perturbations. Depending on the fluid properties, the velocity and the diameter of the jet, as well as on the fluid properties of the ambient gas, various modes of jet disintegration can occur. von Ohnesorge (1936) identified three main mechanisms of jet breakup and plotted his results as a function of Ohnesorge number and Reynolds number. Reitz (1978) enhanced the Ohnesorge chart, sub-dividing the wind-induced

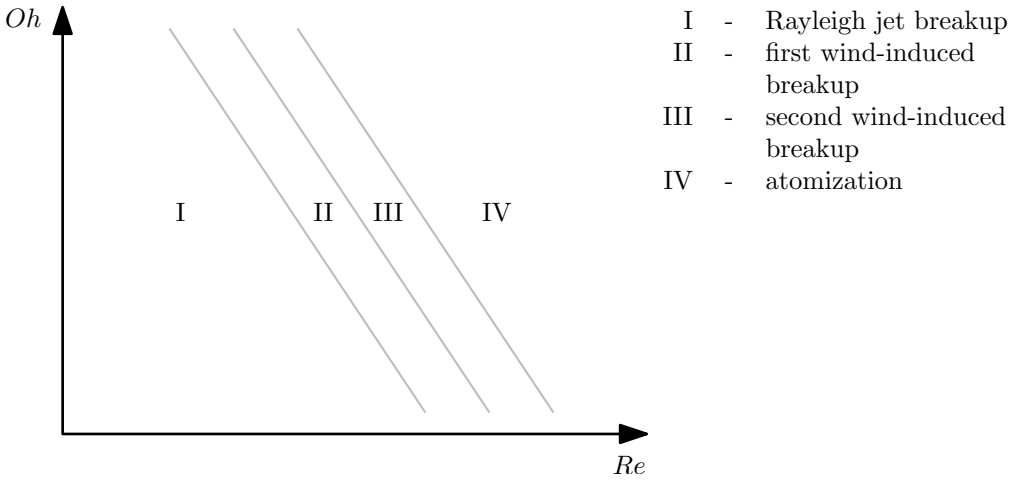

Figure 2.3: Different modes of disintegration of a liquid jet (adapted from Reitz, 1978).

regime into two, so that four different regimes emerged, which can be seen in figure 2.3. The four different modes of jet disintegration are described below.

Rayleigh jet breakup

The Rayleigh jet breakup mechanism can be explained by the theoretical investigations of Plateau (1873) and Rayleigh (1878). It is based on the so called *Plateau-Rayleigh instability*, which is caused by axisymmetric oscillations of the jet surface. Under specific conditions, the effect of surface tension amplifies these oscillations, which lead to a disintegration of the jet. Rayleigh (1878) showed that any inviscid liquid jet of diameter d, which is subjected to surface tension only, will become unstable to axisymmetric disturbances under the condition that the wavelength of the disturbance λ satisfies the inequality

$$\lambda > \pi d\,. \tag{2.11}$$

Furthermore, the wavelength of the fastest growing disturbance is given by

$$\lambda_{\text{opt}} = 4.51 d\,, \tag{2.12}$$

leading to a droplet diameter after breakup of

$$D = 1.89 d\,. \tag{2.13}$$

Weber (1931) extended Rayleigh's analysis by including the viscosity of the liquid. Under the assumption that every disturbance causes axisymmetric oscillations of the jet interface (see figure 2.4), he came to the result that every initial disturbance with a wavelength less than λ_{min} is damped out by surface tension forces. On the other hand, if the wavelength of the initial disturbance is larger than λ_{min}, it is unstable and surface tension forces lead to jet disintegration. Weber (1931) showed that, for viscous

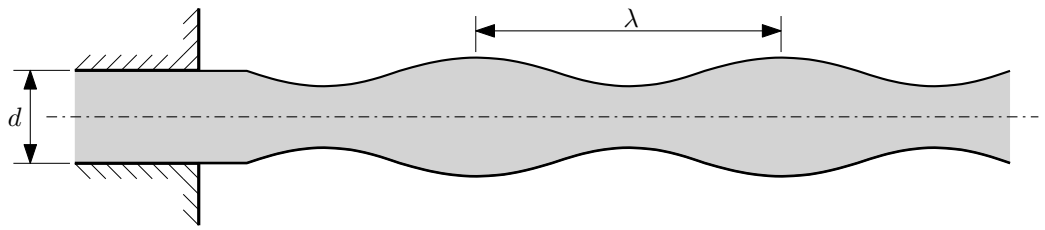

Figure 2.4: Jet with axisymmetric disturbance (adapted from Lefebvre, 1989).

liquids, the minimum wavelength is given by

$$\lambda_{\min} = \pi d\,, \tag{2.14}$$

which is exactly the same value as for inviscid liquids (see equation (2.11)). The optimum wavelength can be calculated by

$$\lambda_{\text{opt}} = \pi d\sqrt{2 + 6\,Oh}\,, \tag{2.15}$$

which leads to greater optimum wavelengths for more viscous fluids. Furthermore, Weber (1931) investigated the influence of the air on the disintegration of a liquid jet. He found that, with increasing relative air velocity, $\lambda_{\min}$ and λ_{opt} are decreased.

First wind-induced breakup

In this case, the relative motion of the ambient gas amplifies the effect of surface tension, which is responsible for the disintegration of the liquid jet in the Rayleigh jet breakup regime. Thus, the breakup process is accelerated. The breakup takes place many jet diameters downstream of the nozzle, producing droplets with diameters of the same order of magnitude as the jet diameter.

Second wind-induced breakup

The second wind-induced breakup mechanism can be explained by the unstable growth of short waves on the surface of the jet. These waves are caused by relative motion of the liquid jet and the ambient gas. Contrary to the first wind-induced breakup regime, surface tension opposes the wave growth in this case. The breakup takes place many jet diameters downstream of the nozzle, producing droplets with diameters much smaller than the jet diameter.

Atomization

Atomization represents the complete disintegration of the liquid jet at the nozzle exit. The liquid is disrupted in a chaotic manner immediately after entering the

gaseous atmosphere. The diameter of the formed droplets is much smaller than the jet diameter.

2.2.2 Technical design

This section gives an overview of the different technical designs used for droplet production. Droplet production systems commercially used in ink-jet printing technology are of many different types, and only an overview is given here. In detail, there are many different designs. Below, only an overview is given (according to Le, 1998). The method used in this work (continuous droplet production) is described in more detail.

Continuous droplet production

Continuous droplet production is based on the Plateau-Rayleigh instability. A liquid jet is disturbed by applying a pressure wave pattern to it, leading to its disintegration into droplets (see section 2.2.1). Continuous ink-jet technologies can be generally divided into binary and multiple deflection methods.

A continuous ink-jet system with a multiple deflection system is sketched in figure 2.5. On the left-hand side, a drop generator can be seen. It applies a wave pattern to the liquid jet, leading to its disintegration. Then the droplets are charged at different levels

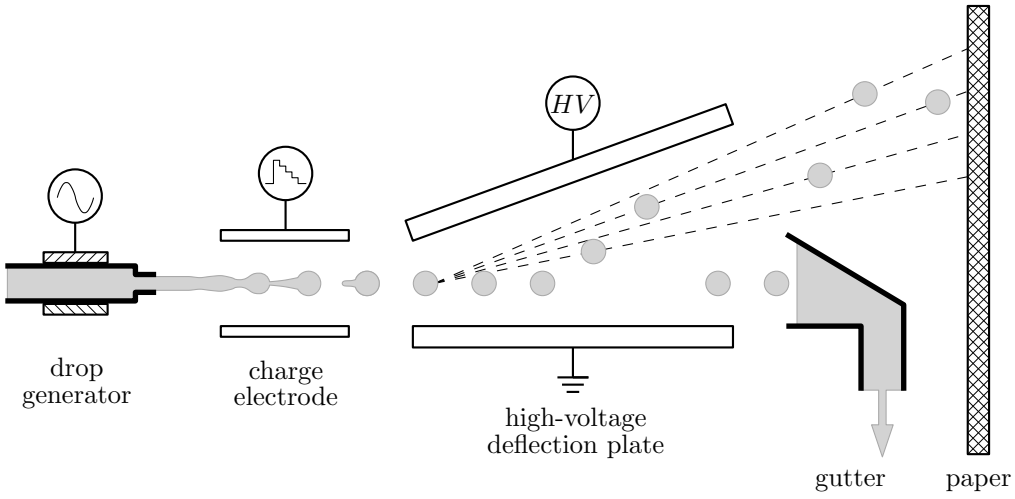

Figure 2.5: Continuous ink-jet with a multiple deflection system (adapted from Le, 1998).

and deflected to the media by a high-voltage deflection plate. The uncharged droplets fly straightforward into a gutter. In a binary deflection system, the uncharged droplets fly straight to the media and the charged droplets are deflected into the gutter.

In this master's thesis work, similar drop generators (Brenn *et al.*, 1996) are used without a deflection system, because it is not required. The disintegration of a liquid jet using a piezoceramic drop generator is pictured in figure 2.6. The liquid is an aqueous glycerol solution at 60% mass percentage of glycerol, the orifice diameter is 200 μm, the drop generator is driven with an excitation frequency of 7659 Hz and the jet velocity is around 5.6 m s^{-1}.

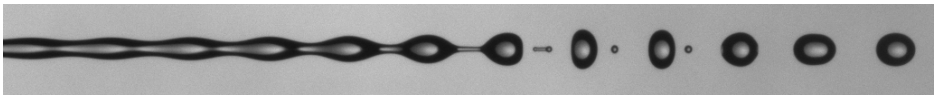

Figure 2.6: Disintegration of a liquid jet using glycerol 60% as a liquid. The drop generator is driven with $f = 7659$ Hz, the undisturbed jet diameter is 200 μm and the jet velocity is approximately 5.6 m s^{-1}.

Drop-on-demand technologies

Drop-on-demand ink-jet is a technology for which individual droplets emerge from the nozzle in a controlled process. The most commonly used drop-on-demand techniques are based on the the following technologies:

- *Thermal* for which drop formation results from nucleation/evaporation. Through a small heater some of the ink is evaporated in a few microseconds. A bubble is formed, leading to a pressure increase in the ink chamber. As a result, a droplet is pushed out of the orifice.
- *Piezoelectric*. By applying a voltage to a piezoelectric material inside the ink chamber, the material is deformed, generating a pressure pulse in the liquid. Thus, a droplet of ink is forced out of the nozzle.
- At a *valve-jet*, the ink is held under pressure and the orifice is closed by a dynamic valve. A droplet is produced by opening this valve, for example with an electromagnet, for a short time step.

In our experiments, continuous-stream drop generators are used. We now discuss the basics of binary drop collisions.

2.3 Binary drop collisions of the same liquid

In order to describe the outcome of binary drop collisions of the same liquid, several parameters are required. First of all, the fluid properties have to be determined. These are the liquid density ρ, the dynamic viscosity μ and the surface tension σ of the droplet liquid against the ambient medium. Moreover, the collision outcome depends on the density and the composition of the ambient medium, which is atmospheric air in the present work. The temperature is constant at $T \approx 23 \pm 2\,°\mathrm{C}$. Furthermore, geometric and kinematic quantities, including the droplet diameters D_1 and D_2, the relative velocity U between the droplets and the impact parameter b are important. As illustrated in figure 2.7, the impact parameter b is the distance between the centroids of the two colliding droplets, measured normal to the direction of the relative velocity U.

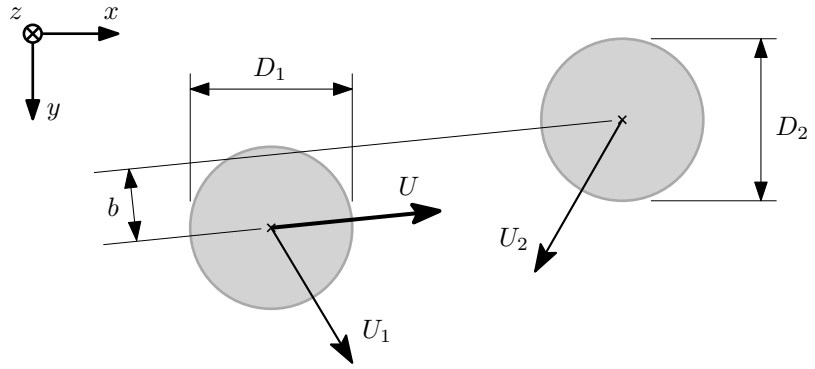

Figure 2.7: Parameters of binary drop collisions (adapted from Planchette *et al.*, 2012).

This set of parameters leads to five non-dimensional numbers, with which the collision outcome can be described systematically. The first number is the drop size ratio δ, which can be written as

$$\delta = \frac{D_1}{D_2}\,, \tag{2.16}$$

where D_1 is the diameter of the smaller droplet and D_2 is the diameter of the larger droplet. Secondly, the non-dimensional impact parameter X is introduced as

$$X = \frac{2b}{(D_1 + D_2)}\,. \tag{2.17}$$

The last three non-dimensional numbers are the Weber number, the Ohnesorge number and the Reynolds number, which are defined and discussed in section 2.1.2 and read

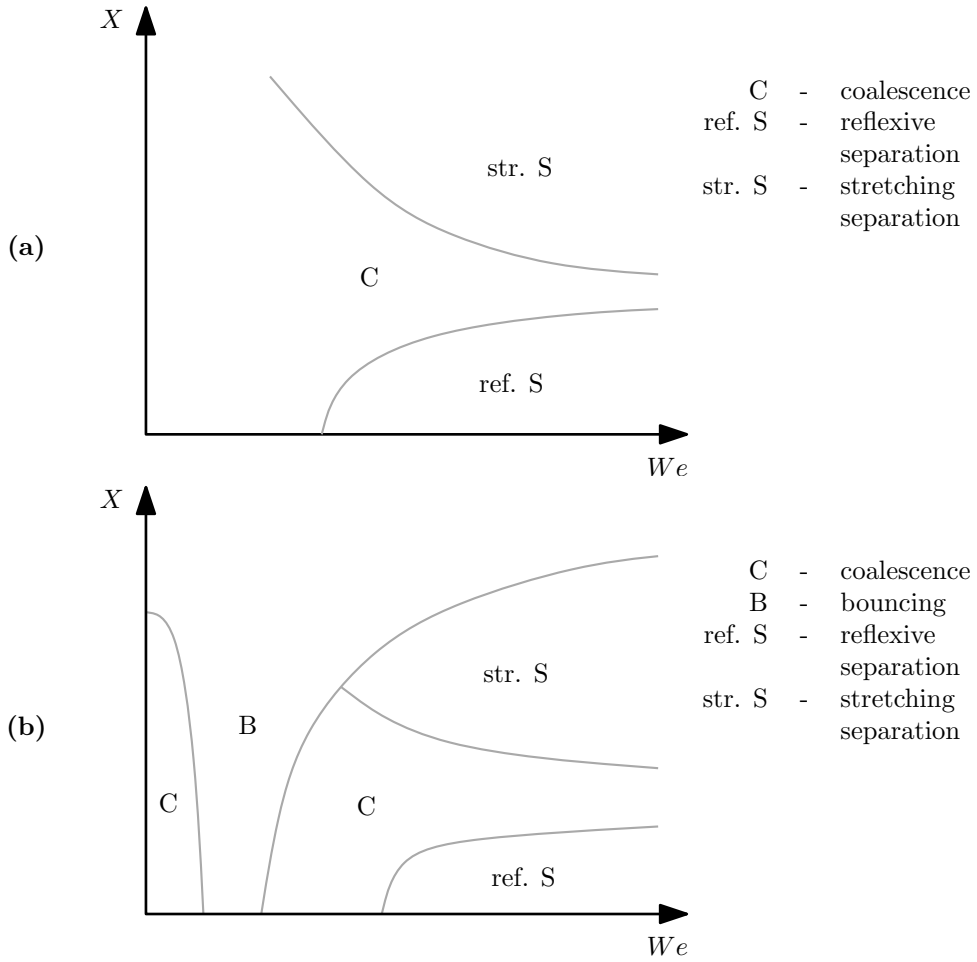

Figure 2.8: Schematic stability nomogram for binary drop collisions in air: **a** water droplets, **b** hydrocarbon droplets (adapted from Qian & Law, 1997).

for binary drop collisions

$$Re = \frac{\rho D U}{\mu}\,, \qquad We = \frac{\rho D U^2}{\sigma} \qquad \text{and} \qquad Oh = \frac{\mu}{\sqrt{\rho\,\sigma D}}\,, \tag{2.18}$$

where $D = (D_1 + D_2)/2$. Since the Ohnesorge number can be expressed in terms of Reynolds number and Weber number by

$$Oh = \frac{\sqrt{We}}{Re}\,, \tag{2.19}$$

only four of these five non-dimensional numbers are independent of each other.

Typically, the collision outcome is presented in the form of a (X, We) nomogram for a given liquid and a constant droplet diameter D (and therefore for a constant

Ohnesorge number *Oh*). Two nomograms for different types of liquids are illustrated in figure 2.8, including a nomogram for water droplets (see figure 2.8 **a**) and one for hydrocarbon droplets (see figure 2.8 **b**). The collision outcome is plotted as a function of the non-dimensional impact parameter and the Weber number. Collisions with zero or reasonably small impact parameters are called *head-on collisions*, whereas unstable collisions, which lead to separation, with sufficiently large impact parameters are so-called *grazing collisions*. From figure 2.8 follows that there are four possible collision outcomes:

- coalescence
- bouncing
- reflexive separation
- stretching separation

Strictly speaking, there is a fifth regime called *droplet shattering*, but since it appears only at relatively high Weber numbers it is not a part of this study. Nevertheless, it will be explained briefly later on.

In figure 2.9, the four main possible collision outcomes of binary liquid drop collisions are illustrated. On the left hand, in figure 2.9 **a**, the different stages of two coalescing droplets are sketched. As a first step, the gas between the two approaching droplets is expelled. Then the drops merge and deform into a disk, or more precisely into some kind of torus-shaped complex, but with a lamella instead of a hole in the centre (Ashgriz & Poo, 1990; Roisman *et al.*, 2012). Afterwards, the merged droplet oscillates until it relaxes into a sphere.

Bouncing, as given in figure 2.9 **b**, is another possible collision outcome. It occurs when the intervening gas layer between the two droplets cannot be expelled. As a result, the two droplets bounce apart. The critical thickness for the inter-droplet gap is of the order of $0.01\,\mu$m (Mackay & Mason, 1963), which is the typical distance for molecular interactions. It has to be stated that bouncing highly depends on the surrounding gas and therefore on its density, viscosity, humidity and other vapours content.

In figure 2.9 **c**, the regime of reflexive separation is illustrated. Similar to the regime of coalescence, the merged droplets form a disk after the collision. However, because of higher kinetic energy compared to the regime of coalescence, the oscillation of the

merged droplet separates it reflexively into two droplets again. Increasing the kinetic energy in the regime of reflexive separation leads to the formation of a ligament which connects the two droplets (as illustrated in figure 2.9 **c**). This ligament finally breaks up and induces the formation of one or more satellite droplets. Reflexive separation occurs for head-on collisions and for rather small impact parameters.

The phenomena of stretching separation (see figure 2.9 **d**) occurs for moderate and large impact parameters. In this inertia-dominated process, parts of the two droplets coalesce, while the remaining parts of the original droplets stay on their initial trajectories. Thus, a ligament between the two droplets is formed, which is stretched until it breaks up into one or more satellite droplets.

As mentioned before, there is a fifth regime called droplet shattering. For this mechanism, a high Weber number, and therefore high kinetic energy, is required. After a large deformation of the droplets, it leads to a chaotic breakup of the resulting liquid system. Since its onset Weber number is around 400 (Brenn, 2011) for binary drop collisions, this phenomenon is not investigated in this work. It seems that droplet shattering is highly depending on the surrounding gas, since Willis & Orme (2000) and Willis & Orme (2003) could not observe this mechanism for Weber numbers larger than 2000 in a vacuum environment.

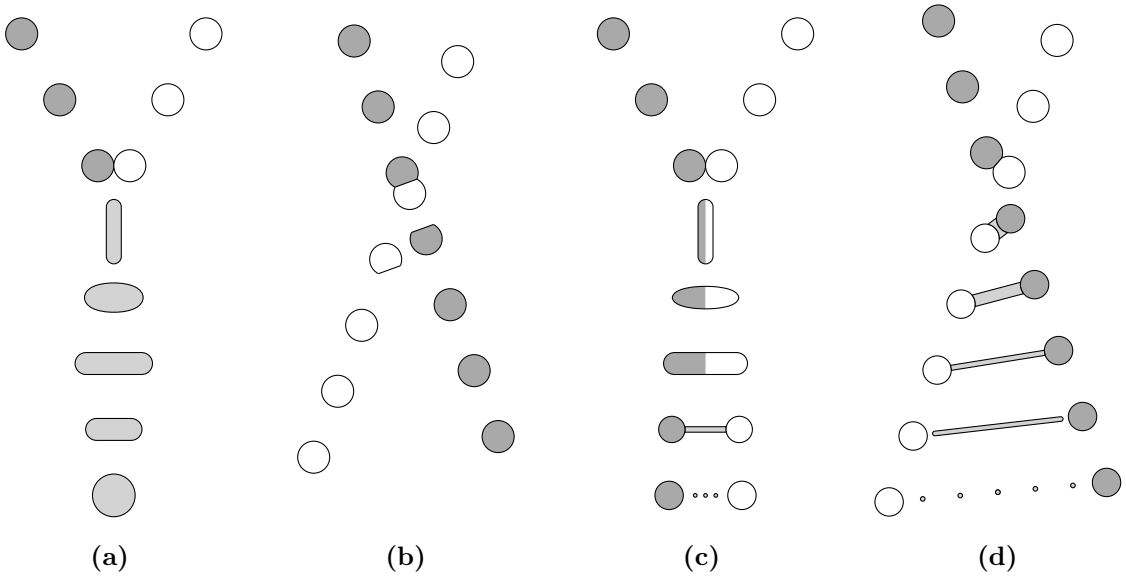

Figure 2.9: Schematic representation of the four possible collision outcomes of binary liquid drop collisions: **a** coalescence, **b** bouncing, **c** reflexive separation, **d** stretching separation (adapted from Ko & Ryou, 2005).

It has to be stated that the regime of reflexive separation described above can be replaced by the so called *single reflex separation* (Chen & Chen, 2006) or *crossing separation* (Planchette *et al.*, 2010) for collisions of two immiscible liquids.

We now discuss the collision process leading to the onset of reflexive separation.

2.4 Reflexive separation criteria

To estimate the transition between the regimes of coalescence and separation for binary drop collisions (see figure 2.8), many different models have been developed. Two models from the literature, which determine the onset Weber number for the transition between coalescence and reflexive separation for binary head-on collisions of equal-sized droplets of the same liquid, are introduced in this section.

2.4.1 The model of Ashgriz & Poo (1990)

In order to explain reflexive separation for water droplets, Ashgriz & Poo (1990) introduced the concept of *effective reflexive energy*, which is in their point of view the cause for reflexive separation. They assume that the total energy of the combined mass after the collision is composed by the kinetic energy and the surface energy. The flow is considered to be inviscid and therefore viscous dissipation is neglected. This is a limit of this approach, since experimentally it has been shown that the onset of reflexive separation is a function of the dynamic viscosity (Willis & Orme, 2003). The effective reflexive energy K_r is the sum of the initial kinetic energy K_c and the kinetic energy of the excess surface induced flow K_e. The former is given by

$$K_c = 2\frac{1}{2}\rho\frac{4}{3}\pi\left(\frac{D}{2}\right)^3\left(\frac{U}{2}\right)^2 = \frac{1}{24}\pi\rho D^3U^2 \tag{2.20}$$

and the latter corresponds to the difference between the surface energy of the initial droplets and the surface energy of the combined spherical mass, which reads

$$K_e = 2\sigma\pi D^2 - \sigma\pi\left(2^{1/3}D\right)^2 = \sigma\pi D^2\left(2 - 2^{2/3}\right) . \tag{2.21}$$

As a consequence, the effective reflexive energy is

$$K_r = K_c + K_e = \sigma\pi D^2 \left(2 - 2^{2/3} + \frac{We}{24}\right) . \tag{2.22}$$

The criterion for the occurrence of reflexive separation is based on the linear theory of Rayleigh (1879), who showed that a liquid column becomes unstable if its length-to-diameter ratio is equal to π or larger. Consequently, Ashgriz & Poo (1990) investigated the last phase of binary drop collisions, where the combined mass is stretched into a cylinder. Such a cylinder, with a total length of $l + 2r$ and a diameter of r, can be seen in figure 2.10. Its critical length-to-diameter ratio is given by

$$\frac{l}{r} = 2\pi - 2 . \tag{2.23}$$

Due to surface tension, the liquid at both ends is forced towards the centre, which would prevent separation. The cylinder can disintegrate only if the momentum rate of the internal flow field compensates the surface tension forces and sustains the shape of the cylinder. As a result, disturbances are able to grow and break the cylinder.

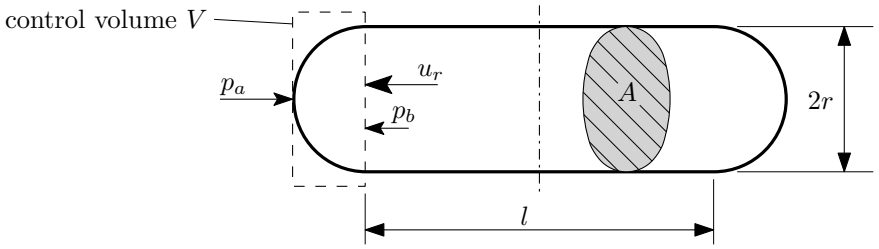

Figure 2.10: Schematic of a cylindrical shaped drop formed in the last stage of the collision (adapted from Ashgriz & Poo, 1990).

In order to calculate the minimum internal kinetic energy, which is necessary to sustain the shape of the cylinder, the internal velocity of the cylinder has to be estimated. Therefore, a force balance is applied to the control volume V sketched in figure 2.10, which leads to

$$\frac{\mathrm{d}}{\mathrm{d}t} \int u\rho \mathrm{d}V - \rho u_r^2 A = (p_b - p_a)A , \tag{2.24}$$

where u_r is the reflexive velocity and u the velocity inside the control volume. The pressures are estimated by $p_a = 2\sigma/r$ and $p_b = \sigma/r$ and the cross sectional area A can be calculated by $A = r^2\pi$. The unsteady term on the left-hand side is estimated

by the product of an average velocity $\bar{u}$ and the mass flow rate $\mathrm{d}m/\mathrm{d}t$. The average velocity is estimated by the mean value between the velocity at the left ($u = 0$) and the right ($u = u_r$) boundary of the control volume, which yields $\bar{u} = u_r/2$. By assuming $\mathrm{d}m/\mathrm{d}t = \rho u_r A$ and substituting everything into equation (2.24), the reflexive velocity can be calculated by

$$u_r = \left(\frac{2\sigma}{\rho r}\right)^{1/2} . \tag{2.25}$$

The minimum kinetic energy to sustain the cylindrical shape is approximated by

$$K_m = \frac{1}{2}\rho\left(r^2\pi l + \frac{4}{3}r^3\pi\right)u_r^2 = 4\sigma\pi r^2\left(\frac{1}{3} + \frac{1}{4}\frac{l}{r}\right) . \tag{2.26}$$

Now it is imagined that the cylinder relaxes into a nominal spherical drop with the reflexive kinetic energy K_r^* and the surface energy S_n^*. The total energy of this nominal spherical droplet is equivalent to the total energy of the cylindrical droplet. Therefore the energy can be balanced by

$$K_r^* + S_n^* = K_m + S_m \,, \tag{2.27}$$

where S_m is the surface energy of the cylindrical droplet. Normalizing equation (2.27) by S_n^* leads to the critical condition for reflexive separation for the quantity Γ, which is defined by the ratio of K_r^* to S_n^*:

$$\Gamma = \frac{K_r^*}{S_n^*} = \frac{K_m}{S_n^*} + \frac{S_m}{S_n^*} - 1 \tag{2.28}$$

The surface energies S_n^* and S_m can be calculated as

$$S_n^* = 4\sigma\pi r^2\left(1 + \frac{3}{4}\frac{l}{r}\right)^{2/3} \qquad \text{and} \qquad S_m = 4\sigma\pi r^2\left(1 + \frac{1}{2}\frac{l}{r}\right) . \tag{2.29}$$

Using equations (2.26) and (2.29), equation (2.28) can be rewritten as

$$\Gamma = \left(1 + \frac{3l}{4r}\right)^{-2/3}\left(\frac{4}{3} + \frac{3l}{4r}\right) - 1 \,. \tag{2.30}$$

Applying the critical length-to-diameter ratio given in equation (2.23), leads to a value

for Γ of 0.7425. Therefore it can be argued that *"for a nominal spherical combined mass, when the effective reflexive kinetic energy is more than 75% of its nominal surface energy, reflexive separation will occur"* (Ashgriz & Poo, 1990: 199). Consequently, the criterion for reflexive separation for equal-sized droplets can be written as

$$K_r \geq 0.75\sigma\pi 2^{2/3} D^2 \,. \tag{2.31}$$

Introducing this criterion into equation (2.22) leads to a critical Weber number for the transition between coalescence and reflexive separation, at zero impact parameter, of

$$We_0 = 6\left(7 \cdot 2^{2/3} - 8\right) \approx 19 \,. \tag{2.32}$$

Since this criterion is based on inviscid flow assumptions, it is described by only one parameter, the Weber number. This is a limitation of this model, because only inviscid fluids are considered. Jiang *et al.* (1992) showed experimentally that the viscous loss for binary collisions of water droplets cannot be neglected. In the next section their theoretical model for viscous fluids will be introduced.

2.4.2 The model of Jiang et al. (1992) and of Qian & Law (1997)

The criterion for head-on reflexive separation developed by Jiang *et al.* (1992) and by Qian & Law (1997) is based on considerations of kinetic energy, surface energy and viscous dissipation. Thus, their approach is more general than the previously introduced model of Ashgriz & Poo (1990). According to Qian & Law (1997), the droplet collision sequence consists of three different stages (see figure 2.11).

In period 1, two droplets collide and spread outward into a disk. After this disk reaches its maximum extension, in period 2, the disk contracts back into a droplet shaped complex due to surface tension forces. Finally, in period 3, the complex stretches into a cylinder, with its both ends pushing outward. Subsequently, a dumb-bell with a thin connecting ligament is formed. If the initial kinetic energy is large enough, the ligament breaks and the droplets separate. Otherwise, surface tension pulls the ends of the dumb-bell back and the excess energy is dissipated during oscillations under viscous loss.

At the transition between coalescence and reflexive separation, the energy can be balanced by

$$E_k = \Phi_1 + \Phi_2 + \Phi_3 + \Phi_r \,, \tag{2.33}$$

where E_k is the initial kinetic energy of the two droplets. It is given by

$$E_k = \rho \frac{1}{6} \pi D^3 \left(\frac{1}{2} U \right)^2 \,, \tag{2.34}$$

where D is the droplet diameter, assuming both drops are equally sized. The viscous dissipation Φ_1, Φ_2 and Φ_3 during the periods 1, 2 and 3 can be generally calculated for each period by

$$\Phi_{1,2,3} = \mu \int \int \frac{1}{2} \left(\frac{\partial v_i}{\partial x_j} + \frac{\partial v_j}{\partial x_i} \right) \mathrm{d}t \, \mathrm{d}x^3 \,. \tag{2.35}$$

The last term on the right hand side of equation (2.33) represents an additional surface energy, which the deformed droplet mass possesses at the instant of breakup, compared to the surface energy of the original spherical droplets. It can be calculated by

$$\Phi_r = \sigma \Delta S \,, \tag{2.36}$$

where ΔS is the additional surface area of the deformed droplet compared to the original spherical droplet. ΔS is evaluated from experimental data.

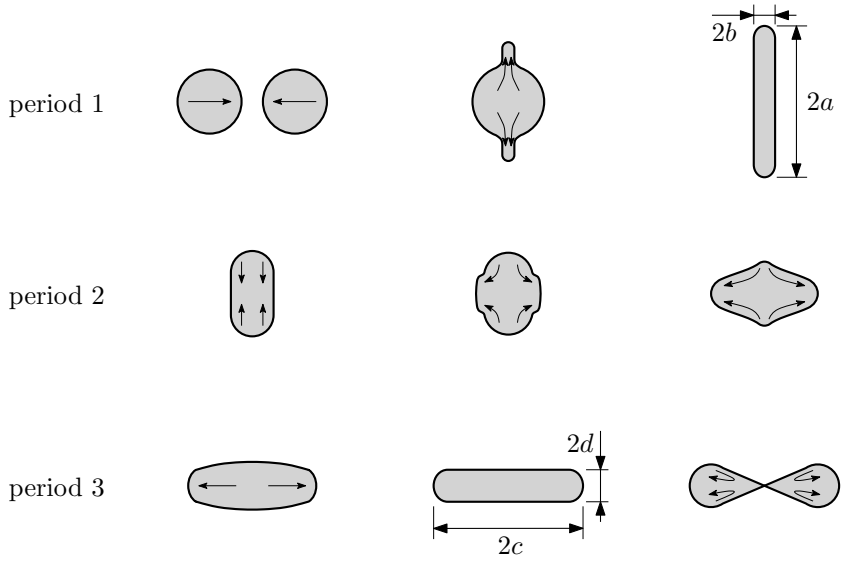

Figure 2.11: Illustration of the three periods of binary head-on collisions of droplets (adapted from Qian & Law, 1997).

Viscous dissipation during period 1

According to Jiang *et al.* (1992), in the first stage of the collision, before the maximum deformation of the disk is reached, the drops may be considered as a central disk sandwiched by two caps (see figure 2.12). It is assumed that the two caps are not affected by the collision. As a consequence, their spherical contour remains and, moreover, they move constantly at $U/2$, where U is the impact relative velocity. Thus, the time period until the disk reaches its maximum extension can be estimated by $2D/U$. Jiang *et al.* (1992) argue that the maximum velocity gradient, with a strain rate of approximately $U/2h$, is located in the stagnation flow region. Therefore, the thickness $2h$ of this stagnation flow region can be calculated by using the relation $\rho(U/2)^2/2 \approx \mu U/2h$. This leads to $h \approx 4\mu/\rho U$. The volume of the stagnation flow region can be estimated by $(2h)(D^2\pi/4)$. According to equation (2.35), the amount of energy dissipated in period 1 can therefore be calculated by

$$\Phi_1 \approx \mu \left(\frac{U}{2h}\right)^2 \left(\frac{1}{2}\pi h D^2\right) \left(\frac{2D}{U}\right) \approx \frac{1}{16}\pi\rho D^3 U^2 \,. \tag{2.37}$$

It is interesting to note that, according to equation (2.37), the amount of dissipated energy is independent of the dynamic viscosity μ. Taking the previous assumptions into account, Φ_1 can be estimated by a fractional amount $\hat{\alpha}$ of initial kinetic energy

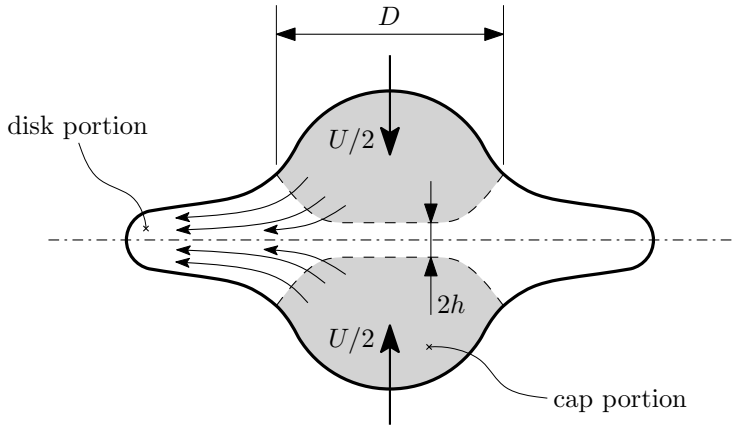

Figure 2.12: Schematic model of period 1 of the collision (adapted from Jiang *et al.*, 1992). The disk portion is coloured white and the cap portion is coloured grey.

dissipated. Therefore, it is given by

$$\Phi_1 = \frac{1}{24}\pi\hat{\alpha}D^2\sigma\,We\,. \tag{2.38}$$

The value of $\hat{\alpha}$ has to be determined empirically for each liquid, which is a drawback of this approach. Jiang *et al.* (1992) obtained $\hat{\alpha} \approx 0.5$ for hydrocarbon and water droplets.

Viscous dissipation during period 2

In order to evaluate the amount of energy dissipated in period 2, the characteristic liquid velocity v_2 towards the centre has to be evaluated. Therefore the pressure and surface tension forces are balanced, which reads

$$\frac{1}{2}\rho v_2^2 = \sigma\left(\frac{1}{a}+\frac{1}{b}\right)\,, \tag{2.39}$$

where a and b are geometrical parameters according to figure 2.11. Rearranging equation (2.39) leads to

$$v_2 = \left[\frac{2\sigma}{\rho}\left(\frac{1}{a}+\frac{1}{b}\right)\right]^{1/2}\,. \tag{2.40}$$

The volume of the whole complex can be calculated by $\pi D^3/3$ and the time which lapses until the drop regains its spherical shape is estimated by a/v_2. With the help of equation (2.35), Φ_2 can be written as

$$\Phi_2 \approx \frac{1}{2}\mu\left(\frac{v_2}{b}\right)^2\left(\frac{a}{v_2}\right)\frac{1}{3}\pi D^3 = \frac{2}{3}\pi D^{3/2}\mu\frac{\tilde{a}}{\tilde{b}^{5/2}}\left[\frac{\sigma}{\rho}\left(1+\frac{\tilde{b}}{\tilde{a}}\right)\right]^{1/2}\,, \tag{2.41}$$

where $\tilde{a} = 2a/D$ and $\tilde{b} = 2b/D$. Equation (2.41) depends on the droplet diameter, the fluid properties and two geometrical parameters. The latter have to be determined separately for collisions at different conditions.

Viscous dissipation during period 3

The amount of energy dissipated in period 3 is evaluated analogously to period 2. The characteristic liquid velocity v_3 is estimated from balancing pressure and surface

tension forces, which reads

$$\frac{1}{2}\rho v_3^2 = \frac{2\sigma}{d}\,. \tag{2.42}$$

Consequently, v_3 is given by

$$v_3 = \left(\frac{4\sigma}{\rho d}\right)^{1/2}\,. \tag{2.43}$$

The volume is calculated by $\pi D^3/3$ and the elapsed time is assumed to be in the order of c/v_3. Thus, the viscous dissipation Φ_3 can be expressed by

$$\Phi_3 \approx \frac{1}{2}\mu\left(\frac{v_3}{d}\right)^2\left(\frac{c}{v_3}\right)\frac{1}{3}\pi D^3 = \frac{2}{3}\pi D^{3/2}\mu\left(\frac{2\sigma}{\rho}\right)^{1/2}\left(\frac{\tilde{c}}{\tilde{d}^{5/2}}\right)\,, \tag{2.44}$$

where $\tilde{c} = 2c/D$ and $\tilde{d} = 2d/D$. The geometrical parameters c and d are given in figure 2.11 and have to be determined individually for collisions at different conditions.

Now that all viscous losses are evaluated, the critical Weber number We_0 for the transition between coalescence and reflexive separation of binary head-on collision can be calculated. Therefore, equations (2.36), (2.38), (2.41) and (2.44) are substituted into equation (2.33) and normalized by the initial surface tension energy $2\sigma(\pi D^2)$, which leads to

$$We_0 = \frac{1}{1-\hat{\alpha}}\left\{\frac{\tilde{a}}{\tilde{b}^{5/2}}\left[\frac{1}{2}\left(1+\frac{\tilde{b}}{\tilde{a}}\right)\right]^{1/2} + \frac{\tilde{c}}{\tilde{d}^{5/2}}\right\} 16\sqrt{2}\,\underbrace{\frac{\mu}{\sqrt{\rho\,D\,\sigma}}}_{Oh} + \frac{24\Delta S}{(1-\hat{\alpha})\pi D^2}\,. \tag{2.45}$$

This is a linear equation

$$We_0 = \bar{A}\,Oh + \bar{B}\,, \tag{2.46}$$

where $\bar{A}$ and $\bar{B}$ are geometrical parameters, independent of the fluid properties. Therefore, at the transition from coalescence to reflexive separation, the separation criterion can be described in terms of two non-dimensional numbers, namely We and Oh. The drawback of the criterion given by equation (2.45) is that four individual geometrical parameters and ΔS have to be determined experimentally.

3 Materials and methods

In the first part of this chapter, the liquids used for the experimental investigations are introduced. Afterwards, the experimental set-up and the procedure of image processing is described for binary and ternary droplet collisions. Finally, a list of the used laboratory equipment is given.

3.1 Liquids and measurements

In order to analyse binary and ternary drop collisions, experiments with different liquids are performed. In table 3.1 the used liquids and their physical properties are listed. Almost all experiments are performed with aqueous glycerol solutions. The concentrations of these solutions are given in mass percent of glycerol. Distilled water has been used for the preparation of the mixtures. By using aqueous glycerol solutions,

Liquids	Density $\rho\,[\mathrm{kg\,m^{-3}}]$	Dynamic viscosity $\mu\,[\mathrm{mPa\,s}]$	Surface tension $\sigma\,[\mathrm{mN\,m^{-1}}]$
Glycerol 10% (Gl 10%)	1012.46	1.23	68.94
Glycerol 30% (Gl 30%)	1063.22	2.17	67.45
Glycerol 40% (Gl 40%)	1096.00	3.15	66.79
Glycerol 50% (Gl 50%)	1131.30	5.24	66.53
Glycerol 60% (Gl 60%)	1153.88	8.81	65.27
Glycerol 65% (Gl 65%)	1166.60	12.11	64.39
Glycerol 70% (Gl 70%)	1179.90	17.84	64.00
Silicon oil M3 (SO M3)	887.48	2.79[a]	19.50
Silicon oil M10 (SO M10)	931.40	9.37[a]	20.10

Table 3.1: Measured properties of the investigated liquids at $\approx 23\,^{\circ}\mathrm{C}$. Glycerol concentration in aqueous glycerol solutions are given as mass percentage. [a] Values given by the data sheet of the supplier *Carl Roth* at $20\,^{\circ}\mathrm{C}$.

Liquids	Orifice diameter D_{or} [μm]				
	70	100	200	300	500
Glycerol 10 %			• ○		
Glycerol 30 %	•	• ○	• ○		
Glycerol 40 %	•	○	• ○		
Glycerol 50 %	• ○	• ○	• ○	• ○	•
Glycerol 60 %			•		
Glycerol 65 %			•		
Glycerol 70 %			•		
Silicon oil M3			•		
Silicon oil M10			•		

Table 3.2: Performed experiments to describe the transition between coalescence and reflexive separation for the case of head-on collisions of equal-sized droplets: • binary drop collisions, ○ ternary drop collisions.

the dynamic viscosity can be tuned in a wide range, while density and surface tension remain almost constant (see table 3.1). In order to vary the surface tension, experiments with two different silicon oils have been performed for binary drop collisions.

The physical properties in table 3.1 apply for a temperature of $\approx 23\,^{\circ}\mathrm{C}$. The density ρ was obtained by measuring the mass of a defined volume (5 ml) of the liquid. The dynamic viscosity μ was determined with the help of an Ubbelohde viscometer and the surface tension σ was measured with the pendant drop method using a tensiometer type LAUDA TVT-1. For both silicon oils, values for the dynamic viscosity are taken from supplier data sheets.

As mentioned in section 2.2.1, the droplet diameter mainly depends on the diameter of the liquid jet and therefore on the orifice diameter. Basically, four different sized orifices with nozzle diameters of 70, 100, 200 and 300 μm were used, leading to drop sizes ranging from 130 to 570 μm. One experiment has been carried out with an orifice diameter of 500 μm. In table 3.2, the performed experiments are listed. Binary collisions are marked with a filled circle (•) and ternary collisions are marked with an open circle (○).

For all these configurations, the onset velocity U_0, and therefore the onset Weber number We_0, of the transition between coalescence and reflexive separation for head-on collisions is determined. Moreover for glycerol 50 % in combination with the 200 μm

orifice, a stability nomogram, analogous to figure 2.8, was determined for binary and ternary drop collisions. The results are presented in the following chapter.

In addition, the onset of fragmentation at head-on collisions is determined for binary collisions of unequal-sized droplets. Liquids and combined nozzle diameters are listed in table 3.3. Thus, two different droplet size ratios of $\delta = 0.62$ and $\delta = 0.78$ are investigated.

Liquids		Orifice diameter D_{or} [μm]	
		70	200
Glycerol 30 %	100	•	•
Glycerol 40 %	100	•	•
Glycerol 50 %	100	•	•

Table 3.3: Performed experiments to describe the transition between coalescence and reflexive separation for head-on collisions of unequal-sized droplets: • binary drop collisions.

3.2 Binary drop collisions

In the present section, the experimental set-up used to study binary drop collisions is introduced. Afterwards, the equations for the analysis of the images are derived.

3.2.1 Experimental set-up

The experimental set-up for binary drop collisions can be seen in figure 3.1. Two drop generators are connected with a hose to the pressurised tank, which contains the liquid. The pressure is continuously adjustable and measured by an analogue manometer. In order to prevent the nozzles from clogging by particles, the liquid is filtered.

The experimental rig consists of two main components and is placed on a vibration isolated table to avoid environmental disturbances. Its two essential parts are the drop generators and a visualisation system, which are described below. In the case of binary drop collisions, there are two piezoelectric drop generators, which produce stable monodisperse liquid drop streams (Brenn *et al.*, 1996). The liquid jet emerging from the nozzle of a drop generator with the velocity U_J, is disturbed by a piezoceramic oscillator

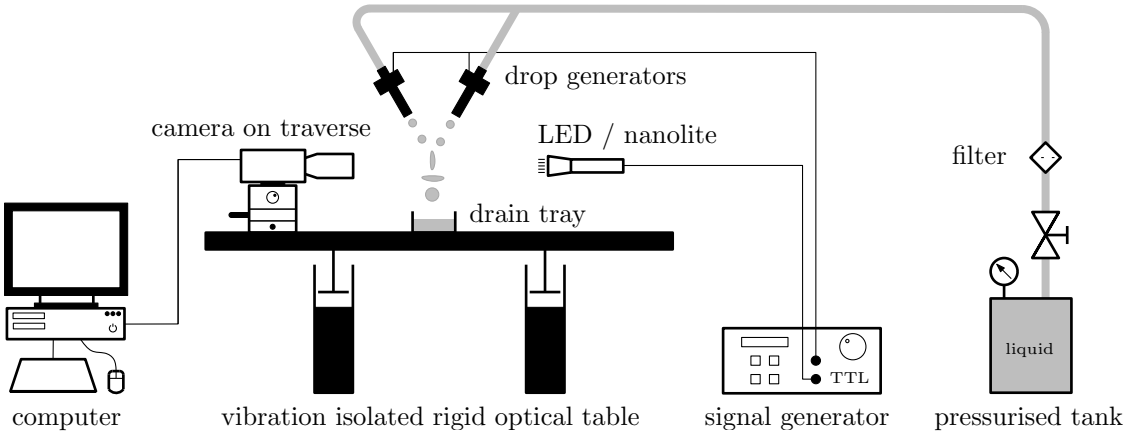

Figure 3.1: Experimental set-up for binary drop collisions of the same liquid.

with the frequency f, leading to instabilities in the jet stream with a wavelength of $\lambda = U_J/f$. Thus, if λ has a proper magnitude (see equation (2.15)), droplets with diameters around twice the diameter of the nozzle hole are produced (see equation (2.13)). Since the nozzle plates of the drop generators are changeable, droplet streams of different sizes can be achieved. In order to adjust the trajectories of the streams, the generators are placed on translation and rotation stages. The accuracy of these movable stages is estimated to be about $\pm 2\,\mu$m and $\pm 2\,^\circ$, respectively. The piezoceramic oscillators of the generators are connected to a signal generator, which provides an AC sine wave output signal with an amplitude of 20 V and a typical frequency of 10 kHz.

The visualisation system can be divided into two parts, the camera system and the illumination system. The camera system used to acquire pictures of the colliding droplets is a PCO Sensicam video camera placed on a traverse. A suitable lens is connected by a C-mount adapter to the camera. Since the droplets have a typical diameter of 130 to 560 μm, a magnification lens is attached to the front side of the objective. The camera is controlled via a computer.

Secondly, the illumination system is responsible for the illumination of the droplet streams. For that purpose two different light sources are used. On the one hand, a *red light LED* and on the other hand, a *nanolite* flash light. The nanolite provides flashes of only a few nanoseconds duration and therefore very sharp images can be acquired. However, the advantage of the LED is that its light flashes are synchronized with the frequency of the drop generators by connecting it to the corresponding TTL output of the signal generator. Thus, the droplet streams appear stationary, which facilitate the adjustment of stability and tuning of the trajectories. Since many pictures of the same

scene are superposed to the final picture with this technique, the images appear less sharp than with the nanolite system. A complete list of the used equipment can be found in section 3.4.

3.2.2 Image processing

In order to extract informations from obtained photographs, two computer programs are used. With the help of the first, called *ImageJ*, the projected area of each drop and the coordinates of its centre of mass are derived . This is illustrated in figure 3.2 for the case of binary drop collisions.

The above mentioned procedure can be described as follows. First of all, the picture has to be cut to select the last two pairs of drops before the collision point. Then the area and the coordinates (x_m, y_m) of the centre of mass are calculated for each droplet by *ImageJ*. The origin of the coordinate system is placed in the left upper corner of the cropped image. For binary drop collisions four droplets remain. With knowledge of the droplet area and assuming spherically shaped drops, the droplet diameter D for each droplet i is given by

$$D_i = \sqrt{\frac{4 \cdot \text{Area}}{\pi}}\,. \tag{3.1}$$

Since all quantities computed by *ImageJ* are given in pixels, a scale is used to convert them into meters. For this purpose, a stage micrometer is used. A photograph of it can

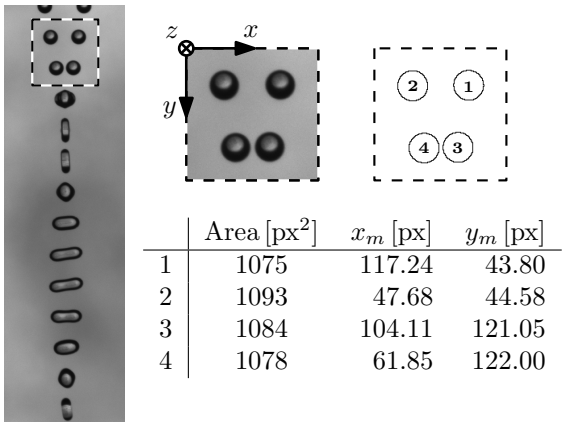

	Area [px^2]	x_m [px]	y_m [px]
1	1075	117.24	43.80
2	1093	47.68	44.58
3	1084	104.11	121.05
4	1078	61.85	122.00

Figure 3.2: Example of image processing with *ImageJ* for binary drop collisions. On the left hand, a photograph of the collision can be seen. On the right hand, a table with the results can be found.

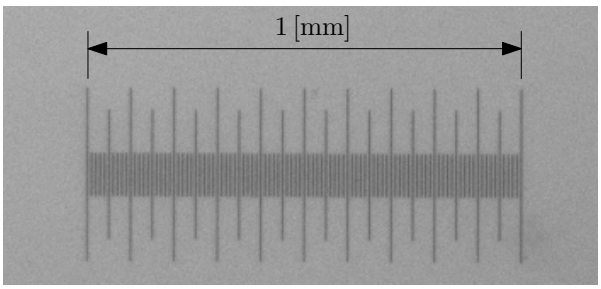

Figure 3.3: Photograph of a stage micrometer. Micrometer scale is 1 mm in 0.01 mm divisions.

be seen in figure 3.3. The micrometer scale is 1 mm, and by measuring this distance in the photograph in [px], the constant factor to convert the desired quantities from [px] to [m] can be determined easily.

Depending on the droplet size, the resolution of the imaging system was varied from $3.3\,\mu\mathrm{m\,px^{-1}}$ to $14.5\,\mu\mathrm{m\,px^{-1}}$. At the estimation of the droplet area in the photographs, which is typically in the order of $A = 1000\,\mathrm{px}^2$ per drop, an error of $\Delta A = \pm\pi D/2\,\mathrm{px}^2$ is assumed. Thus, the accuracy of the estimated drop diameter is roughly 2.8%, which is typically ± 1 px.

By using the droplet diameters D_i, the excitation frequency f of the drop generators and the coordinates of the centroids $x_{m,i}$ and $y_{m,i}$, the relative velocity U and the impact parameter X can be calculated. For binary drop collisions this procedure is shown in section 3.2.3. In order to perform the calculations and handle the data, a second software is used: *GNU Octave*.

3.2.3 Analysis

In figure 3.4, a sketch shows the relative positions of the droplets for binary drop collisions. The drops are numbered from 1 to 4, according to the following rules:

$$\begin{aligned} x_{m,1} \wedge x_{m,2} &< x_{m,3} \wedge x_{m,4} \\ y_{m,1} &< y_{m,2} \\ y_{m,3} &< y_{m,4}\,. \end{aligned} \tag{3.2}$$

To calculate the desired quantities, the three vectors $\vec{l}_{12}$, $\vec{l}_{31}$ and $\vec{l}_{34}$ have to be defined.

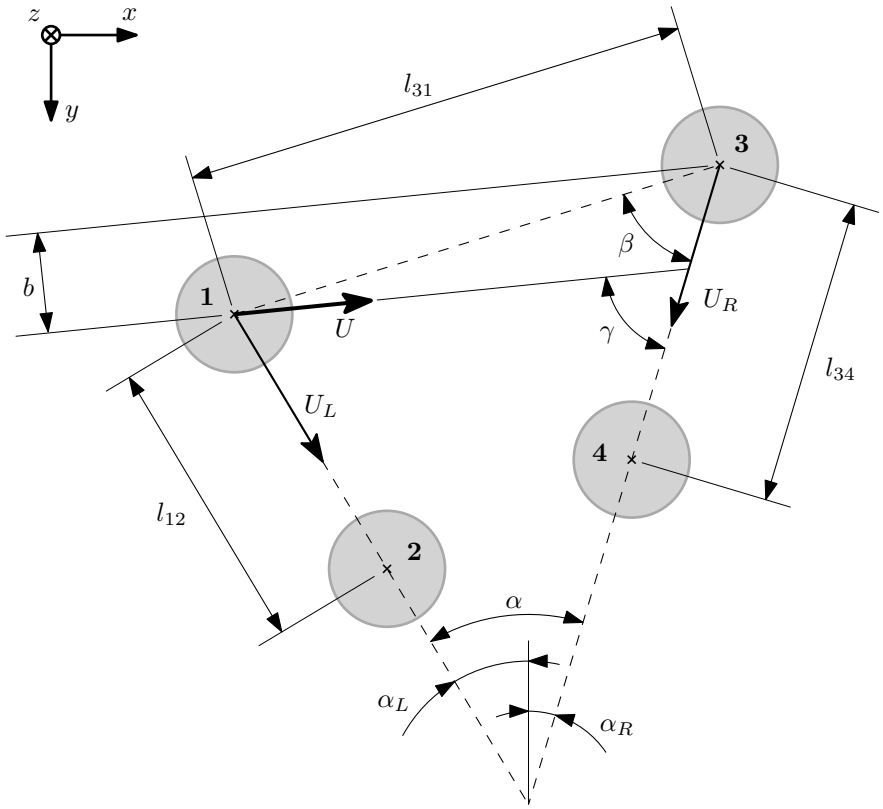

Figure 3.4: Sketch of binary drop collision and notations used for the calculation of the relative velocity U and the non-dimensional impact parameter X.

Each of these vectors $\vec{l}_{ij}$ points from the centre of mass of drop number i to the centre of mass of drop number j and can be written as

$$\vec{l}_{ij} = \begin{pmatrix} x_{m,j} - x_{m,i} \\ y_{m,j} - y_{m,i} \end{pmatrix} . \tag{3.3}$$

Their lengths can be calculated by

$$l_{ij} = |\vec{l}_{ij}| = \sqrt{(x_{m,j} - x_{m,i})^2 + (y_{m,j} - y_{m,i})^2} . \tag{3.4}$$

The average droplet diameter is given by

$$D = \frac{1}{4} \sum_{i=1}^{n=4} D_i . \tag{3.5}$$

The vectors $\vec{l}_{12}$ and $\vec{l}_{34}$ point in the directions of the left and the right droplet stream,

respectively. Together they form the angle α, which can be calculated by

$$\alpha = \cos^{-1}\left(\frac{\vec{l}_{12}\cdot\vec{l}_{34}}{l_{12}\,l_{34}}\right). \tag{3.6}$$

To check the symmetry of the collision, the angle between the trajectories and the vertical axis (y-axis) can be calculated by

$$\alpha_L = \cos^{-1}\left(\frac{\vec{l}_{12}\cdot\binom{0}{1}}{l_{12}}\right) \qquad \text{and} \qquad \alpha_R = \cos^{-1}\left(\frac{\vec{l}_{34}\cdot\binom{0}{1}}{l_{34}}\right). \tag{3.7}$$

We consider the collision as symmetrical when $\alpha_L/\alpha_R = 1 \pm 0.15$. Knowing the excitation frequency f and using the outcome of equation (3.4), the velocities of the left and the right drops are given by

$$U_L = l_{12}\,f \qquad \text{and} \qquad U_R = l_{34}\,f\,, \tag{3.8}$$

respectively. Applying the law of cosines, using the results of equation (3.6) and (3.8), it follows for the magnitude of the relative velocity of the two drops

$$U = \sqrt{U_L^2 + U_R^2 - 2U_L U_R \cos\alpha}\,. \tag{3.9}$$

For the calculation of b, which defines the distance between the centre of the left drop and the centre of the right drop, normal to the relative velocity vector, the angles β and γ have to be determined. The former is given by

$$\beta = \cos^{-1}\left(\frac{\vec{l}_{31}\cdot\vec{l}_{34}}{l_{31}\,l_{34}}\right) \tag{3.10}$$

and the latter is formed between the relative velocity U and the velocity U_R. Thus, applying the law of sines, γ can be written as

$$\gamma = \sin^{-1}\left(\frac{U_L}{U}\sin\alpha\right). \tag{3.11}$$

Therefore, b can be calculated by

$$b = l_{31}\sin(\beta - \gamma) \tag{3.12}$$

and the non-dimensional impact parameter X can be written as

$$X = \frac{|\,b\,|}{D}\,. \tag{3.13}$$

3.3 Ternary drop collisions

The present section shows the experimental set-up and the mathematical description of ternary drop collisions.

3.3.1 Experimental set-up

In figure 3.5, the experimental set-up used to study collisions of three droplets can be seen. There are two main differences in comparison to the set-up for binary collisions (see figure 3.1). First of all, three drop generators are needed. The generator in the centre is fixed and therefore not moveable. Its droplet stream flows vertically downward in the direction of the y-axis (see figure 3.8). The fact that all three drop generators are driven by exactly the same frequency f leads to the second difference. For ternary drop collisions a second pressurised tank is needed, which is connected to the central generator. The reason for this will be explained in section 3.3.3. All other components of the experimental set-up were already described in section 3.2.1.

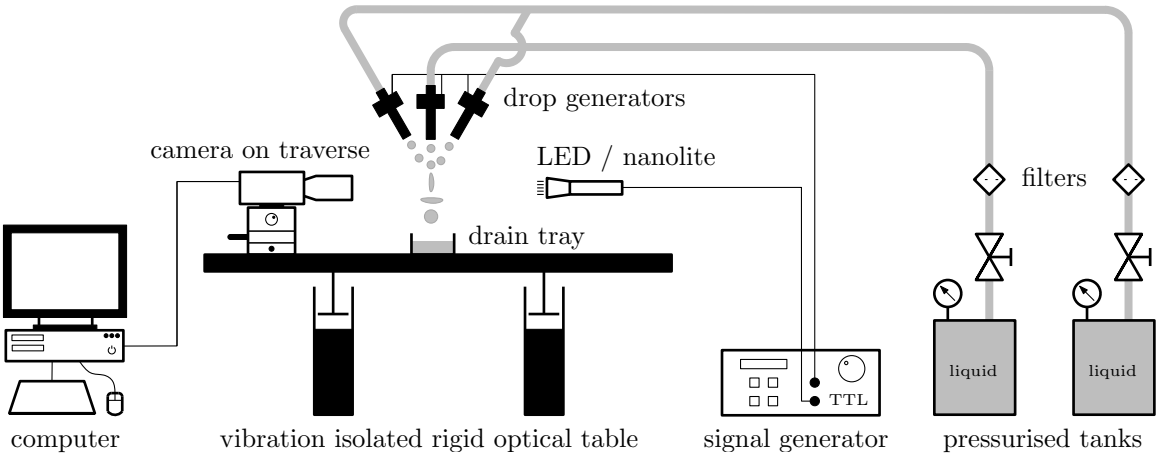

Figure 3.5: Experimental set-up for ternary drop collisions with one liquid.

3.3.2 Image processing

Basically, image processing for ternary drop collisions is similar to the procedure described in section 3.2.2. It is illustrated in figure 3.6. The last three pairs of droplets are selected by cutting the picture. Afterwards the area and the coordinates (x_m, y_m) of the centroid are calculated for each droplet by *ImageJ*. The droplet diameter D is calculated according to equation (3.1). All further calculations are performed with *GNU Octave*.

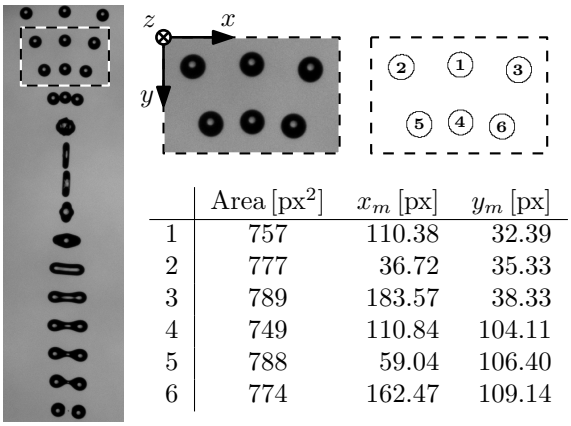

	Area [px^2]	x_m [px]	y_m [px]
1	757	110.38	32.39
2	777	36.72	35.33
3	789	183.57	38.33
4	749	110.84	104.11
5	788	59.04	106.40
6	774	162.47	109.14

Figure 3.6: Example of image processing for ternary drop collision using *ImageJ*. On the left hand, a photograph of the collision can be seen. On the right hand, a table with the results can be found.

3.3.3 Analysis

Basically, there are two possible configurations for symmetrical ternary drop collisions, which can be seen in figure 3.7. For the axially symmetric case, as presented in figure 3.7 **a**, the trajectory of the central droplet stream appears to be the symmetry axis, which is approximately parallel to the y-axis of the coordinate system. In figure 3.7 **b**, the centrally symmetric configuration, with the centre of mass of the central droplet as its point of symmetry, is shown. The two main parameters, relative velocity and non-dimensional impact parameter, are given in table 3.4 for both cases.

In the present thesis only the case of centrally symmetric drop collisions is investigated, since this configuration is better comparable to binary drop collisions, than axially

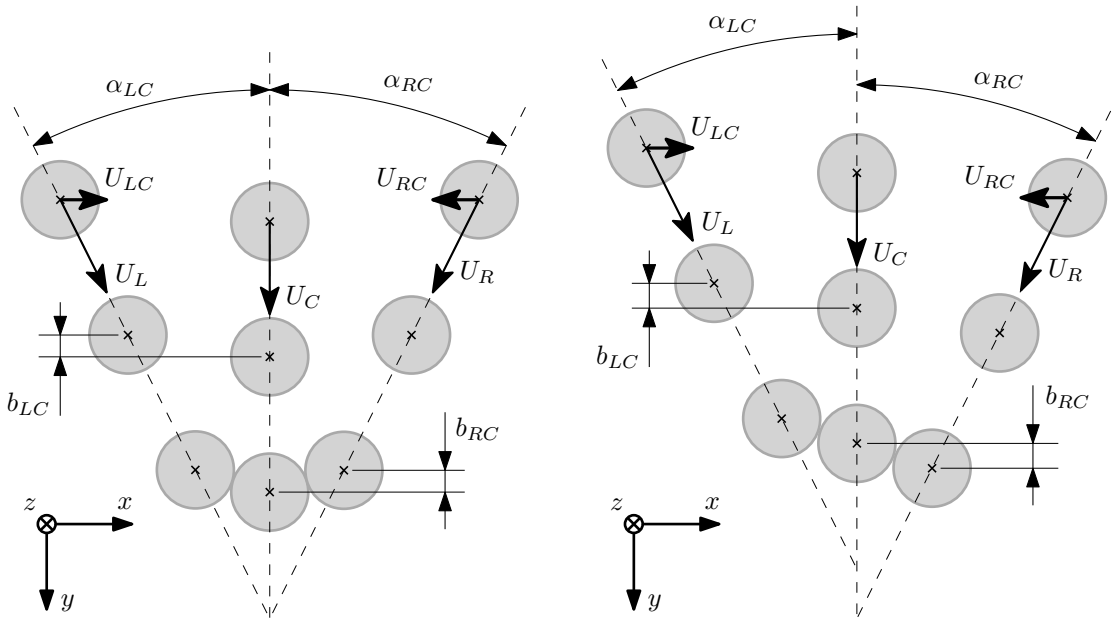

Figure 3.7: Symmetric ternary drop collisions: **a** axially symmetric configuration and **b** centrally symmetric configuration (adapted from Planchette, 2011).

symmetric ternary drop collisions. However, for the investigation of head-on collisions, there is no difference between the two possible configurations of ternary drop collisions, since the impact parameter reduces to zero and the relative velocity is the same for both cases (see table 3.4).

In figure 3.8, a sketch of the relative position for the case of a centrally symmetric ternary drop collision (see figure 3.7 **b**) can be seen. The droplets are numbered from 1 to 6 considering

$$\begin{aligned} x_{m,1} \wedge x_{m,2} \quad &< \quad x_{m,3} \wedge x_{m,4} \quad < \quad x_{m,5} \wedge x_{m,6} \\ y_{m,1} \quad &< \quad y_{m,2} \\ y_{m,3} \quad &< \quad y_{m,4} \\ y_{m,5} \quad &< \quad y_{m,6}\,. \end{aligned} \tag{3.14}$$

The required vectors to estimate the desired quantities $\vec{l}_{12}$, $\vec{l}_{13}$, $\vec{l}_{34}$, $\vec{l}_{53}$ and $\vec{l}_{56}$ can be defined analogous to equation (3.3). Their lengths can be calculated as shown in

figure	relative velocity	impact parameter		
3.7 **a**	$U_{LC} = -U_{RC}$	$b_{LC} = b_{RC}$	$\Rightarrow$	$X_{LC} = X_{RC}$
3.7 **b**	$U_{LC} = -U_{RC}$	$b_{LC} = -b_{RC}$	$\Rightarrow$	$X_{LC} = -X_{RC}$

Table 3.4: Relative velocity and impact parameter for axially and centrally symmetric ternary drop collisions.

equation (3.4). The average droplet diameter is defined by

$$D = \frac{1}{6} \sum_{i=1}^{n=6} D_i \,. \tag{3.15}$$

The angles α_{LC} and α_{RC} are given by

$$\alpha_{LC} = \cos^{-1}\left(\frac{\vec{l}_{12} \cdot \vec{l}_{13}}{l_{12}\, l_{13}}\right) \qquad \text{and} \qquad \alpha_{RC} = \cos^{-1}\left(\frac{\vec{l}_{53} \cdot \vec{l}_{56}}{l_{53}\, l_{56}}\right) \tag{3.16}$$

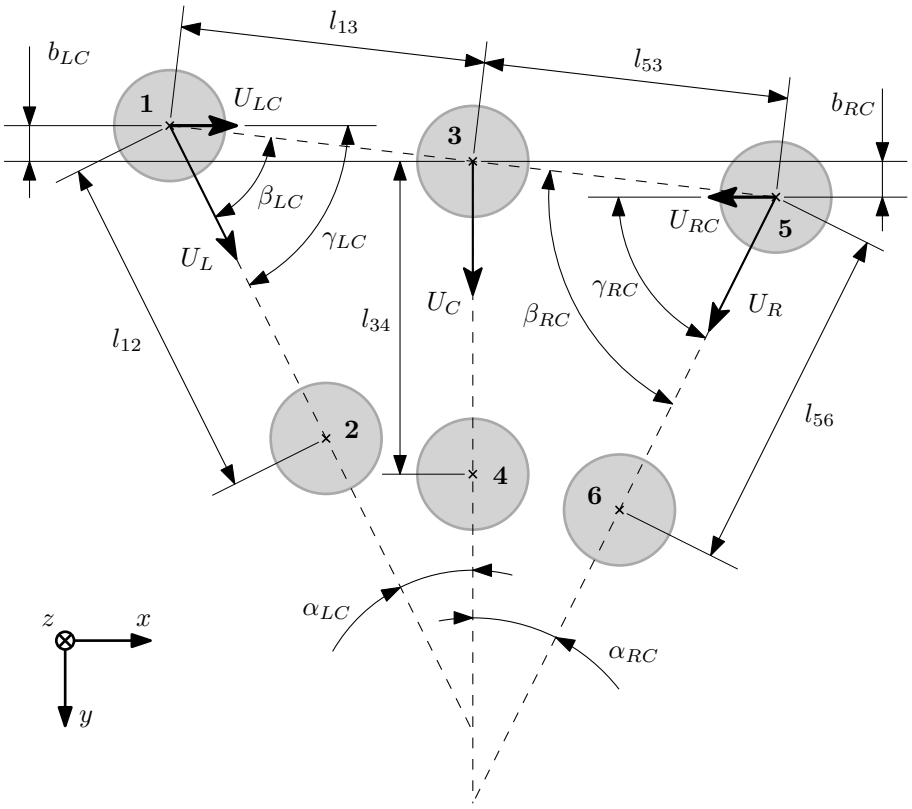

Figure 3.8: Sketch of centrally symmetric collision of three droplets.

and the velocities of the droplets number 1, 2 and 3 can be written as

$$U_L = l_{12} f\,, \qquad U_C = l_{34} f \qquad \text{and} \qquad U_R = l_{56} f\,, \tag{3.17}$$

respectively. In order to achieve symmetric collisions, it is essential that the spacing between two successive droplets follows

$$l_{12} \cos\alpha_{LC} \approx l_{34} \approx l_{56} \cos\alpha_{RC}\,, \tag{3.18}$$

where $\alpha_{LC} \approx \alpha_{RC}$ and $l_{12} \approx l_{56}$. The constraint given by equation (3.18) and the fact that the excitation frequency f is the same for all three drop generators leads to the conclusion that the velocity U_C of the drop in the centre has to be smaller than the velocity of the left and the right drop (see equation (3.17)). Therefore, the central drop generator is connected to a separate pressurised tank, enabling its connection with a smaller pressure and therefore a smaller velocity U_C, as briefly mentioned in section 3.3.1 (see figure 3.5).

As presented in equation (3.9), the relative velocities between left and central droplets U_{LC} and right and central droplets U_{RC} can be calculated by

$$\begin{aligned} U_{LC} &= \sqrt{U_L^2 + U_C^2 - 2U_L U_C \cos\alpha_{LC}}\,, \\ U_{RC} &= \sqrt{U_R^2 + U_C^2 - 2U_R U_C \cos\alpha_{RC}}\,. \end{aligned} \tag{3.19}$$

The overall relative velocity is given by

$$U = U_{LC} + U_{RC} \approx 2\,U_{LC} \approx 2\,U_{RC}\,. \tag{3.20}$$

Analogous to equation (3.10), the angles β_{LC} and β_{RC} are defined by

$$\beta_{LC} = \cos^{-1}\left(\frac{\vec{l}_{12}\cdot\vec{l}_{13}}{l_{12}\,l_{13}}\right) \qquad \text{and} \qquad \beta_{RC} = \cos^{-1}\left(\frac{\vec{l}_{53}\cdot\vec{l}_{56}}{l_{53}\,l_{56}}\right) \tag{3.21}$$

and similar to equation (3.11), the angles γ_{LC} and γ_{RC} are calculated by

$$\gamma_{LC} = \sin^{-1}\left(\frac{U_C}{U_{LC}}\sin\alpha_{LC}\right) \qquad \text{and} \qquad \gamma_{RC} = \sin^{-1}\left(\frac{U_C}{U_{RC}}\sin\alpha_{RC}\right)\,. \tag{3.22}$$

Furthermore, the distances b_{LC} and b_{RC} are given by

$$b_{LC} = l_{13} \sin(\beta_{LC} - \gamma_{LC}) \qquad \text{and} \qquad b_{RC} = l_{53} \sin(\beta_{RC} - \gamma_{RC}) \,, \tag{3.23}$$

which leads to the non-dimensional impact parameters

$$X_{LC} = \frac{b_{LC}}{D_{LC}} \qquad \text{and} \qquad X_{RC} = \frac{b_{RC}}{D_{RC}} \,, \tag{3.24}$$

where D_{LC} and D_{RC} can be calculated by

$$D_{LC} = \frac{1}{4} \sum_{i=1}^{n=4} D_i \qquad \text{and} \qquad D_{RC} = \frac{1}{4} \sum_{i=3}^{n=6} D_i \,, \tag{3.25}$$

respectively. The overall non-dimensional impact parameter is defined as

$$X = \frac{1}{2} \left(|X_{LC}| + |X_{RC}| \right) \approx |X_{LC}| \approx |X_{RC}| \,. \tag{3.26}$$

3.4 Laboratory equipment

In this section the used laboratory equipment is listed below. Accessories like cables and tubes are not considered.

- Drop generator. Provides a monodisperse liquid droplet stream based on the Plateau-Rayleigh instability. Orifice changeable. Developed by Brenn *et al.* (1996).
- Linear and rotary micro-control stages for drop generator. OWIS.
- Pressure vessel. Capacity: 10 l. Difference pressure up to 10 bar. SATA.
- Air pressure regulator. Norgren Watson Smith.
- Signal generator. FLUKE 282 40MB/s ARBITRARY WAVEFORM GENERATOR.
- Camera. PCO Sensicam qe 670KE. Cooled 12-bit CCD camera system. Resolution: 1376×1040 px.

- Objective. Super Cosina 75-300 mm 1:4.5-5.6 Macro camera lens. A C-mount adapter is used to connect the objective to the camera.
- Magnification lens. Raynox CM-3500 MicroExplorer lens (6x and 12x magnification).
- Linear micro-control stages for camera. OWIS.
- Stage micrometer. A.KRÜSS Optronic MML 1003.
- Vibration isolated rigid optical table. Newport LabLegs SL Series.
- NANOLITE flash light. Typical flash duration of a few nanoseconds. Power supply of the flash light. HSPS (High-Speed Photo Systems).
- Red light LED. Typical flash duration of approximately 1 μs. Manufactured at the Institute of Fluid Mechanics and Heat Transfer at the Graz University of Technology.
- Computer.

4 Results and discussion

In the first part of this chapter the collision regime maps for binary and ternary liquid drop collisions are presented and compared. The second part focuses on the onset of fragmentation for head-on collisions.

4.1 Collision regime maps

In this section, the obtained (X, We) nomograms at constant Ohnesorge number for binary and ternary collisions of equal-sized droplets are presented and discussed. Moreover, similarities and differences between both collision regime maps are pointed out. The used liquid is an aqueous glycerol solution with 50% mass of glycerol and the nozzle diameter of the drop generators is 200 μm.

4.1.1 Binary drop collisions

In this section the different collision outcomes for binary liquid drop collisions are presented. The Ohnesorge number for all collisions is 0.032 ± 0.001. Four classical collision outcomes can be identified: coalescence, bouncing, reflexive separation and stretching separation (see figure 2.9). These collision outcomes are shown and discussed below. In all the images shown below, the droplets are seen to move from the left to the right.

First of all, head-on collisions with increasing Weber numbers are discussed allowing to observe the transition between coalescence (see figure 4.1) and reflexive separation (see figure 4.2). In figure 4.1 **a**, two drops merge at $We = 12.7$. The collision energy is not very high. For this reason it takes some time to expel the intervening air layer between the drops. As a result both drops start to flatten a bit before the liquid bridge

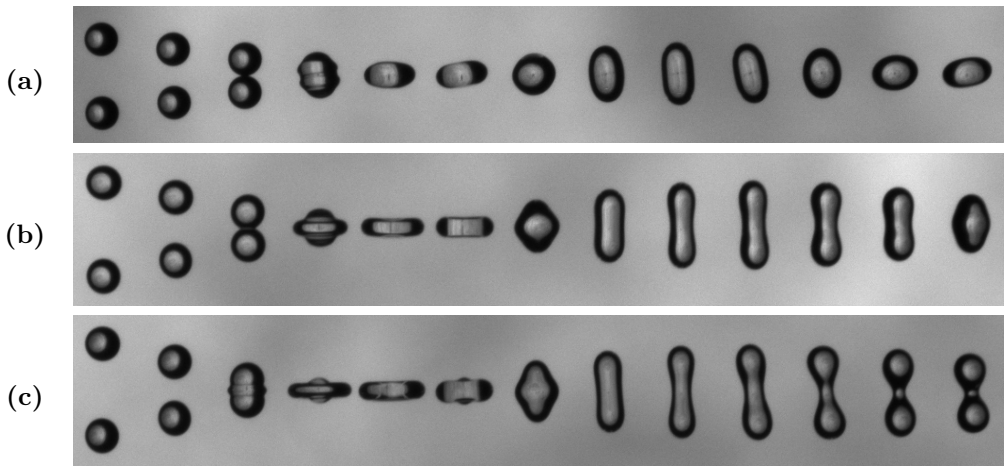

Figure 4.1: Photographs of pairs of coalescing drops, using glycerol 50% as the liquid, at zero impact parameter: **a** $D = 341\,\mu$m, $We = 12.7$, $X = 0.04$, $f = 7060\,$Hz **b** $D = 335\,\mu$m, $We = 25.1$, $X = 0.02$, $f = 7060\,$Hz **c** $D = 338\,\mu$m, $We = 35.7$, $X = 0.02$, $f = 7060\,$Hz.

is formed. After coalescence, the excess surface and internal kinetic energy is dissipated via oscillations.

In figure 4.1 **b**, the Weber number is increased to 25.1, which can be realised by increasing the pressure in the reservoir (see figure 3.1) or by increasing the angle between the trajectories of the two droplet streams (see figure 3.4). The merged droplets expand into a slim disk shaped complex, then retract into a cylindrical rod and finally into a spherical drop. Coalescence at a Weber number of 35.7 can be seen in figure 4.1 **c**. After the cylindrical rod is formed, internal forces continue to push both ends outwards and as a result the complex deforms into a dumbbell. Nevertheless, the internal motion is not strong enough to break this ligament and, consequently, it retracts into a spherical droplet.

By further increasing the Weber number (see figure 4.2), the internal momentum rate exceeds the surface tension force and reflexive separation occurs. This can be seen in figure 4.2 **a** ($We = 37.3$), where in the last stage of the collision the two droplets separate again and a small satellite droplet is formed. As the Weber number is further increased, the size of the satellite droplet grows, which can be observed in figures 4.2 **b** and 4.2 **c**. Moreover, in figure 4.2 **b**, it can be nicely seen how the droplets are pinched off the connecting ligament. In general, the ligament can contract to form a single droplet, as shown in the photograph, or break up into several satellite droplets.

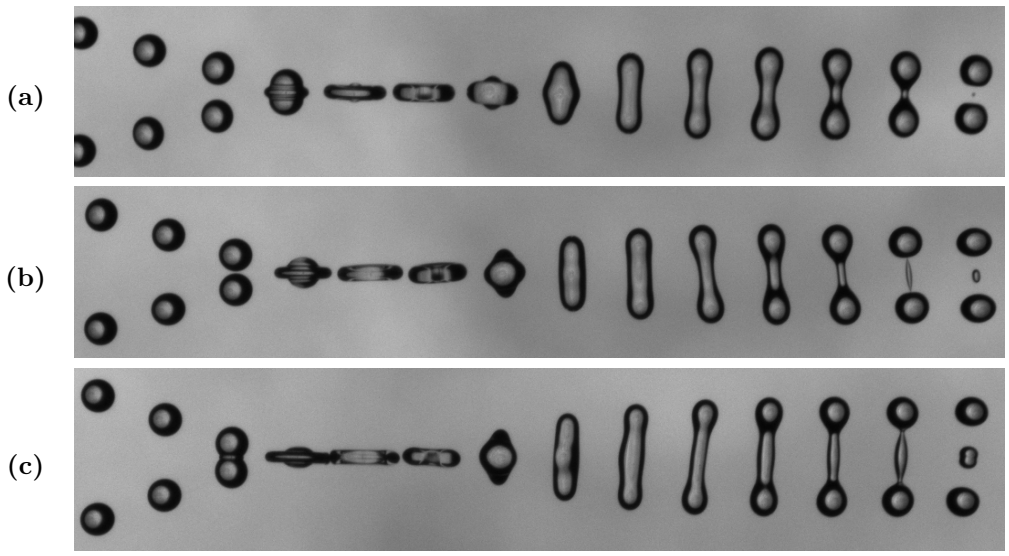

Figure 4.2: Examples of reflexive separation at binary drop collisions, using glycerol 50% as the liquid, at zero impact parameter: **a** $D = 337\,\mu\text{m},\ We = 37.3,$ $X = 0.01,\ f = 7060\,\text{Hz}$ **b** $D = 339\,\mu\text{m},\ We = 47.8,\ X = 0.01,\ f = 7060\,\text{Hz}$ **c** $D = 339\,\mu\text{m},\ We = 68.6,\ X = 0.04,\ f = 7060\,\text{Hz}.$

As the Weber number is increased to around 68, which can be seen in figure 4.2 **c**, the limitation of the used droplet production technique is reached. The disk emerging from the collision expands to a degree that it interacts with the preceding disk. In the current case, the collision is not affected, but, for larger Weber numbers, successive disks may coalesce, which affects the collision outcome to a great extent. This aspect is not critical for the development of a collision regime map, but can become a limiting factor for the investigation of the onset velocity of high-viscous liquids, for example with an aqueous glycerol solution at 75% mass of glycerol (typical dynamic viscosity of 35.5 mPa s at 20 °C).

In figures 4.1 **a** and 4.3, coalescence at constant Weber numbers and different non-dimensional impact parameters can be compared. In figure 4.1 **a** the impact parameter is around zero, whereas in figure 4.3 the non-dimensional impact parameter is in the order of 0.48. Nevertheless, apart from the displacement of the droplet trajectories, the

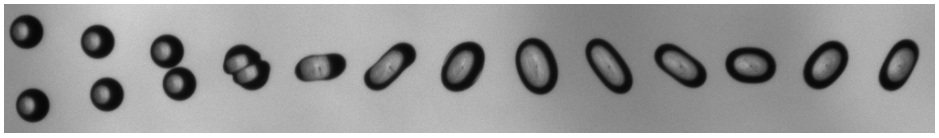

Figure 4.3: Coalescence at binary drop collision, using glycerol 50% as the liquid, at $D = 341\,\mu\text{m},\ We = 13.2,\ X = 0.48,\ f = 7060\,\text{Hz}.$

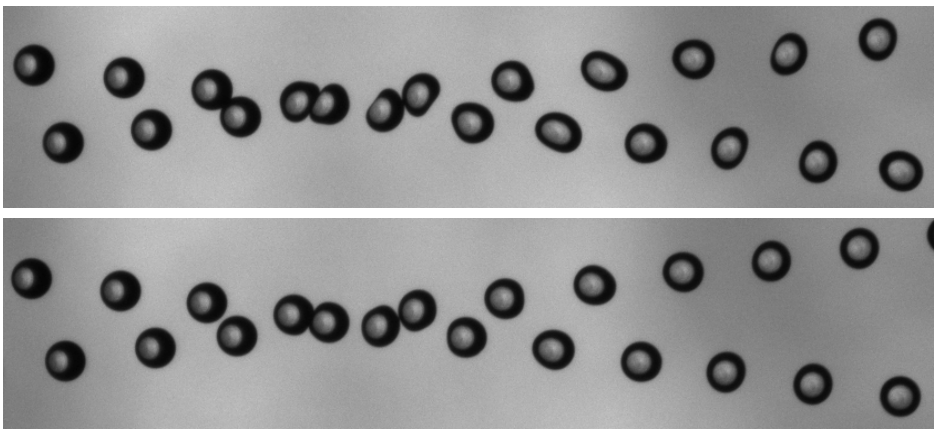

Figure 4.4: Bouncing at binary drop collisions, using glycerol 50% as the liquid, at **a** $D = 339\,\mu$m, $We = 13.0$, $X = 0.57$, $f = 7060\,$Hz **b** $D = 337\,\mu$m, $We = 13.2$, $X = 0.92$, $f = 7060\,$Hz.

collision process looks similar in both cases. As the non-dimensional impact parameter is increased to 0.57, which is presented in figure 4.4 **a**, bouncing occurs. Due to the small contact area both droplets deform oblique and bounce apart without forming a liquid bridge. The deformation is quite significant and therefore it takes some time until both droplets regain their spherical shape. In figure 4.4 **b**, bouncing at a large non-dimensional impact parameter can be seen. Hence the contact area is very small, barely no deformation of the drops can be noticed. Thus, they recover their spherical shape quickly.

In figure 4.5, two photographs at $X \approx 0.25$ are presented. For the collision in figure 4.5 **a**, the Weber number has a magnitude of 36.2 and in figure 4.5 **b**, $We = 69.4$. It is interesting to note that, for a Weber number comparable to the one of figure 4.5 **b**

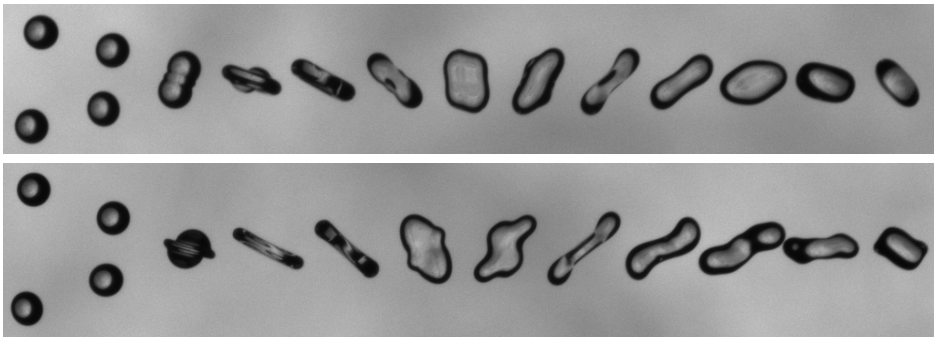

Figure 4.5: Coalescence at binary drop collisions, using glycerol 50% as the liquid, at small impact parameters: **a** $D = 338\,\mu$m, $We = 36.2$, $X = 0.25$, $f = 7060\,$Hz **b** $D = 368\,\mu$m, $We = 69.4$, $X = 0.23$, $f = 5310\,$Hz.

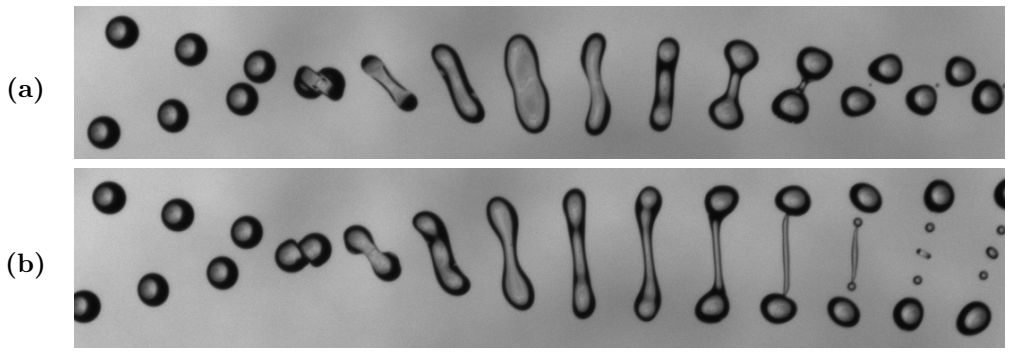

Figure 4.6: Stretching separation at binary drop collisions, using glycerol 50% as the liquid, at **a** $D = 349\,\mu$m, $We = 35.7$, $X = 0.54$, $f = 7060\,$Hz **b** $D = 338\,\mu$m, $We = 36.2$, $X = 0.75$, $f = 7060\,$Hz.

($We = 68.6$) and smaller impact parameter ($X = 0.04$), reflexive separation occurs (see figure 4.2 **c**). This can be explained by the fact that the amount of impact inertia along the imaginary line connecting the centroids of the droplets is decreased with increasing impact parameter. In other words, for head-on collisions all impact inertia is reflected towards the outside. At non-zero impact parameters, due to the position of the droplets at the impact, part of internal liquid motion is tangential and the remaining energy responsible for reflexive separation is reduced. From this follows that, with increasing impact parameter, the critical impact inertia leading to reflexive separation increases.

As a next step, stretching separation at intermediate Weber numbers is discussed. Taking the configuration of figure 4.5 **a** (coalescence) at $We \approx 36$ as a reference, the impact parameter is increased. Above a certain impact parameter, stretching separation occurs, which can be seen in figure 4.6 **a**. This process is inertia dominated, which can

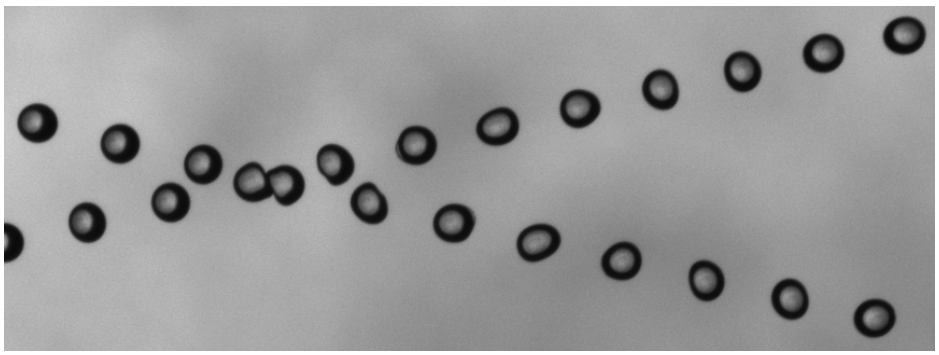

Figure 4.7: Bouncing at binary drop collision, using glycerol 50% as the liquid, at $D = 338\,\mu$m, $We = 35.7$, $X = 0.83$, $f = 7060\,$Hz.

be observed more clearly in figure 4.6 **b**, where the non-dimensional impact parameter of $X = 0.75$ is larger than in figure 4.6 **a**. After the impact a liquid bridge is formed, but the main parts of both droplets remain on their respective trajectories. Thus, the connecting ligament is stretched and finally pinches off from both drops at its ends. In further consequence, the ligament breaks into three satellite droplets, due to a non-uniform pressure field within the ligament resulting from surface tension. Thus, spherical drops are formed at both ends of the ligament and pinched off. This mechanism is called *end-pinching* (Stone *et al.*, 1986). If the impact parameter is increased, the regime of stretching separation ends and both droplets bounce off each other. This can be seen in figure 4.7.

Let us now discuss the collision outcomes at high Weber numbers for $We > 100$. Starting at $We = 100.1$ and a small impact parameter, as presented in figure 4.8 **a**, reflexive separation can be observed. The breakup mechanism appears to be different from the breakup mechanism at intermediate Weber numbers (see figure 4.2). In figure 4.2, the Rayleigh criterion can be identified as the reason for breakup of the cylinder into two main droplets after its length-to-diameter ratio exceeds a value of π. At high Weber numbers, the merged complex stretches into a very long cylindrical rod, with a much higher aspect ratio. Disturbances at the surface of the cylinder from recoiling lead to its pinch off at both ends. This mechanism is identical to the above mentioned *end-pinching* mechanism, which is responsible for the breakup of ligaments

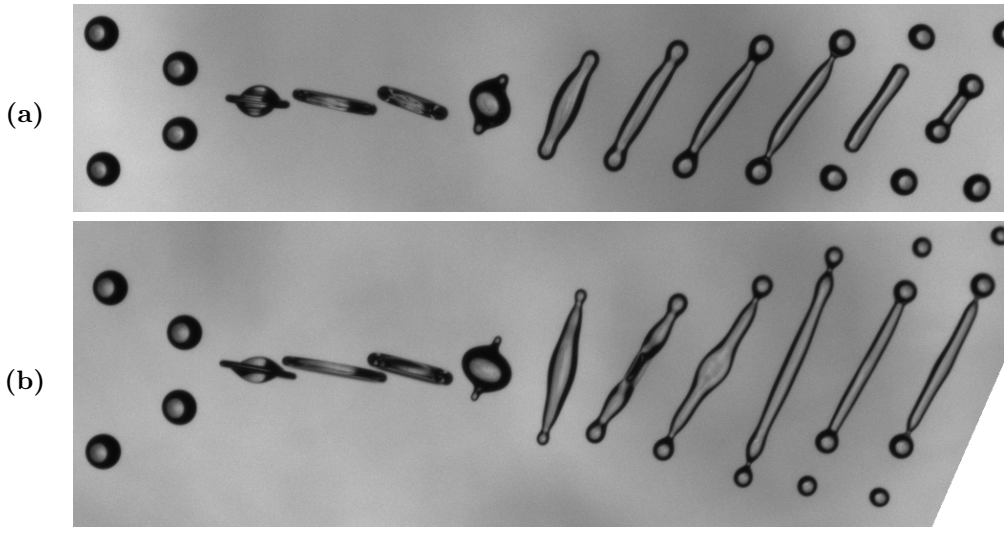

Figure 4.8: Reflexive separation as a result of binary drop collisions, using glycerol 50% as the liquid, at large Weber numbers: **a** $D = 366\,\mu$m, $We = 100.1$, $X = 0.08$, $f = 5310\,$Hz **b** $D = 369\,\mu$m, $We = 152.3$, $X = 0.11$, $f = 5250\,$Hz.

into satellite droplets. The produced droplets are smaller in size than the initial drops. For a Weber number of 152.3, which can be seen in figure 4.8 **b**, the formed cylinder is longer than in figure 4.8 **a**. The pinched off droplets seem to grow in size from the outside to the inside. It is also interesting to note that the maximum diameter of the disk emerging in the first phase after the collision is now almost four times the initial droplet diameter.

In figure 4.9, two photographs of reflexive separation at intermediate non-dimensional impact parameters can be seen. Both happen to be close to the transition to another regime. First, in figure 4.9 **a**, reflexive separation at an intermediate Weber number ($We = 47.5$) and at $X = 0.15$ is pictured. The collision process looks similar to a head-on collision at an equal Weber number, which is shown in figure 4.2 **b**. The only difference is that, due to arising tangential forces at non-zero impact parameters, the whole merged complex is rotated by a certain angle. The second photograph, given in figure 4.9 **b**, shows reflexive separation at a large Weber number and $X = 0.22$. This process is quite different from head-on reflexive separation (see figure 4.8 **a**). Due to the rotational momentum, the internal motion of the flow is not strong enough to form a long cylindrical rod. In fact the complex retracting from the disk is not much longer than in figure 4.2 **b**. Finally, the complex breaks up into three uniform-sized droplets.

In the next section, stretching separation at high Weber numbers of $We \approx 100$ is discussed. To do so, two photographs are reproduced in figure 4.10. In figure 4.10 **a**, at a non-dimensional impact parameter of $X = 0.44$, a broad liquid bridge is formed,

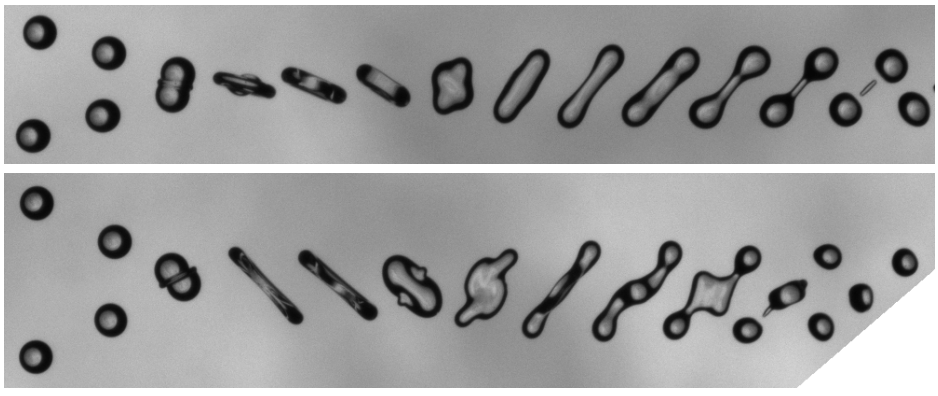

Figure 4.9: Reflexive separation as a result of binary drop collisions, using glycerol 50% as the liquid, at small impact parameters: **a** $D = 339\,\mu$m, $We = 47.5$, $X = 0.15$, $f = 7060\,$Hz **b** $D = 363\,\mu$m, $We = 115.7$, $X = 0.22$, $f = 5310\,$Hz.

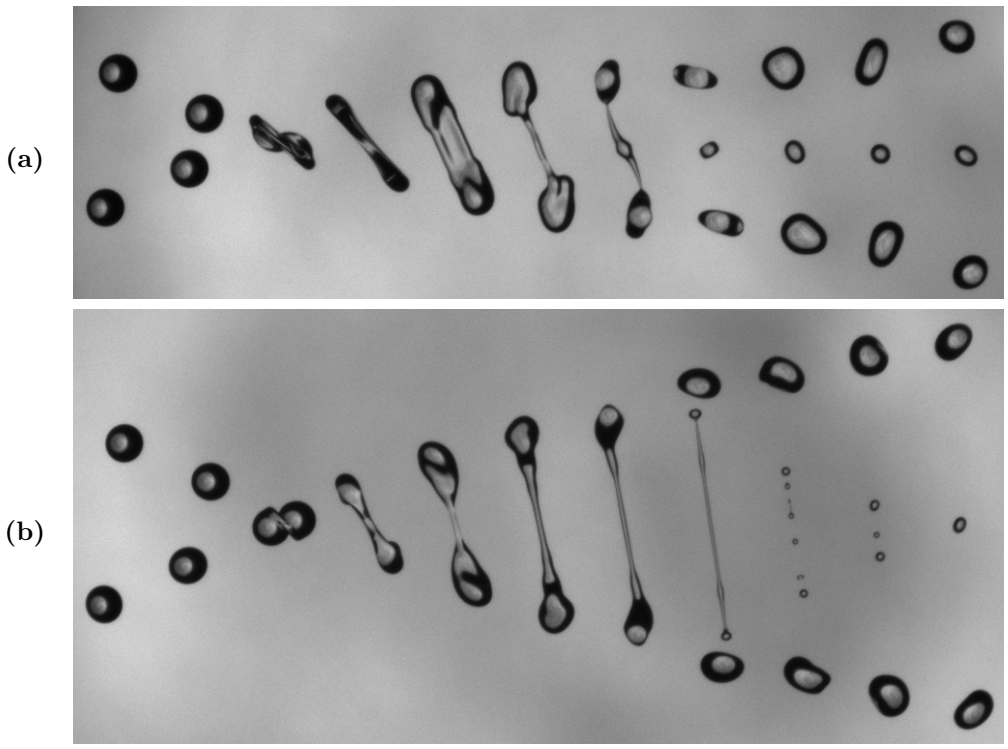

Figure 4.10: Stretching separation at binary drop collisions, using glycerol 50% as the liquid, at large Weber numbers: **a** $D = 363\,\mu$m, $We = 101.7$, $X = 0.44$, $f = 5310\,$Hz **b** $D = 365\,\mu$m, $We = 99.4$, $X = 0.67$, $f = 5310\,$Hz.

which subsequently collapses into a ligament and breaks up into a single satellite droplet. On the contrary, at a larger impact parameter, which can be seen in figure 4.10 **b**, a longer ligament is formed. This ligament breaks up into many satellites. Because of the inward directed motion of the outer satellites, they merge again into one resulting satellite droplet. Due to a larger impact parameter, the droplets in figure 4.10 **b** are not as much deflected from their initial trajectories as the droplets in figure 4.10 **a**.

The collision regime map for binary drop collision is created by plotting the outcomes of many different collisions for the various pairs (X, We) into a single nomogram. This can be seen in figure 4.11. The used liquid is glycerol 50% and the average Ohnesorge number for this map is in the order of 0.032. In figure 4.12, the (X, We) coordinates and the figure numbers of the previously presented photographs can be seen.

The transitions between the four different regimes are drawn as grey lines. They are a result of observation and neither based on theoretical nor on empirical correlations.

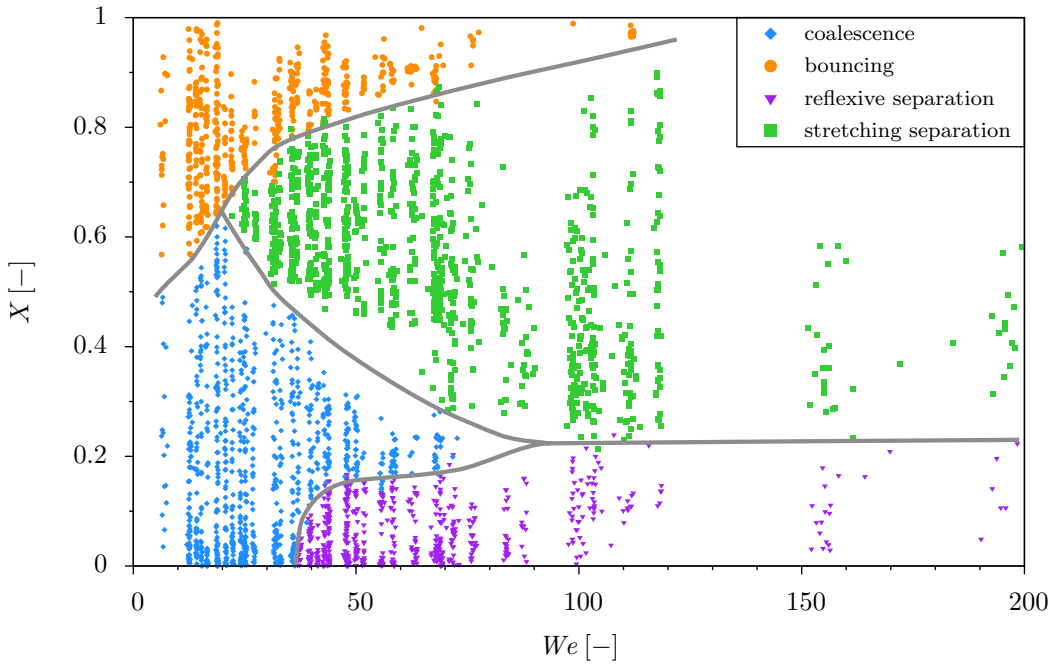

Figure 4.11: Collision regime map obtained for binary drop collisions, using glycerol 50% as the liquid, in an atmospheric environment at $T \approx 23\,°\mathrm{C}$. The droplet diameter ranges between 325 μm and 378 μm, leading to an average Ohnesorge number of $Oh \approx 0.032$. The relative velocity is varied in the range of $1.0\,\mathrm{m\,s^{-1}} \leq U \leq 5.9\,\mathrm{m\,s^{-1}}$, which leads to Weber numbers between 6 and 217. The transitions are sketched as grey lines.

At small Weber numbers ($We < 20$) only two collisions outcomes, depending on the non-dimensional impact parameter, are possible. For $X \lesssim 0.5$ both drops merge permanently and otherwise bouncing occurs. With increasing Weber number, this border is shifted to larger impact parameters. This observation was expected, since more kinetic energy is available to expel the air layer between the droplets which prevents bouncing.

From a Weber number of approximately 20 on, a third collision outcome, namely stretching separation, can be observed. It occurs at relatively high impact parameters, when parts of both droplets temporarily merge, but due to the relatively high kinetic energy, the non-merging parts of the droplets remain on their initial trajectories and the liquid bridge temporarily connecting them breaks up. Consequently, for Weber numbers larger than around 20, there is no transition between coalescence and bouncing, but only between stretching separation and bouncing. With increasing Weber number, this transition is shifted to larger impact parameters, until the regime of bouncing vanishes

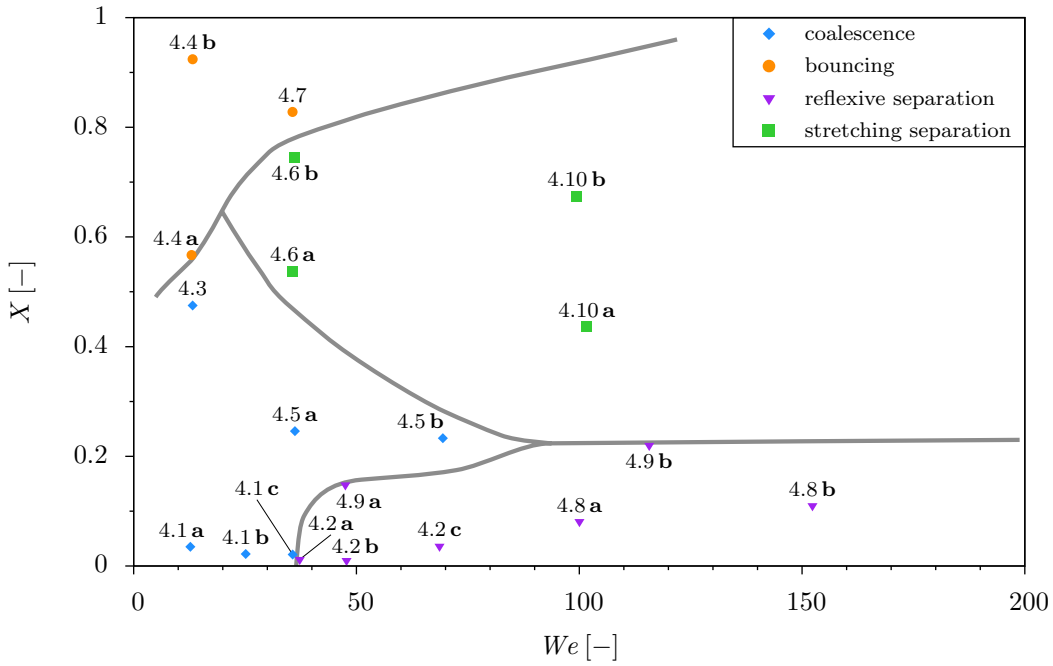

Figure 4.12: Coordinates of the presented photographs in the binary collision regime map, which is given in figure 4.11.

completely at $We \approx 120$. On the contrary, the transition between coalescence and stretching separation is shifted to smaller impact parameters with increasing Weber number. Thus, the probability of stretching separation in the (X, We) nomogram increases with increasing kinetic energies (see figure 4.11).

Reflexive separation occurs first at a Weber number of around 37 at $X = 0$. In this case, the initial kinetic energy is sufficiently large to separate the temporarily merged droplets again. The transition to coalescence is observed for constant Weber number ($We \approx 40$) and increasing non-dimensional impact parameter ($0 \rightarrow 0.15$) as well as for almost constant X (≈ 0.15) and increasing Weber number ($40 \rightarrow 90$). At a Weber number of approximately 90, the three regimes of coalescence, reflexive separation and stretching separation meet on the map. The transition between the latter two appears to be found for almost constant non-dimensional impact parameter ($X \approx 0.22$) for all investigated Weber numbers. Consequently, coalescence occurs only for $We < 90$. It has to be stated that this value is approximated, because it is difficult to distinguish between the different regimes in this transition area. This can be seen in figure 4.11, where no data points are plotted in this region. The reason for this lies in the fact that the collision outcome in this parameter range is very sensitive to any perturbations.

The nomogram for binary drop collisions, using glycerol 50% as the liquid, looks very similar to the nomograms for hydrocarbon droplets obtained by Qian & Law (1997) (see figure 2.8 **b**) and Jiang *et al.* (1992). One main difference is that bouncing for head-on collisions at the very small Weber number of 6 (see figure 2.8 **b**) could not be observed during this work. At this Weber number, bouncing occurred for non-dimensional impact parameters larger than around 0.57. Maybe for smaller Weber numbers, bouncing at zero impact parameter could be observed using the current configuration.

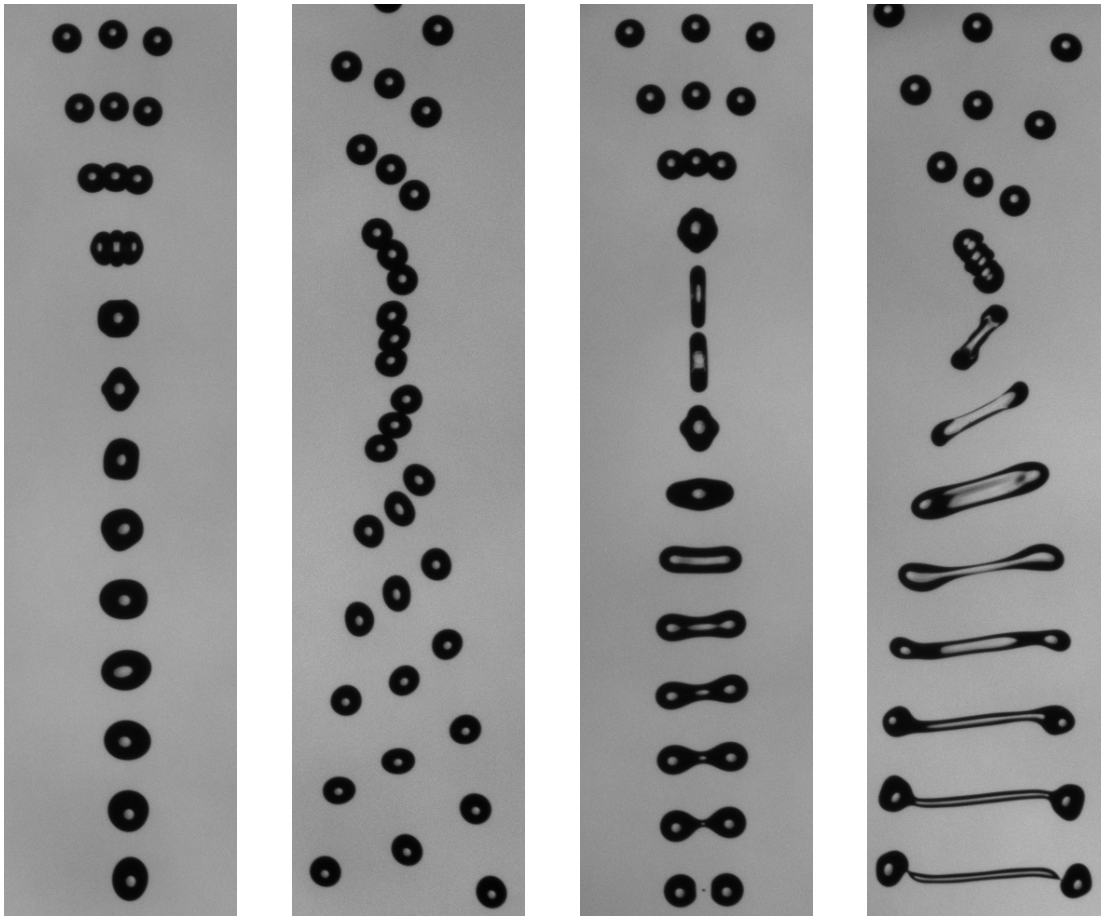

(a) **(b)** **(c)** **(d)**

Figure 4.13: The four main collision outcomes observed for centrally symmetric ternary drop collisions using glycerol 50% as the liquid: **a** coalescence at $D = 363\,\mu$m, $We = 15.1$, $X = 0.13$, $f = 5429\,$Hz **b** bouncing at $D = 384\,\mu$m, $We = 23.6$, $X = 0.81$, $f = 5529\,$Hz **c** reflexive separation at $D = 359\,\mu$m, $We = 48.3$, $X = 0.01$, $f = 5560\,$Hz **d** stretching separation at $D = 374\,\mu$m, $We = 85.9$, $X = 0.53$, $f = 5710\,$Hz.

4.1.2 Ternary drop collisions

In this section, the observed collision outcomes and the map of regimes for centrally symmetric ternary drop collisions (see figure 3.7 **b**) are presented. The used liquid again the aqueous glycerol solution at 50% mass of glycerol (see table 3.1). In general, similar to binary drop collisions, four different collision outcomes, namely coalescence, bouncing, reflexive separation and stretching separation were observed. They are exemplarily pictured in figure 4.13. At first glance, the collision mechanisms look similar to binary drop collisions (see figure 2.9 and section 4.1.1). However, significant differences will be shown later on.

The different collision outcomes are shown and discussed below. On the following pictures the droplets move from the left to the right. A white vertical line within an image indicates that it consists of two photographs. This is necessary in some cases in order to observe the collision farther downstream without lessening the magnification of the acquired images.

In figure 4.14, three examples of coalescence in ternary head-on collisions can be seen. At a small Weber number, in figure 4.14 **a**, all three droplets are almost equally deformed before the liquid bridge is formed. Then they merge permanently. Due to small kinetic energy, the combined complex deforms very little and relaxes very fast into a spherical droplet. At a Weber number of 27 (calculated with the relative velocity

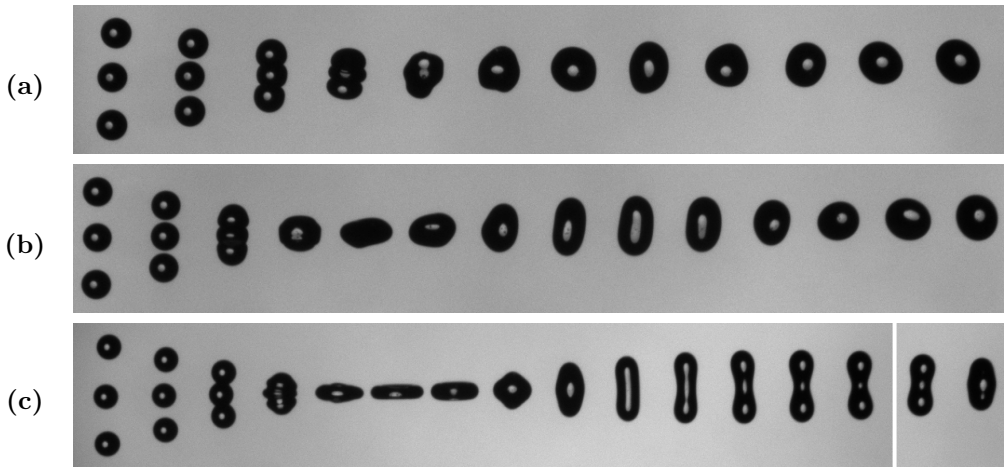

Figure 4.14: Coalescence at ternary head-on collisions, using glycerol 50% as the liquid, at **a** $D = 375\,\mu$m, $We = 10.2$, $X = 0.06$, $f = 4131\,$Hz **b** $D = 359\,\mu$m, $We = 27$, $X = 0.06$, $f = 5560\,$Hz **c** $D = 359\,\mu$m, $We = 42.9$, $X = 0.05$, $f = 6810\,$Hz.

given by equation (3.20)), which can be seen in figure 4.14 **b**, the central droplet is more deformed than the two outer droplets after the impact. Moreover, the merged droplet is deformed into a spheroid. The kinetic energy is still very small. Thus, after relaxation and a few oscillations, a spherical droplet is obtained. In figure 4.14 **c**, coalescence at $We = 42.9$ can be observed. The central drop is highly squeezed by the two impinging drops and, as a consequence of the high kinetic energies, a narrow disk is formed. After this disk reaches its maximum extension, the liquid retracts due to surface tension and relaxes afterwards into a cylindrical rod. As the forces which push both ends of this cylinder outwards cannot overcome the inward pulling surface tension force, the excess energy is dissipated through oscillations and the merged complex reaches a spherical shape.

Coalescence at larger impact parameters is pictured in figure 4.15. For a small Weber number of 14.7 and a quite high non-dimensional impact parameter of 0.51, which can be seen in figure 4.15 **a**, the process of the collision is similar to the head-on case given in figure 4.14 **a**. All three droplets are flattened equally as the intervening air layer is expelled. After the liquid bridge is formed, only moderate deformations occur due to oscillations. In figure 4.15 **b**, three coalescing droplets at $We = 47.2$ and a moderate impact parameter of 0.24 are pictured. The droplets merge and expand into a narrow disk followed by relaxation into a rod-shaped complex. Despite the inclination of the merged complex, due to the non-zero impact parameter, this process is quite similar to the head-on collision presented in figure 4.14 **c**.

At small Weber numbers, if the impact parameter exceeds a critical value, the drops do not coalesce any more. Instead they bounce off each other, since the intervening air

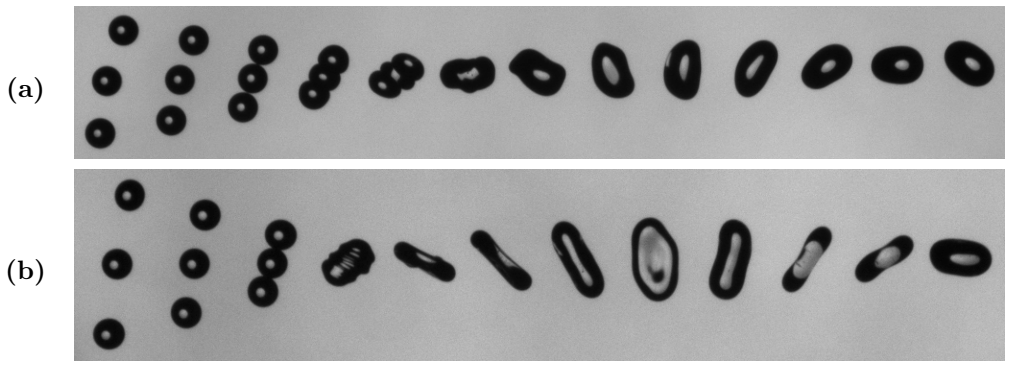

Figure 4.15: Coalescence at ternary collisions, using glycerol 50% as the liquid, at non-zero impact parameter: **a** $D = 362\,\mu$m, $We = 14.7$, $X = 0.51$, $f = 5429\,$Hz **b** $D = 371\,\mu$m, $We = 47.2$, $X = 0.24$, $f = 5500\,$Hz.

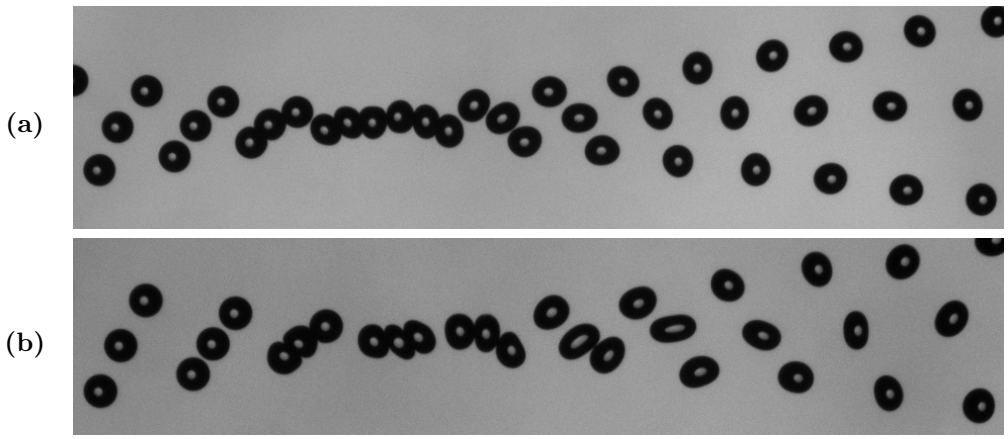

Figure 4.16: Bouncing at ternary collisions, using glycerol 50% as the liquid, at small Weber numbers: **a** $D = 363\,\mu\text{m}$, $We = 14.7$, $X = 0.75$, $f = 5429\,\text{Hz}$ **b** $D = 384\,\mu\text{m}$, $We = 23.8$, $X = 0.6$, $f = 5529\,\text{Hz}$.

layer between the droplets cannot be expelled. This phenomenon can be seen in figure 4.16 **a** at $We = 14.7$ and $X = 0.75$ for a ternary drop collision. The impact kinetic energy is very small and therefore the droplets are only slightly deformed. Obviously, the deformation of the central droplet is larger than the deformation of the two outer drops. Interactions between two successive droplet triplets can occur, due to the limited space between two successive drops in the droplet streams. In this case, a force is applied which pushes each triplet closer together. Since this additional force has no impact on the outcome regime, the results can be included in the collision regime map (see figure 4.26). In figure 4.16 **b**, bouncing can be observed at $We = 23.8$ and $X = 0.6$. In contrast to figure 4.16 **a**, the central droplet is stronger deformed due to the higher kinetic energy of the outer droplets and the smaller impact parameter.

Stretching separation at ternary drop collisions is introduced in the next paragraph. It can be seen in figure 4.17 at $We = 47$ and $X = 0.42$. The outer droplets squeeze the central drop until a liquid bridge is formed. Due to inertia, the outer drops stay on their trajectories and stretch the connecting ligament until the complex breaks

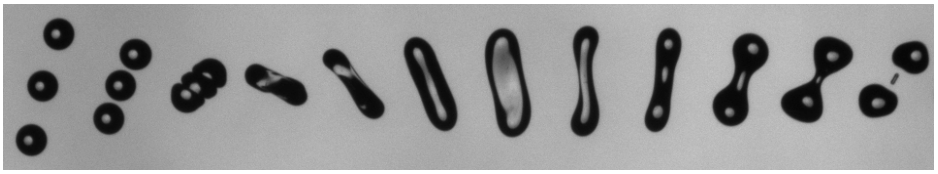

Figure 4.17: Stretching separation at ternary collisions, using glycerol 50% as the liquid, at $D = 370\,\mu\text{m}$, $We = 47$, $X = 0.42$, $f = 5500\,\text{Hz}$.

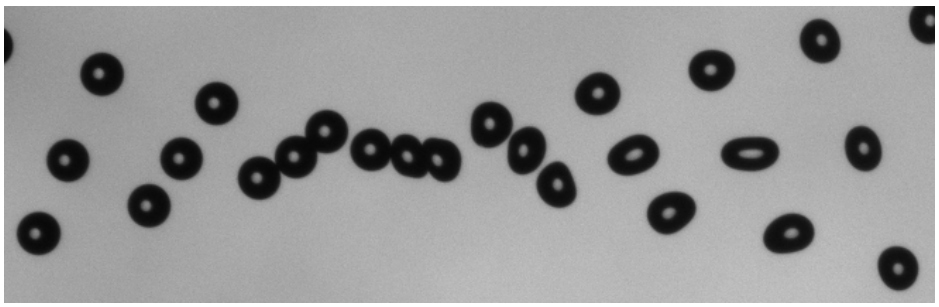

Figure 4.18: Bouncing at ternary collisions, using glycerol 50% as the liquid, at $D = 380\,\mu\text{m}$, $We = 43.6$, $X = 0.88$, $f = 5120\,\text{Hz}$.

up into two large droplets and one small satellite droplet. Decreasing the impact parameter at this Weber number stabilises the collision, leading to coalescence, which can be seen in figure 4.15 **b**. A further increase of the impact parameter would lead to bouncing droplets. This can be seen in figure 4.18 for a very large non-dimensional impact parameter of 0.88. Despite this large impact parameter, the central droplet is noticeably deformed, because it is squeezed from two sides.

In figure 4.19, two photographs picturing reflexive separation at ternary drop collisions can be seen. Starting from small Weber numbers, reflexive separation occurs for the first time at a Weber number of around 47, which can be seen in figure 4.19 **a**. Similar to figure 4.14 **c**, the central droplet is highly squeezed after the impact, and the merged complex is deformed into a narrow disk. After the relaxation, a cylindrical rod is formed. With its internal flow pushing both ends further outwards, a dumbbell with a thin connecting ligament is formed. Finally, this ligament breaks up, and two droplets larger than the initial droplets with a small satellite droplet in between are formed.

(a)

(b)

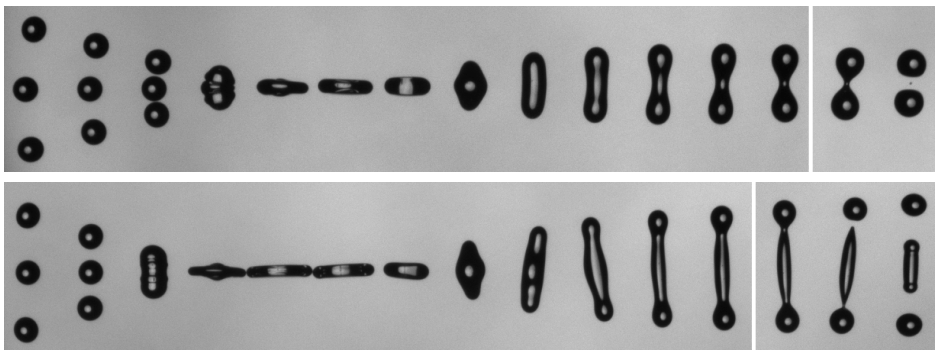

Figure 4.19: Reflexive separation at ternary head-on collisions, using glycerol 50% as the liquid, at **a** $D = 372\,\mu\text{m}$, $We = 47.6$, $X = 0.03$, $f = 5500\,\text{Hz}$ **b** $D = 372\,\mu\text{m}$, $We = 87.3$, $X = 0.03$, $f = 5710\,\text{Hz}$.

At a larger Weber number, say 87.3, the process of the collision is different from the collision pictured in figure 4.19 **a**. This can be seen in figure 4.19 **b**, where after the relaxation of the disk, a long cylindrical rod is formed. At both of its ends a drop with around the initial droplet size is pinched off. The remaining ligament in the centre contracts to a third droplet.

Reflexive separation at a non-zero impact parameter of $X = 0.11$ is pictured in figure 4.20. The Weber number is in the same range as in figure 4.19 **b**. Due to the tangential part of the impact inertia, the merged complex is turned around a certain rotation angle. Thus, after the relaxation of the disk, the formed cylindrical rod is not as long as the rod established in the head-on case. The breakup results in three almost equally sized droplets.

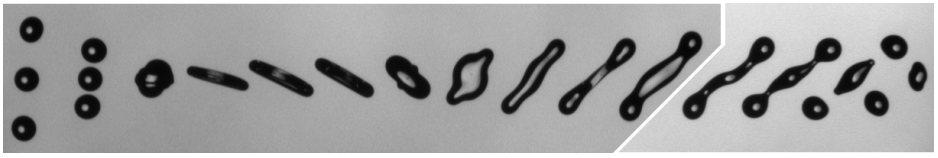

Figure 4.20: Reflexive separation at ternary collision, using glycerol 50% as the liquid, at $D = 373\,\mu\text{m},\ We = 86.4,\ X = 0.11,\ f = 5710\,\text{Hz}$.

Note that it is not always clearly visible on the photographs if reflexive or stretching separation occurs. For example, the collisions in figure 4.17 (stretching separation) and figure 4.20 (reflexive separation) look quite identical. In figure 4.17, the outer droplets principally stay on their initial trajectories. This means that the droplet on the right before the collision can be found on the left after the collision. This is an indication for stretching separation, which cannot be obviously seen in figure 4.20. Here, reflexive behaviour can be observed as well. Another way to estimate the collision outcome is to look at its position in the collision regime map, which will be introduced below in figure 4.26.

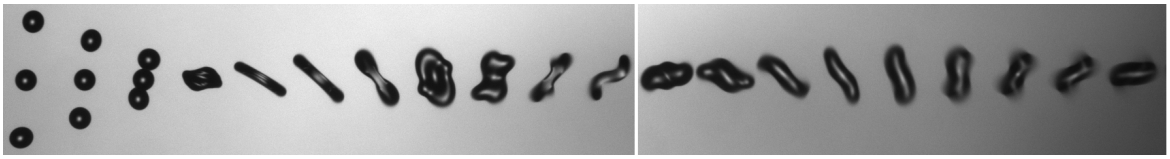

Figure 4.21: Coalescence at ternary collision, using glycerol 50% as the liquid, at $D = 390\,\mu\text{m},\ We = 81.5,\ X = 0.22,\ f = 5151\,\text{Hz}$.

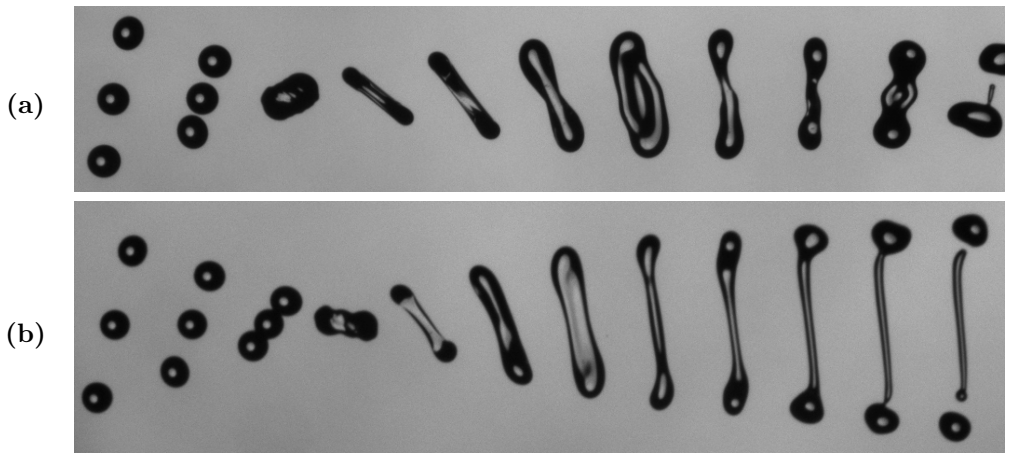

Figure 4.22: Stretching separation at ternary collisions, using glycerol 50% as the liquid, at **a** $D = 386\,\mu$m, $We = 81$, $X = 0.31$, $f = 5151\,$Hz **b** $D = 372\,\mu$m, $We = 83.6$, $X = 0.56$, $f = 5710\,$Hz.

As for binary collisions, an increase of the impact parameter stabilises the collision, and the three droplets merge permanently. This can be seen in figure 4.21. The merged droplet is highly deformed and oscillates over a long period of time, but surface tension forces prevent the breakup. This photograph looks a bit different from the others, because the LED was used in this case for the illumination of the droplets.

After increasing the non-dimensional impact parameter to 0.31, stretching separation occurs, which can be seen in figure 4.22 **a**. Due to the relatively small value of X, the droplets are strongly deflected from their initial trajectories. In figure 4.22 **b**, stretching separation at a further increased impact parameter is pictured. The formation of the connecting ligament and its pinching off from the outer droplets can be seen nicely. The breakup of the ligament into satellites takes place farther downstream.

Finally, the different regimes obtained for ternary drop collisions at high Weber numbers around 140 - 145 are presented. In figure 4.23, reflexive separation at a head-on collision is pictured. The droplets collide at a high relative velocity and are deformed into a

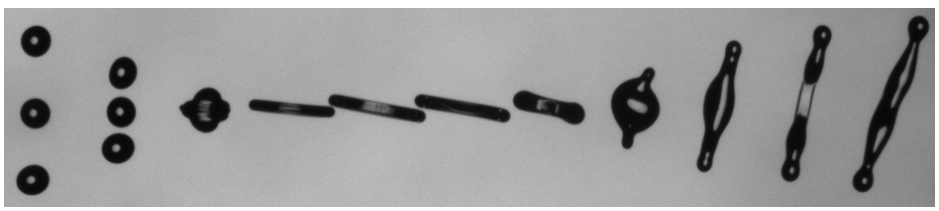

Figure 4.23: Reflexive separation at ternary collision, using glycerol 50% as the liquid, at a large Weber number: $D = 399\,\mu$m, $We = 143.1$, $X = 0.11$, $f = 5530\,$Hz.

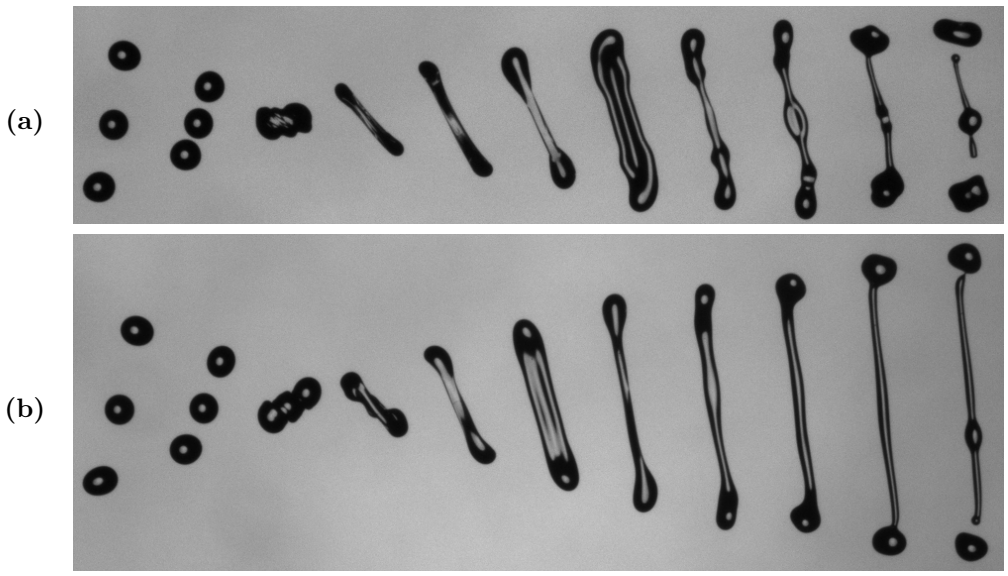

Figure 4.24: Stretching separation at ternary collisions, using glycerol 50% as the liquid, at large Weber numbers: **a** $D = 402\,\mu$m, $We = 143.4$, $X = 0.37$, $f = 5530\,$Hz **b** $D = 407\,\mu$m, $We = 141$, $X = 0.55$, $f = 5530\,$Hz.

narrow disk with a very large diameter, exceeding the initial droplet diameter many times. After relaxation of the disk, a cylindrical shaped droplet is formed. Then drops are pinched off from its ends. The breakup cannot be seen in the photograph, but the mechanism is basically the same as for binary collisions at high Weber numbers (see figure 4.8 **b**).

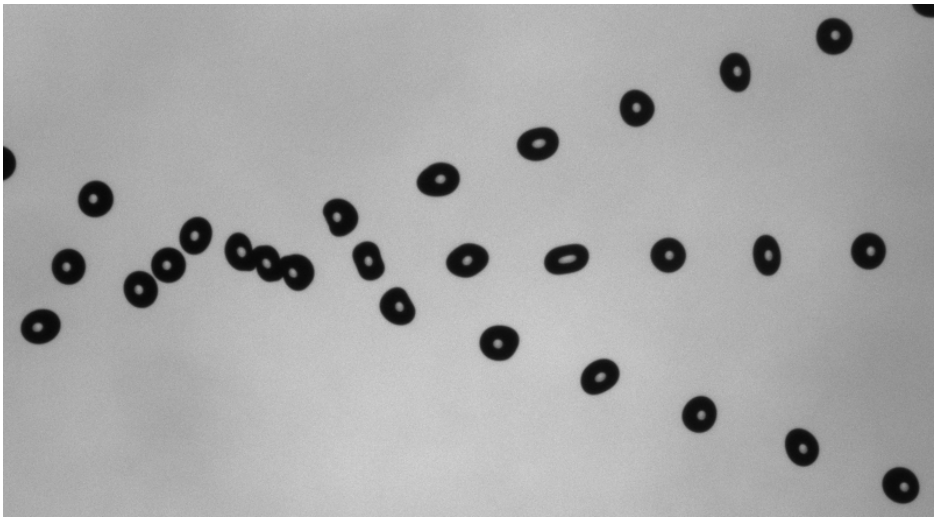

Figure 4.25: Bouncing at ternary collision, using glycerol 50% as the liquid, at a large Weber number: $D = 400\,\mu$m, $We = 140.3$, $X = 0.77$, $f = 5530\,$Hz.

As the impact parameter exceeds a critical value stretching separation occurs. This can be seen in figure 4.24 **a** at $X = 0.37$. Because of the relatively small impact parameter, the volume of the interacting portions is quite large. This leads to a broad ligament and, in further consequence, to highly deformed droplets, which can be seen in the last two stages of the collision. For a larger impact parameter, the volume of the interacting portions shrinks and the two outer droplets are not distracted as much from their initial trajectories as at smaller impact parameters. This is pictured in figure 4.24 **b** at $X = 0.55$.

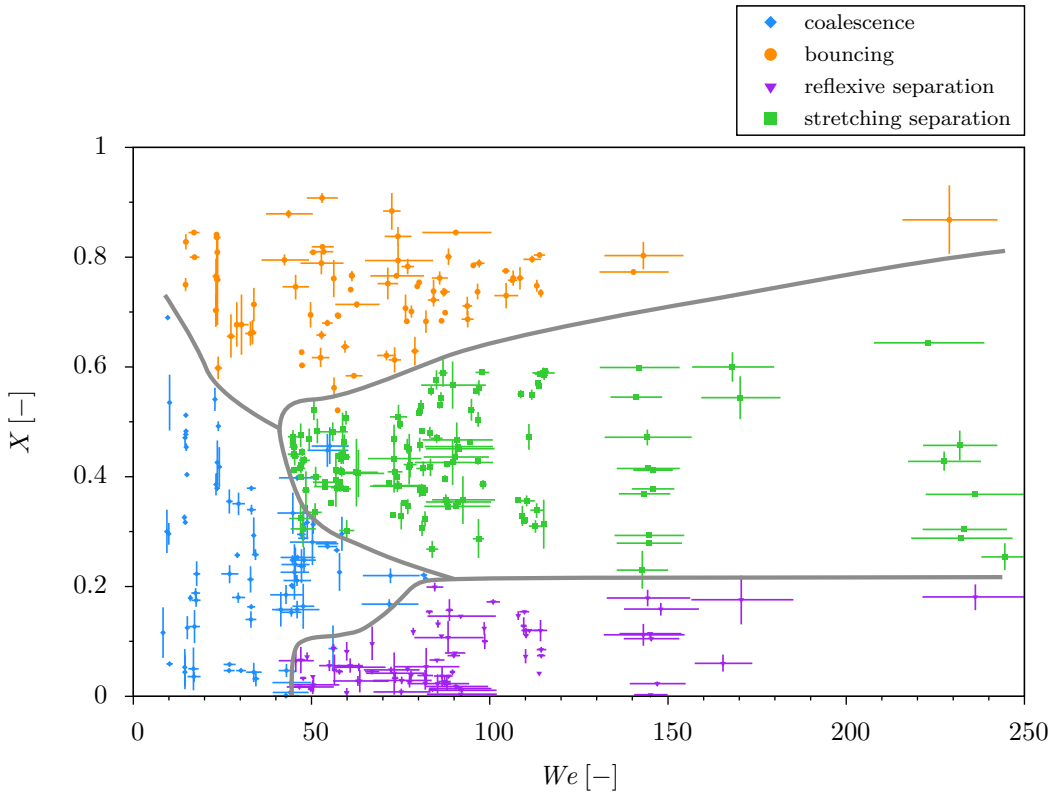

Figure 4.26: Collision regime map obtained for ternary drop collisions, using glycerol 50% as the liquid, in an atmospheric environment at $T \approx 23\,°\mathrm{C}$. The droplet diameter ranges between 340 μm and 419 μm, leading to an average Ohnesorge number of $Oh \approx 0.031$. The relative velocity is varied in the range of $1.1\,\mathrm{m\,s^{-1}} \leq U \leq 6\,\mathrm{m\,s^{-1}}$, which leads to Weber numbers from 8 to 245. The non-dimensional impact parameter X is plotted with an error bar between $|X_{LC}|$ and $|X_{RC}|$ and the Weber number is plotted with an error bar between We_{LC} and We_{RC}, which are calculated with the relative velocities $2U_{LC}$ and $2U_{RC}$, respectively. The transitions are sketched as grey lines.

The third possible collision outcome at high Weber numbers is bouncing. In figure 4.25 an example is given at a non-dimensional impact parameter of 0.77. The photograph perfectly shows that the central droplet is deformed at two opposing poles, whereas the outer droplets are only impressed at on pole. Thus, it takes a longer time for the central droplet to relax into a sphere again.

In figure 4.26, the (X, We) nomogram obtained for ternary liquid drop collisions is plotted. The average droplet diameter is 379 μm, which leads to an average Ohnesorge number of $Oh \approx 0.031$. As sketched in figure 3.7 **b**, there are basically two relative velocities and two non-dimensional impact parameters for collisions of three droplets. On the one hand, between the left and the central droplet and on the other hand, between the right and the central droplet. Due to symmetry, the absolute value of these two velocities and impact parameters should be equal (see table 3.4). However, perfectly symmetric drop collisions are practically not achieved. To take this into consideration each data point in 4.26 is plotted with an error bar in terms of We and X. The error bar for the Weber number is taken as the variability of the relative velocity U with extreme values of $2U_{LC}$ and $2U_{RC}$. The non-dimensional impact parameter X is drawn between $|X_{LC}|$ and $|X_{RC}|$. The (X, We) coordinates of the photographs

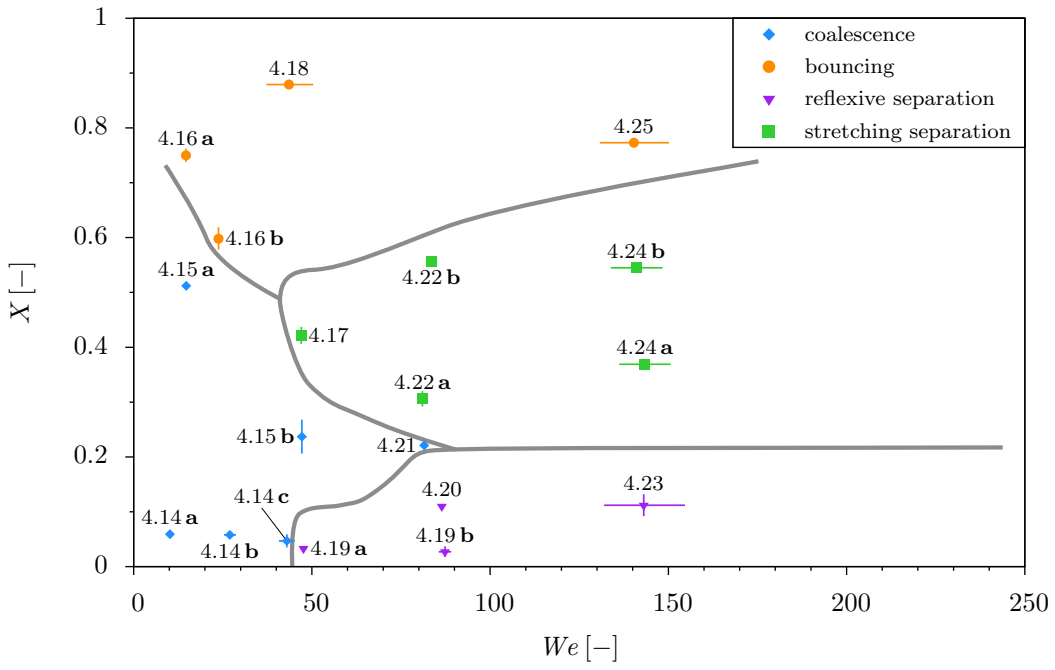

Figure 4.27: Coordinates of the presented photographs in the ternary collision regime map, which is given in figure 4.26.

presented above are marked in figure 4.27.

According to figure 4.26, and as already mentioned above, four different regimes can be identified. Starting with a small Weber number, say 10, only two collision outcomes are possible, namely coalescence and bouncing. The former occurs for head-on collisions at non-dimensional impact parameters up to around 0.7 and the latter happens when this critical value is exceeded. With increasing Weber number, the critical impact parameter representing the transition between these two regimes is decreased.

At $We \approx 45$, two other possible collision outcomes appear. For head-on collisions, reflexive separation occurs, monotonously shifting its transition against coalescence to larger impact parameters with increasing Weber numbers. At $We \approx 90$ and $X \approx 0.22$, the three regimes of coalescence, reflexive separation and stretching separation meet. For larger Weber numbers, three droplets cannot coalesce permanently. The transition between the regimes of reflexive and stretching separation proceeds at approximately constant non-dimensional impact parameter ($X \approx 0.22$) for Weber numbers up to 250, which is the limit of We in the present study.

As mentioned above, stretching separation occurs at $We \approx 45$, and a non-dimensional impact parameter of around 0.5. In this parameter range, the regimes of coalescence, bouncing and stretching separation meet. It has to be stated that an exact crossing point could not be determined, because the collision outcome is very sensitive to any disturbances and not easy to identify. Therefore, as for binary collisions, this area remains white in figure 4.26. For increasing Weber number, the transition between coalescence and stretching separation is shifted to smaller impact parameters until the regimes of reflexive separation and stretching separation meet. The critical non-dimensional impact parameter for the transition from stretching separation to bouncing increases with increasing Weber number.

Note, that the collision regime map in figure 4.26 agrees very well with the (X, U) nomogram obtained by Planchette (2011) at $D = 375\,\mu$m. Although the liquids are not exactly the same, glycerol 50% is used in the current study, while glycerol 40% was used by Planchette (2011) (see table 3.1), the outcomes of both studies match very well in a qualitative way.

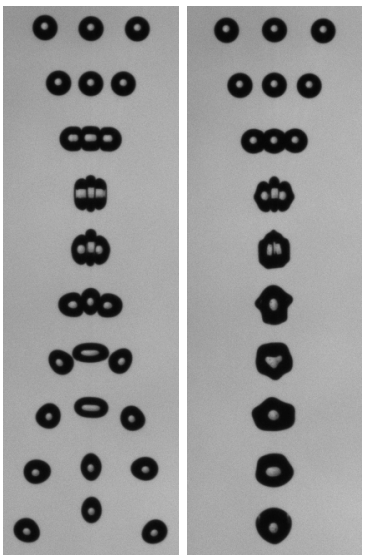

(a) **(b)**

Figure 4.28: Ternary head-on collisions using glycerol 30% as the liquid: **a** bouncing, **b** coalescence. The corresponding collision parameters to the two photographs are listed in table 4.1.

Bouncing at head-on collisions

During the measurements for the map of regimes for ternary collisions, bouncing at zero impact parameter was not observed. Moreover, looking at the transition between coalescence and bouncing in figure 4.26, it appears that the critical impact parameter increases with decreasing Weber number in the investigated domain which is different from what was observed with binary collisions in a comparable domain. However, bouncing at $X = 0$ was observed using glycerol 30% as the liquid. In comparison to glycerol 50% its dynamic viscosity is smaller but its surface tension is almost equal (see table 3.1).

In figure 4.28 **a**, bouncing at a ternary head-on collision is pictured. It can be seen that all three drops are highly squeezed due to the relatively large relative velocity, but no

Figure	Relative velocity [$\mathrm{m\,s^{-1}}$]			Impact parameter [$-$]			[μm]	[Hz]
	U	U_{LC}	U_{RC}	X	X_{LC}	X_{RC}	D	f
4.28 **a**	2.140	1.059	1.081	0.017	0.007	-0.026	353	5460
4.28 **b**	2.139	1.060	1.079	0.023	0.029	-0.018	354	5460

Table 4.1: Corresponding collision parameters to the two photographs in figure 4.28.

liquid bridge is formed. Thus, the droplets retract and bounce off each other. However, this process is not easy to achieve since small disturbances cause coalescence to occur. This can be seen in figure 4.28 **b**. The parameters for both photographs in figure 4.28 are basically identical (see table 4.1). It is interesting to note that the Weber number of ≈ 25.5 for the two collisions in figure 4.28 is relatively large. In order to give a reliable explanation for this behaviour, further experimental investigations would be necessary. Maybe it cannot be characterized by a set of non-dimensional numbers only, but additional geometric parameters like the angle between the trajectories of the droplets, characteristics of the ambient air and limitations of the alignment tuning may play an important role.

4.1.3 Comparison of binary and ternary drop collisions

In sections 4.1.1 and 4.1.2, the collision regimes of binary and ternary liquid drop collisions for $Oh \approx 0.032$ were presented and discussed. In this part of the thesis, the two cases are compared, underlining differences and similarities. First of all, the obvious and main difference is that a third droplet in the centre is added for ternary collisions. However, this central droplet does not contribute additional energy in terms of kinetic energy, which can be explained looking at figure 3.8. The velocity vector of the central droplet points downwards, whereas the relative velocities between both outer droplets and the central droplet point normal to its direction. Thus, the drop in the centre brings no additional kinetic energy into the collision, because the velocity component in the direction of the trajectory of the central droplet is the same for all three drops (see equations (3.17) and (3.18)). On the other hand, the surface energy of the central drop cannot be neglected.

At ternary collisions, four possible collision outcomes, similar to binary collisions, were observed. In figure 4.29, the obtained collision regime maps for binary (see figure 4.11) and ternary (see figure 4.26) drop collisions are compared. This is legitimate because both maps were achieved at approximately the same Ohnesorge number. For simplicity only the transitions between the particular regimes are sketched in figure 4.29. The transitions for binary drop collisions are drawn as full grey lines and the transitions for ternary collisions are sketched as black dashed lines. Moreover, the coordinates of some photographs, which will be discussed later, are marked.

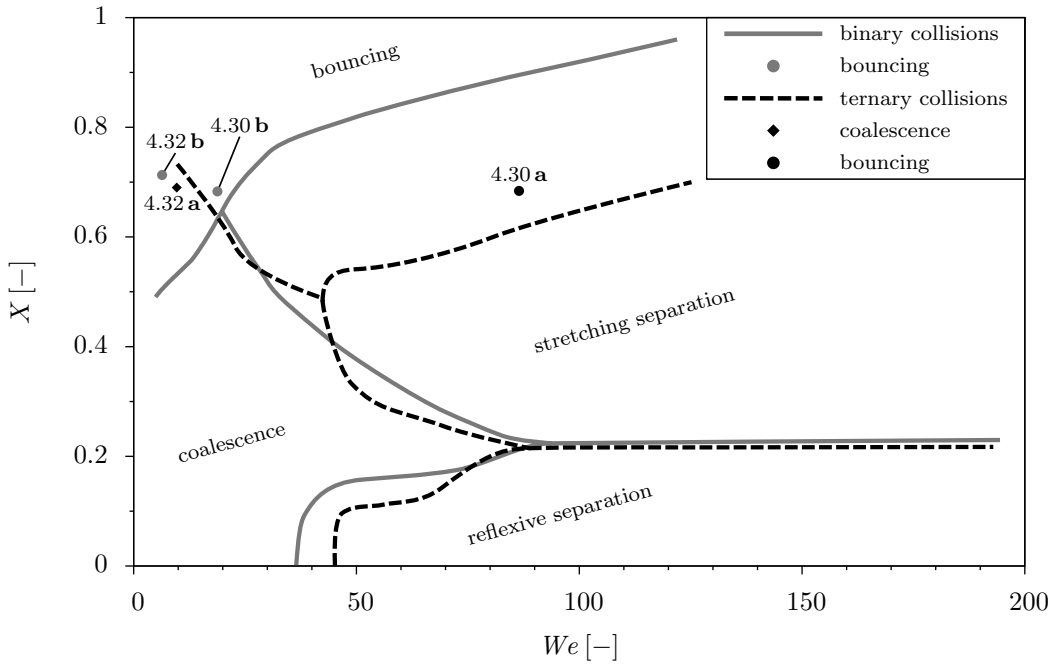

Figure 4.29: Transitions for binary and ternary liquid drop collisions according to figure 4.11 and figure 4.26, respectively.

As a first step, the four collision regimes of binary and ternary drop collisions are compared in a qualitative way with the help of the photographs presented in sections 4.1.1 and 4.1.2. In a second stage, the differences and similarities of the transition boundaries are discussed.

Regime of coalescence

Coalescence for binary and ternary head-on collisions is pictured in figures 4.1 and 4.14. The first phase of the collision, until the formed disk reaches its maximum extension, is different in both cases due to the additional mass of the central droplet for ternary collisions. However, the second phase, where the disk relaxes and oscillates looks quite similar for both cases. Especially in figure 4.14 **c**, the disk relaxes into a cylindrical rod, exactly as in the binary case given in figure 4.1 **c**. Evidently, assuming equal-sized initial droplets, the drop formed after a ternary collision has a diameter of around $1.44D$, whereas the drop resulting from the binary collision has only a diameter of $1.26D$. The similarities discussed above can also be found comparing pictures of coalescence at non-zero impact parameter (see figures 4.15 and 4.21 compared to figures 4.3 and 4.5).

Regime of bouncing

In order to compare the phenomenon of bouncing for binary and ternary drop collisions, the photographs of figures 4.7 and 4.25 are used. As the process of collision is only qualitatively compared, the parameters of both collisions can differ quantitatively. For the binary case, which can be seen in figure 4.7, both droplets are equally deformed at opposed sides. The same applies for both outer droplets in ternary collisions (see figure 4.25). However, this time both drops do not have direct contact, but impinge on the central droplet. Therefore, the central droplet is symmetrically deformed and undergoes a larger distortion than the two impacting droplets.

Regime of reflexive separation

Reflexive separation at head-on collision and intermediate Weber numbers can be seen in figure 4.2 **a** for the binary case and in figure 4.19 **a** for the ternary case. Analogous to the regime of coalescence, which was already discussed above, the relaxation of the disk into a cylindrical rod which leads to breakup looks similar for both types of collisions. This can be observed for head-on collisions at large Weber numbers (compare figure 4.8 **b** to figure 4.23) as well as for collisions at non-zero impact parameter (compare figure 4.9 **b** to figure 4.20).

Regime of stretching separation

Due to the central droplet at ternary collisions, there is more liquid available for the formation of a connecting ligament than for binary collisions. On the one hand, for binary collisions, the two main resulting droplets are smaller than the initial droplets because liquid is lost for the formation of the satellite droplets. On the other hand, for ternary collisions, the two main emerging droplets are larger than the initial droplets, because they take liquid from the additional central droplet. For example, this can be seen by comparing figure 4.10 to figure 4.22. However, the principal mechanism of formation of the ligament and its breakup are the same for binary and ternary collisions.

In conclusion, the first phase of the collision, where the droplets collide, is different for binary and ternary drop collisions. However, the second phase, where the merged

complex relaxes or a ligament is formed, followed by possible breakup or permanent coalescence, seems to be identical in both cases. In the following part of the thesis, the transitions between different regimes in the collision regime maps of binary and ternary drop collisions are discussed.

Transition: coalescence - reflexive separation

For head-on collisions, the onset of fragmentation takes place at larger Weber numbers for ternary than for binary collisions. This can be seen clearly in figure 4.29. The reason for it is the central droplet at ternary collisions. This drop acts like a buffer by decreasing the occurring velocity gradient after the impact. Therefore, additional kinetic energy is required compared to binary drop collisions. At increasing impact parameter, the ternary transition follows the binary one until they meet at the maximum Weber number for coalescence to occur at $We \approx 90$ and $X \approx 0.2$. However, this value is rather vague, looking at the collision regime maps in figures 4.11 and 4.26. Thus, it cannot be trustworthily said if coalescence appears at higher Weber numbers for binary or ternary collisions. The higher required kinetic energy at ternary head-on collisions would also indicate that more energy is needed for reflexive separation to occur at small impact parameters. During the measurements for the collision regime maps, the highest Weber number where coalescence was observed is $We = 72.7$ for the binary case and $We = 82$ for the ternary case.

Transition: coalescence - stretching separation

The transition between coalescence and stretching separation occurs in the range of $0.2 < X < 0.6$ and $0.2 < X < 0.5$ for binary and ternary collisions, respectively. In the area, where the borders overlap in terms of the non-dimensional impact parameter, they seem to agree also very well in terms of the Weber number. The influence of the central droplet in ternary collisions appears to be decreased with increasing impact parameter. Therefore, no significant difference could be observed comparing the transition between coalescence and stretching separation. For ternary collisions in the range of $0.5 < X < 0.6$ the regimes of coalescence and bouncing meet. This is discussed in the paragraph on the transition between coalescence and bouncing.

Transition: reflexive separation - stretching separation

The transition between reflexive and stretching separation originates in the point where the regimes of coalescence, reflexive separation and stretching separation meet at $We \approx 90$ and $X \approx 0.2$. Similar to the transition between coalescence and reflexive separation, the value of this Weber number is not exactly determined. However, above a certain Weber number, the transition between reflexive separation and stretching separation comes into existence and remains at a constant value of $X \approx 0.2$ for increasing Weber number, which leads to a horizontal line in the (We, X) nomogram (see figure 4.29). This is valid for binary and ternary collisions similarly.

Transition: stretching separation - bouncing

Looking at figure 4.29, huge differences between binary and ternary collisions can be observed for the transition between stretching separation and bouncing. At a given Weber number, bouncing occurs for ternary collisions at much smaller non-dimensional impact parameters than for the binary case. However, if we take a closer look, the

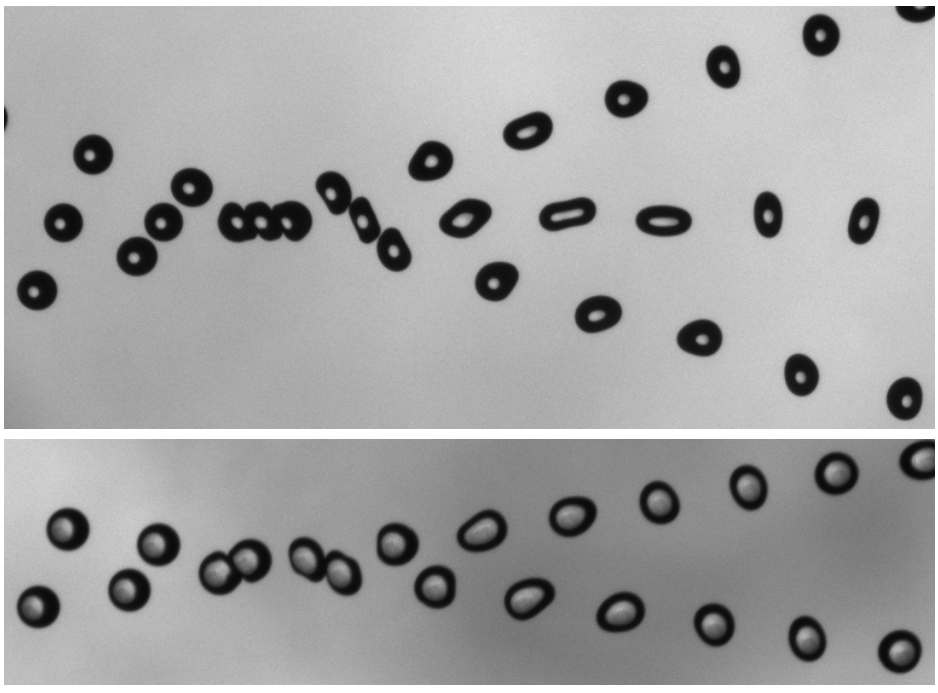

Figure 4.30: **a** Bouncing at ternary drop collision at $D = 376\,\mu\text{m}$, $U = 3.68\,\text{m}\,\text{s}^{-1}$, $X = 0.68$, $f = 5710\,\text{Hz}$ **b** Bouncing at binary drop collision at $D = 337\,\mu\text{m}$, $U = 1.81\,\text{m}\,\text{s}^{-1}$, $X = 0.68$, $f = 7060\,\text{Hz}$.

differences almost completely vanish and can be explained easily. Exemplarily, in figure 4.30 **a**, bouncing at a ternary collision is pictured at a quite large Weber number of 86.5. The collision is marked in the collision regime map in figure 4.29. It can be seen that, at these parameters, stretching separation would occur in the binary case. Now we take a look at the collision outcome if one of the two outer droplets at the ternary collision is removed. In this case, the remaining outer droplet and the central droplet collide at a velocity of $U/2$, which would be around $1.84\,\mathrm{m\,s^{-1}}$ in the case of figure 4.30 **a**. The binary collision outcome at this velocity can be seen in figure 4.30 **b** where two droplets collide at $U = 1.82\,\mathrm{m\,s^{-1}}$. The impact parameter is equal in both cases. The collision outcome of figure 4.30 **b**, is also marked in figure 4.29. It is located in the regime of bouncing for the binary case. Applying this procedure to all bouncing data points representing ternary collisions in figure 4.26, leads to figure 4.31. The old transition for ternary collisions between bouncing and reflexive separation is removed (compare to figure 4.29) and replaced by a new transition, which is drawn as a continuous black line. It can be seen that the transitions for binary and ternary drop collisions between

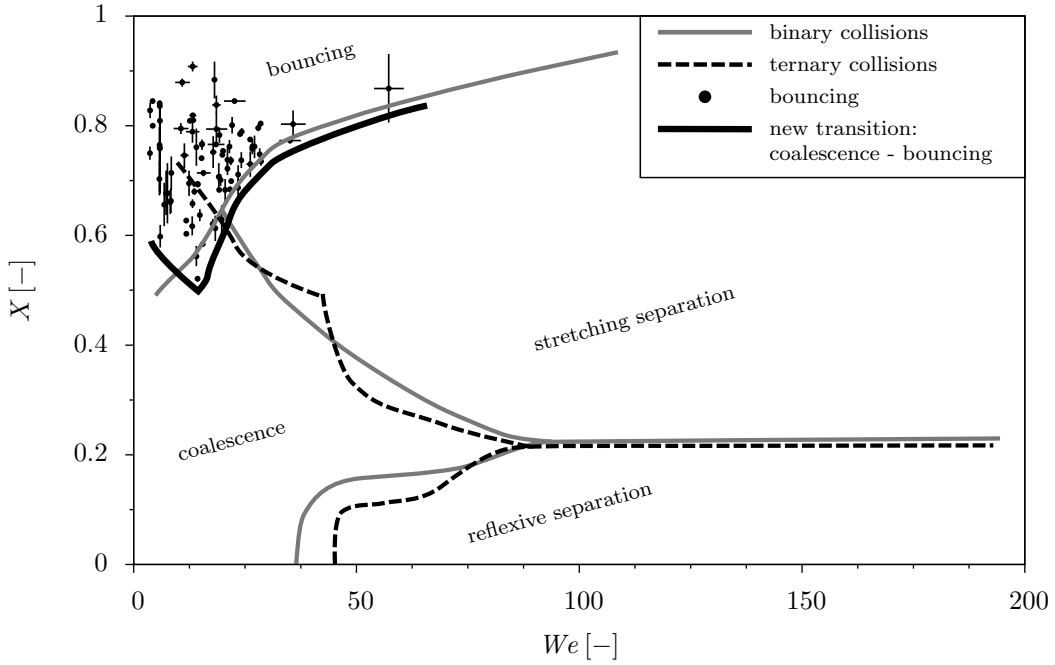

Figure 4.31: Transitions for binary and ternary liquid drop collisions according to figure 4.11 and figure 4.26, respectively. The non-dimensional impact parameter X is plotted with an error bar between $|X_{LC}|$ and $|X_{RC}|$. The Weber number is calculated with the half impact velocity $U/2$ and plotted with an error bar between We_{LC} and We_{RC}, which are calculated with the relative velocities U_{LC} and U_{RC}, respectively.

bouncing and reflexive separation now agree very well to a great extent. It can be concluded that, for the observed collisions, the mechanism of bouncing seems to be the same for binary and ternary drop collisions. The ternary case can be considered as two binary collisions at once. Therefore it is legitimate to use $U/2$, which corresponds to the relative velocity in the binary case, for the calculation of the Weber number in the ternary case. This is valid for bouncing droplets at Weber numbers in the range where stretching separation and bouncing meet. For decreasing Weber numbers at $We \approx 40$ and $X \approx 0.5$ this transition vanishes. Instead, the transition between coalescence and bouncing arises, which will be discussed next.

Transition: coalescence - bouncing

The transition between coalescence and bouncing differs strongly between binary and ternary collisions. Starting at a certain Weber number, say 10, the critical impact parameter increases with the Weber number for binary collisions, whereas the opposite happens for ternary collisions. In figure 4.32 **b**, a binary collision at $U = 1.02\,\mathrm{m\,s^{-1}}$ can be seen, where both droplets bounce apart again after the impact. Figure 4.32 **a** shows a ternary collision in the same range of Weber number and impact parameter. The positions of both collisions are marked in figure 4.29. Contrary to the binary case, the ternary collision results in coalescence. Both outer droplets impinge the central droplet at $U/2 = 0.62\,\mathrm{m\,s^{-1}}$ and after a short phase where the droplets are slightly deformed, the intervening air layer is expelled and a liquid bridge is formed. Afterwards, the merged droplet contracts due to surface tension forces. The excess energy is dissipated through oscillations and a single coalesced drop remains. Unfortunately, it was not possible to

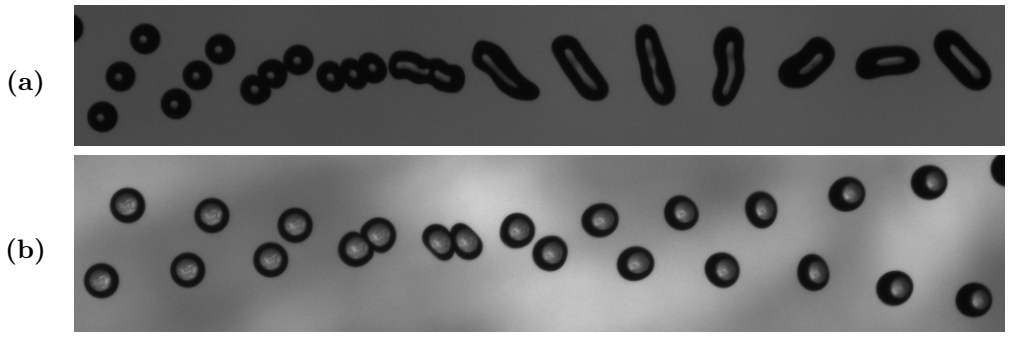

Figure 4.32: **a** Coalescence at ternary drop collision at $D = 375\,\mu\mathrm{m}$, $U = 1.23\,\mathrm{m\,s^{-1}}$, $X = 0.69$, $f = 4131\,\mathrm{Hz}$ **b** Bouncing at binary drop collision at $D = 360\,\mu\mathrm{m}$, $U = 1.02\,\mathrm{m\,s^{-1}}$, $X = 0.71$, $f = 4960\,\mathrm{Hz}$.

perform measurements for binary collisions at a relative velocity of $0.62\,\mathrm{m\,s^{-1}}$, which would help to explain the difference at transition between coalescence and bouncing at binary and ternary collisions. It is interesting to note that the trend of transition for the ternary case indicates that bouncing is impossible to occur at ternary head-on collisions. However, this phenomenon was already shown in section 4.1.2, but with a less viscous liquid.

4.2 Onset of fragmentation

In this section, the results of the investigation on the onset velocity, defining the transition between coalescence and reflexive separation for the case of head-on collisions, are presented and discussed. From now on, for simplicity, reflexive separation is merely called separation. First of all, the obtained data for binary head-on collisions with droplets of the same size is presented. Afterwards, the results for binary head-on collisions of unequal-sized droplets are discussed. Finally, the onset velocities for ternary drop collisions are presented.

4.2.1 Binary collisions of equal-sized droplets

In order to determine the onset of fragmentation for binary head-on collisions for a given liquid and a given droplet size, two different quantities have to be estimated. These are the largest velocity $U_{0,c}$ where coalescence can be observed and the smallest

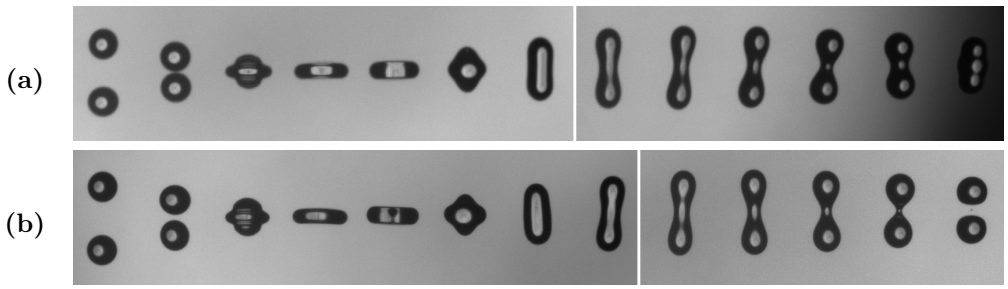

Figure 4.33: Onset of fragmentation for binary head-on collisions of equal-sized droplets using glycerol 40% as the liquid: **a** coalescence at $D = 361\,\mu\mathrm{m}$, $U_{0,c} = 2.13\,\mathrm{m\,s^{-1}}$, $X_{0,c} = 0.02$, $f = 6396\,\mathrm{Hz}$ **b** separation at $D = 365\,\mu\mathrm{m}$, $U_{0,s} = 2.18\,\mathrm{m\,s^{-1}}$, $X_{0,s} = 0.00$, $f = 6396\,\mathrm{Hz}$.

Liquid	μ [mPa s]	σ [mN m^{-1}]	D_{or} [μm]	U_0 [m s^{-1}]	$U_{0,c}$ [m s^{-1}]	$U_{0,s}$ [m s^{-1}]	$X_{0,c}$ [–]	$X_{0,s}$ [–]	D [μm]
Gl 10%	1.23	68.94	200	**1.96**	1.90	2.02	0.03	0.00	**336**
Gl 30%	2.17	67.45	200	**2.00**	1.99	2.00	0.00	0.02	**370**
			100	**2.82**	2.78	2.85	0.01	0.04	**220**
			70	**3.67**	3.59	3.74	0.02	0.01	**141**
Gl 40%	3.15	66.79	200	**2.16**	2.13	2.18	0.02	0.00	**363**
			70	**4.29**	4.24	4.34	0.03	0.00	**132**
Gl 50%	5.24	66.53	500	**1.58**	1.41	1.75	0.00	0.01	**864**
			300	**1.98**	1.92	2.04	0.03	0.07	**503**
			200	**2.53**	2.50	2.55	0.01	0.01	**338**
			100	**3.45**	3.38	3.52	0.03	0.00	**221**
			70	**4.61**	4.53	4.68	0.03	0.00	**149**
Gl 60%	8.81	65.27	200	**2.85**	2.80	2.89	0.00	0.00	**367**
Gl 65%	12.11	64.39	200	**3.73**	3.67	3.79	0.01	0.02	**366**
Gl 70%	17.84	64.00	200	**4.44**	4.33	4.54	0.02	0.02	**369**
SO M3	2.79	19.50	200	**1.46**	1.43	1.48	0.01	0.02	**347**
SO M10	9.37	20.10	200	**2.98**	2.79	3.17	0.00	0.04	**365**

Table 4.2: Results describing the onset of fragmentation for binary head-on collisions of equal-sized droplets.

velocity $U_{0,s}$, where separation can be detected. Certainly, $U_{0,c}$ has to be smaller than $U_{0,s}$. The onset velocity can then be calculated by

$$U_0 = \frac{1}{2}(U_{0,c} + U_{0,s})\,. \tag{4.1}$$

In figure 4.33, two photographs determining the onset of fragmentation for binary collisions, using glycerol 40% as the liquid, at an average droplet diameter of $D \approx 363\,\mu$m can be seen. The picture on top, in figure 4.33 **a**, shows the regime of coalescence at a relative velocity of $U_{0,c} = 2.13\,\mathrm{m\,s^{-1}}$. In figure 4.33 **b**, separation at $U_{0,s} = 2.18\,\mathrm{m\,s^{-1}}$ can be observed. Consequently, according to equation (4.1), the onset velocity results in $U_0 = 2.16\,\mathrm{m\,s^{-1}}$.

A list of the results, obtained from the experiments defined in table 3.2, is given in table 4.2. The quantities U_0 and D are written in bold. With the help of these quantities and the fluid properties (see table 3.1), non-dimensional quantities like Weber, Reynolds

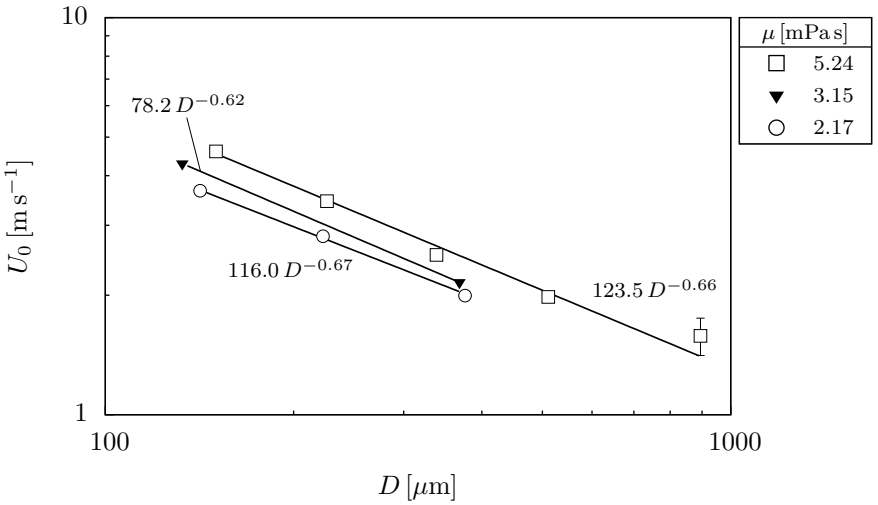

Figure 4.34: Evolution of the obtained onset velocity with the droplet diameter for binary collisions of equal-sized droplets.

and Ohnesorge number can be calculated in order to describe the onset of fragmentation systematically.

In figure 4.34, the evolution of the threshold velocity is plotted against the average droplet diameter for three different liquids. It can be observed that, for a given liquid, the critical threshold velocity reduces monotonously with increasing droplet size. A power law between U_0 and D appears, with an exponent in the range of -0.6 to -0.7.

Another information which can be obtained from figure 4.34 is that, for a given droplet diameter, the onset velocity is decreased with the dynamic viscosity. Therefore, in figure 4.35, the evolution of the threshold velocity is plotted against the dynamic viscosity. Results obtained with equal nozzle diameters D_{or} , and therefore droplets with around the same diameter, are marked with the same symbol in this graph. Except for the silicon oils (SO), which are marked with open circles, because their surface tension differs from the almost equal surface tensions of the aqueous glycerol solutions. Some results are plotted with an error bar for the onset velocity between the values of $U_{0,c}$ and $U_{0,s}$, which are listed in table 4.2. It can be seen that, for a given droplet diameter, the onset velocity grows monotonously with the dynamic viscosity. This seems reasonable, because with increasing μ the resistance of the liquid against deformation rises and therefore more energy is needed to break up the merged droplet. For viscosities smaller than approximately 10 mPa s, a power law between U_0 and μ is obtained for various droplet sizes. The exponent is in the range of 0.2 to 0.25.

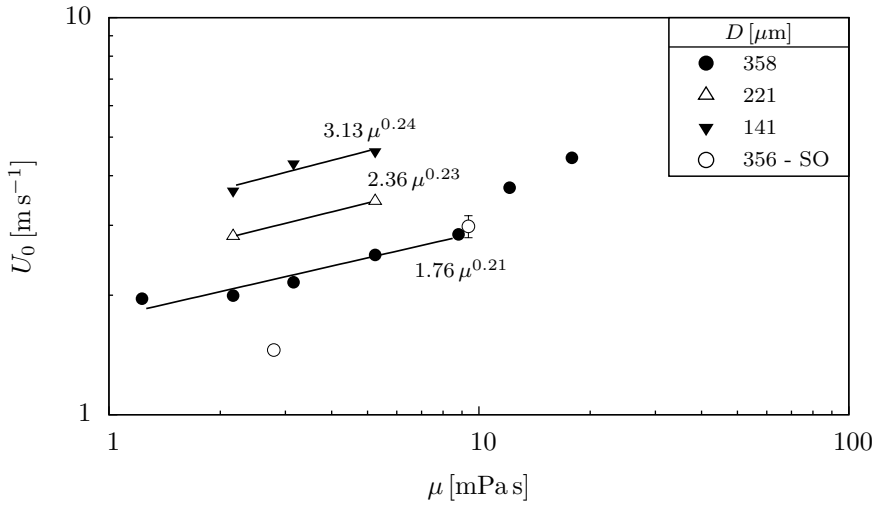

Figure 4.35: Evolution of the measured onset velocity with the dynamic viscosity for binary collisions of equal-sized droplets.

However, regarding the results with $D = 358\,\mu$m, this power law cannot be applied to the data for $\mu > 10\,$mPa s, because the growth of U_0 with the dynamic viscosity is increased. In figure 4.35, small deviations of some data points from the fitted lines can observed. This can be explained by the fact that, for a given nozzle diameter, the droplet diameters are not constant at all measurements. For example, for an average droplet diameter of $358\,\mu$m, the measured droplet diameters vary from 336 to $370\,\mu$m (see table 4.2).

In order to bring all these results to a single line, we plot the onset Weber number as a function of the Ohnesorge number. This can be seen in figure 4.36 for the results of this study. Qian & Law (1997) proposed a criterion to describe the transition between coalescence and separation, where the onset Weber number grows linearly with the Ohnesorge number (see equation (2.46)). This is the case at $Oh < 0.06$ for the obtained results. For this regime the data is fitted with a line (see figure 4.36), which is defined by the equation $We_0 = 730.0\,Oh + 14.4$. This agrees very well with the measurements of Qian & Law (1997), who obtained $We_0 \approx 678.8\,Oh + 15$ at $Oh < 0.05$. However, as shown in figure 4.36, for Ohnesorge numbers larger than around 0.06 (regime 2), the linear correlation between We_0 and Oh is not valid any more. This indicates that the mechanism of separation, and accordingly the process of the collision itself, is different for droplets with Ohnesorge numbers smaller and larger than 0.06.

The linear correlation between onset Weber number and Ohnesorge number implies

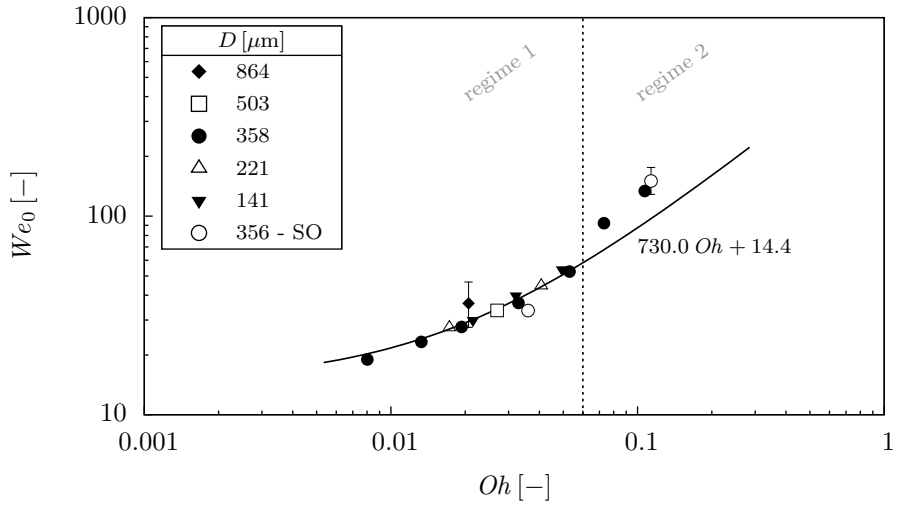

Figure 4.36: Evolution of the onset Weber number with the Ohnesorge number for binary collisions of equal-sized droplets. The curve is fitted with the data at $Oh < 0.06$. The used liquids are listed in table 3.2.

that the onset velocity is proportional to $U_0 \sim \mu^{0.5} D^{-0.75}$. The experimental results show that $U_0 \sim \mu^{0.21} D^{-0.66}$ (see figures 4.34 and 4.35). While the agreement for the exponents of the droplet diameter is quite good, the exponents of the dynamic viscosity differ tremendously. Thus, the linear correlation between We and Oh appears to be appropriate to represent the onset of fragmentation for binary head-on collisions of the same liquid (see figure 4.36), but comparing it to experimental results shows that it takes certain parameters incorrectly into account. This can be improved by representing the transition between coalescence and separation by a power law between Reynolds number and Ohnesorge number, which is introduced and discussed in section 4.2.3.

4.2.2 Binary collisions of unequal-sized droplets

In this section the results for the onset of fragmentation at binary head-on collisions of unequal-sized droplets are presented. Basically, experiments for two different droplet size ratios of $\delta = 0.62$ and $\delta = 0.76$ have been performed, using three different liquids (see table 3.3). The obtained results are listed in table 4.3, where U_0 is calculated according to equation (4.1).

In figure 4.37, coalescence and separation at binary collisions of unequal-sized droplets

Liquid	D_{or} [μm]	U_0 [m s^{-1}]	$U_{0,c}$ [m s^{-1}]	$U_{0,s}$ [m s^{-1}]	$X_{0,c}$ [−]	$X_{0,s}$ [−]	D [μm]	δ [−]
Gl 30% ($\mu = 2.17$ mPa s) ($\sigma = 67.45$ mN m^{-1})	200 100	**2.95**	2.92	2.97	0.05	0.00	**354** **223**	0.63
	100 70	**3.65**	3.62	3.68	0.02	0.01	**174** **135**	0.78
Gl 40% ($\mu = 3.15$ mPa s) ($\sigma = 66.79$ mN m^{-1})	200 100	**3.19**	3.06	3.31	0.00	0.03	**362** **228**	0.63
	100 70	**3.84**	3.75	3.93	0.11	0.02	**186** **142**	0.76
Gl 50% ($\mu = 5.24$ mPa s) ($\sigma = 66.53$ mN m^{-1})	200 100	**3.91**	3.86	3.95	0.07	0.01	**357** **216**	0.61
	100 70	**4.76**	4.74	4.77	0.01	0.02	**181** **137**	0.76

Table 4.3: Onset velocities for binary head-on collisions of unequal-sized droplets.

are pictured. The left droplet stream is produced with a smaller nozzle diameter than the right droplet stream, which leads to a droplet size ratio of $\delta = 0.76$. Both drop generators are driven with the same excitation frequency f, leading to a different spacing between two successive droplets for both droplet streams. In order to ensure that the relative velocity between two colliding droplets consists only of a component in the horizontal direction, the right droplet stream is inclined, leading to an equal vertical distance between two successive droplets for the left and the right droplet stream.

A difficulty arising at binary collisions of unequal-sized droplets is the proper definition of a representative droplet diameter D for calculating non-dimensional quantities like Weber and Ohnesorge number. In fact, there are four possibilities which are listed below.

- small droplet diameter $D = D_1$
- large droplet diameter $D = D_2$
- average droplet diameter $D = (D_1 + D_2)/2$
- mass conserving average droplet diameter $D = \sqrt[3]{(D_1^3 + D_2^3)\,/\,2}$

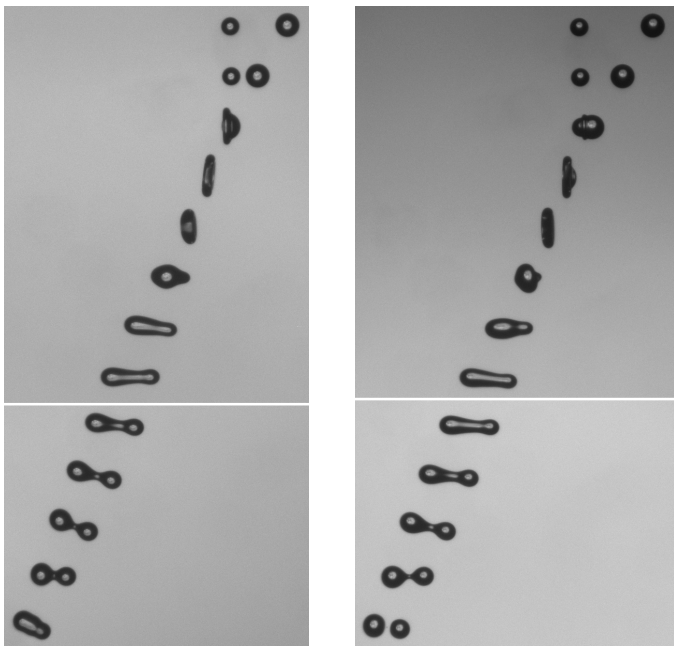

(a) **(b)**

Figure 4.37: Onset of fragmentation for binary head-on collisions of unequal-sized droplets using glycerol 50% as the liquid: **a** coalescence at $D_1 = 137\,\mu\text{m}$, $D_2 = 181\,\mu\text{m}$, $\delta = 0.76$, $U_{0,c} = 4.74\,\text{m}\,\text{s}^{-1}$, $X_{0,c} = 0.01$, $f = 20035\,\text{Hz}$ **b** separation at $D_1 = 137\,\mu\text{m}$, $D_2 = 181\,\mu\text{m}$, $\delta = 0.76$, $U_{0,s} = 4.77\,\text{m}\,\text{s}^{-1}$, $X_{0,s} = 0.02$, $f = 20035\,\text{Hz}$.

In order to choose a reasonable droplet diameter, the onset velocity U_0 is plotted as a function of the droplet diameter. This can be seen in figure 4.38, where the droplet diameters are drawn with an error bar between the small and the large droplet diameter. Moreover, three lines are plotted, which are the fit curves of figure 4.34 for the collisions of two droplets of the same size. The error bars in figure 4.38 show that, for a given viscosity, the best agreement to binary collisions of equal-sized droplets is achieved using a droplet diameter between the smaller droplet diameter D_1 and the average droplet diameter $(D_1 + D_2)/2$. During the first period of the collision after the impact, high velocity gradients appear. Therefore it is assumed that the viscous dissipation in this phase is dominated by small scales. The Reynolds number is calculated with the small droplet diameter D_1 resulting in

$$Re = \frac{\rho U D_1}{\mu}\,. \tag{4.2}$$

With respect to the second period of the collision, where the merged disk relaxes into a sphere and inertia is irrelevant, the mass conserving average droplet diameter is used

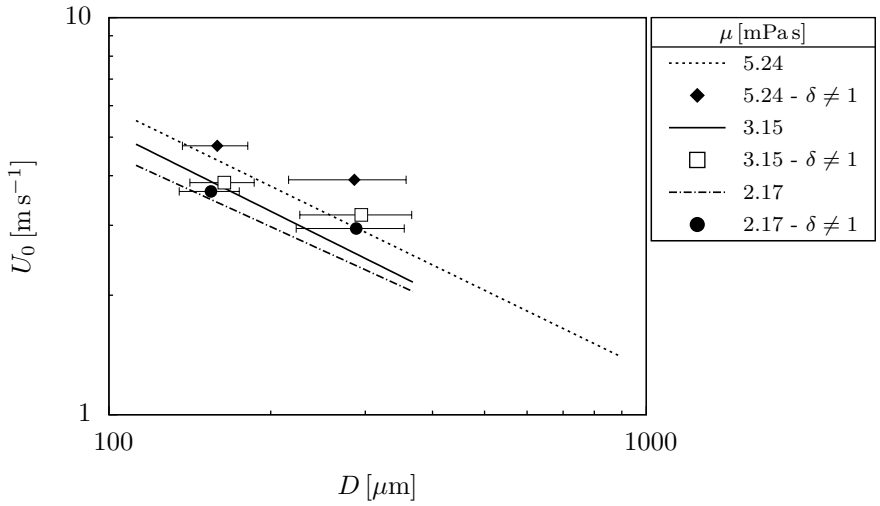

Figure 4.38: Correlation of the onset velocity with the droplet diameter for binary collisions of unequal-sized droplets. The lines correspond to the fit curves given in figure 4.34.

to calculate the Ohnesorge number:

$$Oh = \frac{\mu}{\rho\,\sigma\,\sqrt[3]{(D_1^3 + D_2^3)\,/\,2}}\,. \tag{4.3}$$

For the calculation of the Weber number, two different approaches are proposed. On the one hand, analogous to the Reynolds number, the smaller droplet diameter is used:

$$We = \frac{\rho\,U^2 D_1}{\sigma}. \tag{4.4}$$

On the other hand, since the impact inertia is related to the viscous dissipation during the first phase of the collision, the smaller droplet diameter is used for the estimation of the inertial energy. The surface energy is calculated with the mass conserving average droplet diameter. Thus, the Weber number is given by

$$We = \frac{\rho\,U^2 D_1^3}{\sigma\,\left[(D_1^3 + D_2^3)\,/\,2\right]^{2/3}}. \tag{4.5}$$

Analogous to figure 4.36, the evolution of the onset Weber number is plotted against the Ohnesorge number in figure 4.39. The solid line represents the trend curve obtained for binary collisions of equal-sized droplets given in figure 4.36. The onset Weber numbers obtained by equation (4.4) are black coloured. It can be seen that, for the larger droplet size ratio of $\delta = 0.76$, the data correlates very well with the results for binary collisions

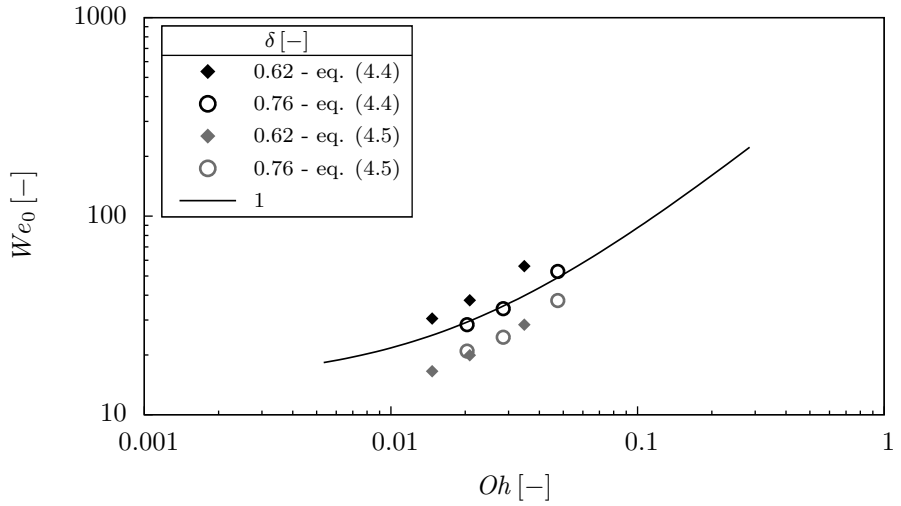

Figure 4.39: Evolution of the onset Weber number with the Ohnesorge number for binary head-on collisions of unequal-sized droplets. The used liquids are listed in table 3.3. The black line corresponds to the fit curve given in figure 4.36. For the black data points the Weber number is calculated as given in equation (4.4) and for the grey data points it is calculated by equation (4.5). The Ohnesorge number is obtained analogous to equation (4.3).

of equal-sized droplets. However, the Weber numbers for $\delta = 0.62$ are overestimated. Calculating the Weber number as given by equation (4.5) appears to unify the grey coloured data points. Then, however, the Weber numbers are underestimated compared to the results obtained for binary collisions of equal-sized droplets.

There are two possible explanations for this discrepancy. First of all, the wrong diameters were chosen for the calculation of We and Oh. However, it will be shown in section 4.2.3 that the Ohnesorge number correlates very well with the onset Reynolds number, indicating that the diameter in equation (4.3) is estimated correctly. Secondly, as already observed previously, Weber number and Ohnesorge number are not the right parameters to describe binary droplet collisions universally.

4.2.3 Ternary drop collisions

The onset velocity for ternary head-on collisions is determined similar to the binary case by defining a maximum velocity for coalescence and a minimum velocity for separation to occur. Thus, U_0 can be calculated as given in equation (4.1). In figure 4.40, on the

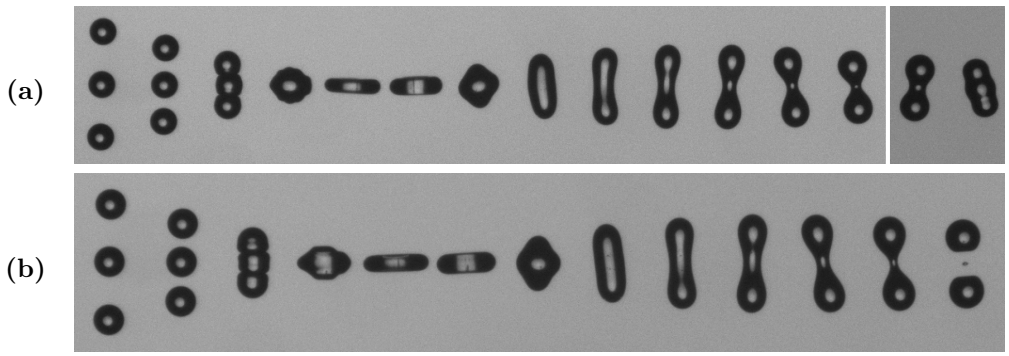

Figure 4.40: Onset of fragmentation for ternary head-on collisions using glycerol 30% as the liquid: **a** coalescence at $D = 186\,\mu$m, $U_{0,c} = 3.34\,\mathrm{m\,s^{-1}}$, $X_{0,c} = 0.02$, $f = 14940\,$Hz **b** separation at $D = 186\,\mu$m, $U_{0,s} = 3.49\,\mathrm{m\,s^{-1}}$, $X_{0,s} = 0.03$, $f = 14940\,$Hz.

top coalescence is pictured at $U_{0,c} = 3.34\,\mathrm{m\,s^{-1}}$ and on the bottom separation can be observed at $U_{0,s} = 3.49\,\mathrm{m\,s^{-1}}$, leading to an onset velocity of $U_0 = 3.41\,\mathrm{m\,s^{-1}}$. The used liquid is glycerol 30% and the average droplet diameter is $D = 186\,\mu$m. All of the obtained results for ternary head-on collisions are listed in table 4.4. The relevant quantities are written in bold.

Below, the characteristics of the onset of fragmentation are examined more closely. In figure 4.41, the onset velocity is plotted against the dynamic viscosity of the liquid at several almost constant droplet diameters. For a droplet diameter of $186\,\mu$m, a power law between U_0 and μ with an exponent of 0.17 appears and for $D = 361\,\mu$m a

Liquid	μ [mPa s]	σ [mN m^{-1}]	D_{or} [μm]	U_0 [m s^{-1}]	$U_{0,c}$ [m s^{-1}]	$U_{0,s}$ [m s^{-1}]	$X_{0,c}$ [–]	$X_{0,s}$ [–]	D [μm]
Gl 10%	1.23	68.94	200	**2.66**	2.54	2.77	0.01	0.01	**368**
Gl 30%	2.17	67.45	200	**2.83**	2.74	2.91	0.00	0.01	**354**
			100	**3.41**	3.34	3.49	0.02	0.03	**186**
Gl 40%	3.15	66.79	200	**2.79**	2.70	2.88	0.03	0.02	**361**
			100	**3.66**	3.55	3.78	0.03	0.03	**181**
Gl 50%	66.53	5.24	300	**2.38**	2.33	2.43	0.02	0.00	**536**
			200	**2.78**	2.74	2.83	0.02	0.01	**360**
			100	**3.98**	3.92	4.04	0.00	0.04	**192**
			70	**4.80**	4.69	4.91	0.02	0.02	**143**

Table 4.4: Onset velocities for separation and corresponding parameters obtained for ternary head-on collisions.

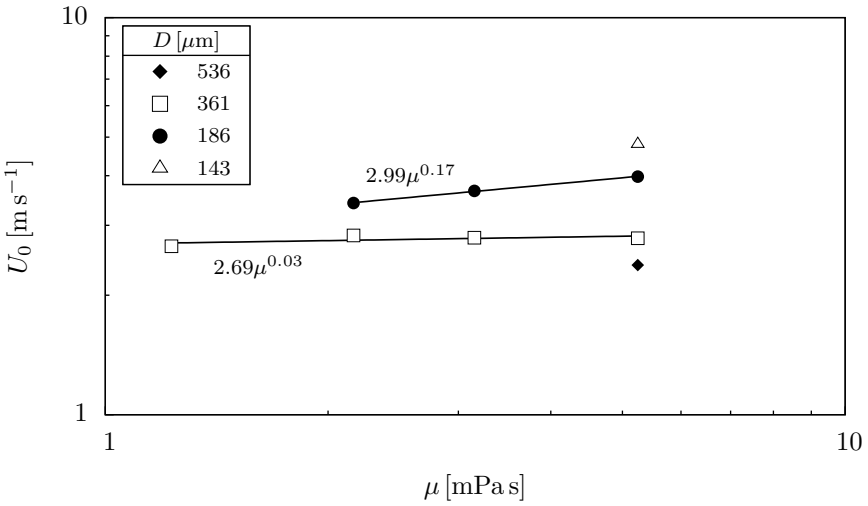

Figure 4.41: Correlation of the onset velocity with the dynamic viscosity for ternary drop collisions.

power law between these two quantities with an exponent of almost zero is obtained. Hence, the onset velocity for ternary collisions seems to be nearly independent from the dynamic viscosity. This is in contrast to the binary case, which was already discussed in figure 4.35. On the other hand, the mainstream trend that, at a given viscosity, the onset velocity decreases with increasing droplet diameter can be observed for both the binary and the ternary cases.

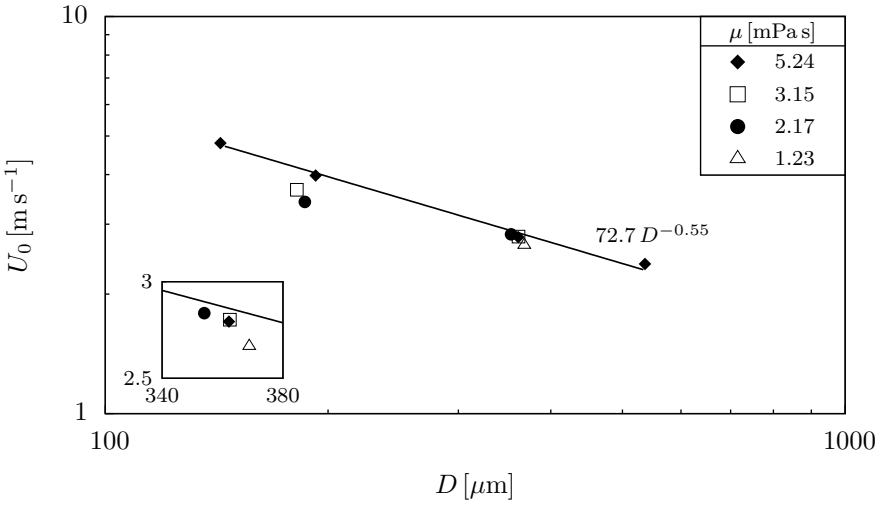

Figure 4.42: Onset velocity plotted against the droplet diameter for ternary drop collisions.

As a next step, in figure 4.42, the evolution of the onset velocity with the droplet diameter at a constant dynamic viscosity is considered. For glycerol 50% with $\mu = 5.24\,\mathrm{mPa\,s}$, a power law with an exponent of -0.55 appears. Comparing it to binary collisions, given in figure 4.34, leads to the conclusion that the onset velocity decreases stronger with increasing droplet diameter in the binary case compared to ternary collisions.

In figure 4.43, the onset Weber number is plotted as a function of the Ohnesorge number for ternary collisions. Moreover, the fitted curve for binary collisions, as shown in figure 4.36, is sketched. Two conclusions can be drawn with the help of this diagram. First of all, the onset Weber number at a given Ohnesorge number is larger in the ternary than in the binary case. This was expected and already observed and discussed in section 4.1.3. Secondly, the data points in the diagram do not fall onto a single curve. As already mentioned for binary collisions of equal-sized (see section 4.2.1) and unequal-sized (see section 4.2.2) droplets, this indicates once more that the combination of (We, Oh) is not the right set of parameters to describe the onset of fragmentation for droplet collisions. Nevertheless it is considered in this thesis because established collision models in the literature are based on it (see section 2.4.2).

A more general definition of the onset of fragmentation can be obtained by representing

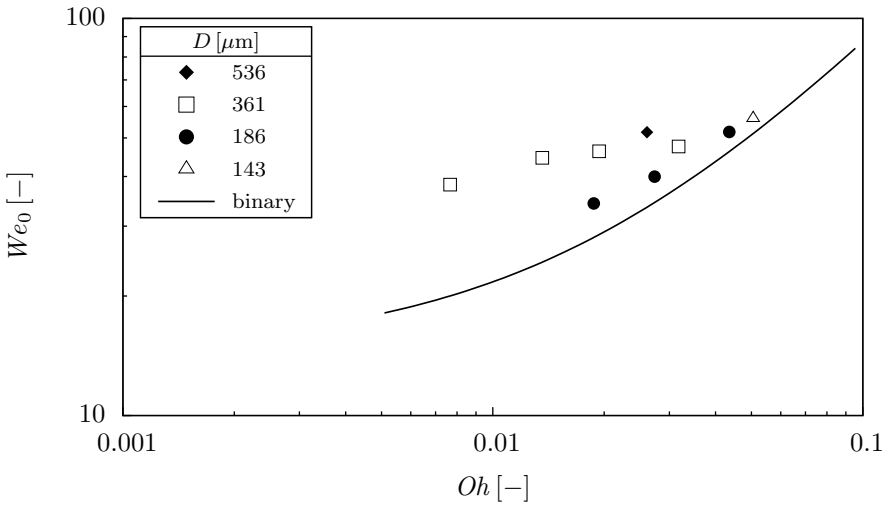

Figure 4.43: Evolution of the onset Weber number with the Ohnesorge number for ternary drop collisions. The black line is the fit curve of the results for binary collisions presented in figure 4.36. The used liquids are listed in table 3.2.

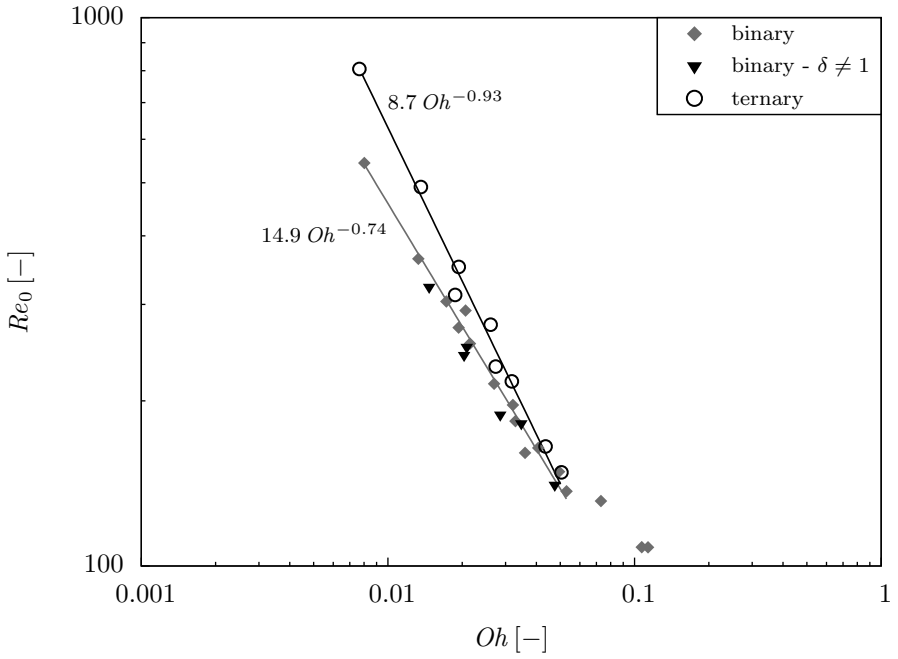

Figure 4.44: Correlation of the onset Reynolds number with the Ohnesorge number. The fit curve for binary collisions of equal-sized droplets (marked by grey diamonds) excludes collisions at $Oh > 0.06$. The used liquids are listed in tables 3.2 and 3.3.

it in terms of an onset Reynolds number Re_0 and Ohnesorge number. This can be seen in figure 4.44, where the results for ternary collisions are plotted as black circles. It can be seen that the data points fall perfectly onto a single line, which is defined by a power law with an exponent of -0.93. The results for binary collisions are also drawn in this diagram. The outcomes for binary collisions of equal-sized droplets are represented by grey diamonds. The power law with an exponent of -0.74 appears for small Ohnesorge numbers at $Oh < 0.06$, excluding the three data points on the right hand. Planchette *et al.* (2012) gathered the results for binary head-on collisions of seven different studies in the literature and showed that they all belong to a single line for low Ohnesorge numbers, which is defined by a power law between Re and Oh with an exponent close to -0.8. This agrees very well, with the measurements of the present study. Furthermore, the results for binary head-on collisions of unequal-sized droplets are also shown in figure 4.44. Here, Reynolds number and Ohnesorge number are calculated according to equations (4.2) and (4.3), respectively. The data points are marked by black triangles and correspond very well to the grey line representing the results for binary collisions of equal-sized droplets.

In conclusion, it can be said that the representation of the onset Reynolds number of fragmentation as a function of the Ohnesorge number has to be favoured over the representation in terms of Weber number and Ohnesorge number. The latter can be used to describe binary collisions of equal-sized droplets using one single liquid, but it does not represent the phenomenon as well as (Re, Oh) because it takes the dynamic viscosity incorrectly into account (see section 4.2.1). Describing the onset of fragmentation as a function of Reynolds number and Ohnesorge number can be applied to all types collisions investigated during the current study, including binary collisions of equal-sized and unequal-sized droplets as well as ternary collisions. The different exponents in figure 4.44 can be explained by different flow fields in the drops due to the quasi stationary central droplet in the ternary case. Moreover, Planchette *et al.* (2012) have shown that the onset of fragmentation for binary head-on collisions of immiscible liquids can be expressed by (Re, Oh). In this case the exponent of the Ohnesorge number appears to be around -0.5, which can be explained by a different flow field as well. This confirms the approach of representing the onset of fragmentation for head-on collisions in terms of Reynolds number and Ohnesorge number.

5 Modelling

In this chapter modelling attempts based on the literature are presented in order to explain the onset of fragmentation for binary and ternary liquid drop collisions theoretically. A completely analytical expression for the onset velocity U_0 is not developed, but individual periods of the collision are analysed. Therefore, the collision process is divided into two main phases (see figure 5.1). In the first phase of the collision, the droplets impinge on each other and deform into a disk shaped complex. Afterwards, in the second phase of the collision, this disk relaxes into a cylindrical shaped rod, which possibly breaks up into two equal-sized droplets or retracts into a spherical droplet.

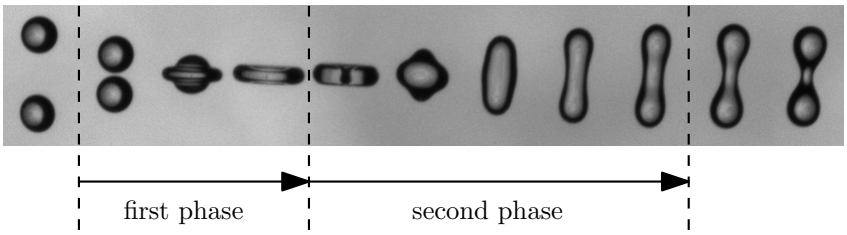

Figure 5.1: Collision process in two phases. The first phase lasts from the first contact of the two droplets until the merged disk reaches its maximum extension. During the second phase the disk relaxes into a cylinder.

In the first section of this chapter, the fragmentation criterion introduced by Ashgriz & Poo (1990) is verified for the results obtained in this study. Afterwards, the viscous energetic loss in the first phase of the collisions is analysed. Finally, an empirically obtained transition criterion analogous to figure 4.44 is introduced.

5.1 Fragmentation criterion

In the second phase of the collision, the deformed disk retracts due to surface tension forces and relaxes into a cylindrical shaped complex (see figure 5.1). Based on the

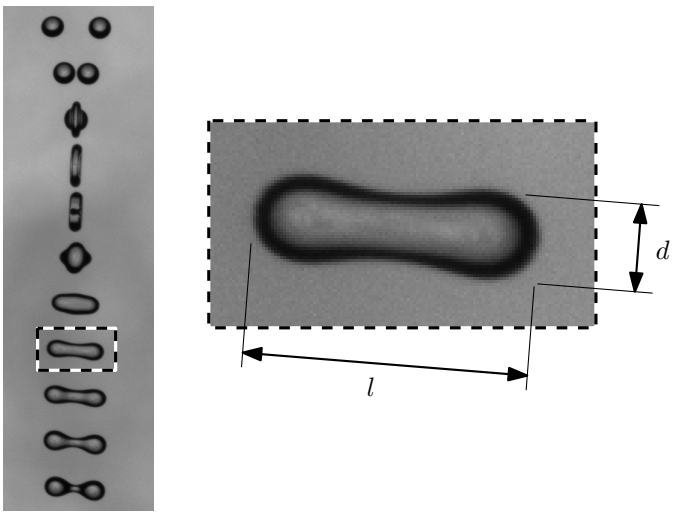

Figure 5.2: Second phase of a binary drop collision where a liquid cylinder is formed.

Rayleigh criterion (Rayleigh, 1879), Ashgriz & Poo (1990) introduced a fragmentation criterion for binary head-on collisions of water droplets. In order to minimise its total surface energy, the liquid cylinder breaks up into two equal-sized droplets when its length-to-diameter ratio exceeds the critical value of π. However, it has been shown that the breakup mechanism of this cylinder has nothing in common with the classical Plateau-Rayleigh instability of a liquid column (Stone & Leal, 1989; Notz & Basaran, 2004). Nevertheless, experimental observations show very good agreement of the onset of fragmentation and the exceeding of the critical length-to-diameter ratio of the cylinder. Lately, Planchette *et al.* (2012) used it as a fragmentation criterion for their model, describing the onset velocity for binary collisions of immiscible liquids. In this work we follow the same approach and evaluate if the criterion is applicable to the results obtained for binary and ternary collisions.

In order to determine the length-to-diameter ratio of the cylindrical shaped drop, its length l and its diameter d must be measured, which is pictured in figure 5.2. Thus, the aspect ratio ζ can be calculated by

$$\zeta = \frac{l}{d}\,. \tag{5.1}$$

Technically speaking ζ is time-dependent, but it can be seen in figure 5.2 that the shape of the cut out and the following cylinder are almost identical. It can be concluded that the shape of the maximum extended cylinder varies little in time compared to the used sampling frequency. This was confirmed by examining other photographs obtained

during this study at typical sampling frequencies from 5 to 20 kHz.

5.1.1 Binary drop collisions

In order to examine if the fragmentation criterion can be applied to binary head-on collisions, the critical aspect ratio ζ_0 has been defined for all obtained onset velocities (see table 4.2). Two values of ζ_0 are required for each measurement, one at coalescence and one at separation defining the lower and upper limits, respectively. The results are plotted in figure 5.3 with error bars between the two values of ζ_0. The silicon oils are marked separately (SO). For small Ohnesorge numbers, ζ_0 is close to the value of π, which agrees very well with the Rayleigh criterion. However, above a certain Ohnesorge number, say 0.06, the critical aspect ratio increases. Thus, the fragmentation criterion of $\zeta_0 = \pi$ cannot be applied to binary collisions at higher Ohnesorge numbers. This is in good agreement with figure 4.36 and figure 4.44, where two regimes can be observed for $Oh < 0.06$ and $Oh > 0.06$, respectively, indicating a change in the breakup mechanism. It results that, for small Ohnesorge numbers ($Oh < 0.06$), the Rayleigh criterion can be used for binary head-on collisions.

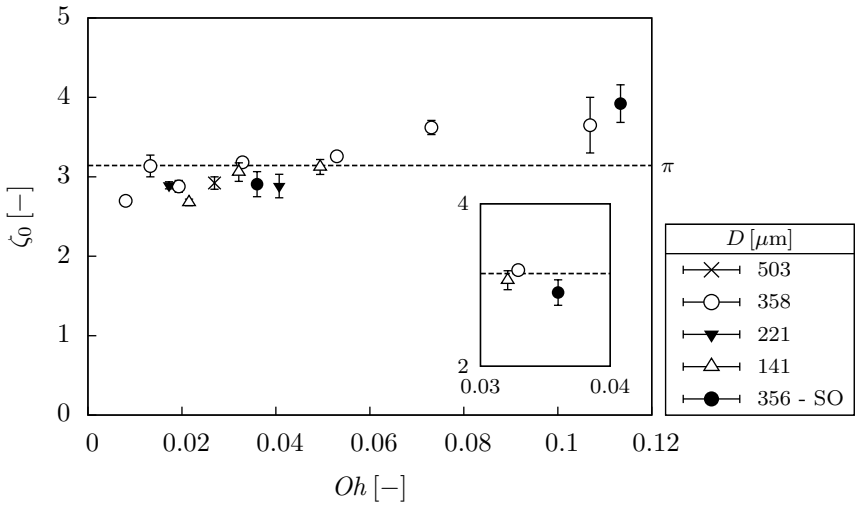

Figure 5.3: Correlation of ζ_0 with the Ohnesorge number. At $Oh < 0.06$ the critical aspect ratio is in good agreement with the Rayleigh criterion, which is drawn with a dashed line ($\zeta_0 = \pi$). The used liquids are listed in table 3.2.

5.1.2 Ternary drop collisions

The critical aspect ratios describing the transition between coalescence and reflexive separation for ternary head-on collisions are drawn in figure 5.4 against the Ohnesorge number. For each onset velocity (see table 4.4), the value of ζ_0 at coalescence and separation is estimated, leading to a data point at the average with an error bar between these two values in the diagram. The Rayleigh criterion at $\zeta_0 = \pi$ is marked by a dashed line. It can be seen that the data correlates with a critical aspect ratio π. Deviations from this value can be explained by measurement inaccuracies and the time dependency of ζ, combined with finite sampling frequencies between 5 and 20 kHz. The measuring accuracy of ζ is about 3.3%, assuming an error of ± 1 px for the estimation of l (typically 100 px) and d (typically 32 px).

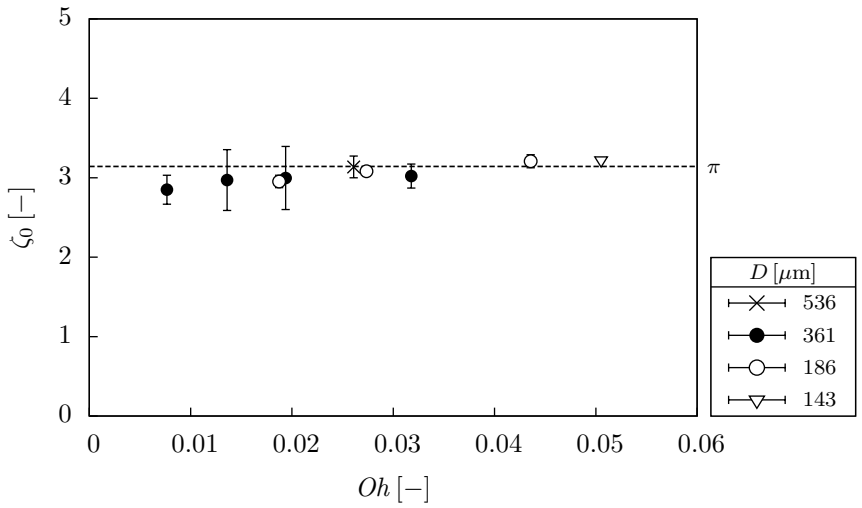

Figure 5.4: Evolution of ζ_0 with the Ohnesorge number. The critical aspect ratio is in good agreement with the Rayleigh criterion, which is drawn by a dashed line ($\zeta_0 = \pi$). The used liquids are listed in table 3.2.

In conclusion, the Rayleigh criterion can be applied to determine the onset of fragmentation for ternary head-on collisions in the examined range of Ohnesorge numbers (see figure 5.4). This agrees very well with the observations made for binary collisions, which is not unexpected, regarding that the process of the collision during the second phase is nearly identical for the binary and the ternary case.

5.2 First phase of the collision

The first phase of the collision of two or more droplets lasts from their first contact until the formed disk reaches its maximum extension (see figure 5.1). At the state of maximum extension it is assumed that the internal flow has stopped and all the energy is transformed into surface energy. Thus, it can be balanced to the initial energy, and the dissipated energy can be estimated.

In order to calculate the surface energy of the deformed disk, its geometric parameters are needed. In figure 5.5, the maximum diameter D_{max} and its width w are exemplarily defined for a binary collision. A problem in the estimation of D_{max} is that, in the photographs, the droplets are shown at discrete time steps. Therefore, one cannot verify if the disk is currently at its maximum deformation. However, Roisman *et al.* (2012) showed that, around its maximum value, the diameter of the disk varies little in time for immiscible liquids. This was observed for miscible liquids during this work as well while comparing the measured maximum diameters at a certain velocity. The variation from an imaginary average maximum diameter is about $\pm 5\,\%$.

The estimation of the surface area of the disk can be done differently. Jiang *et al.* (1992) proposed a spheroid with an elliptic cross section which leads to a surface area

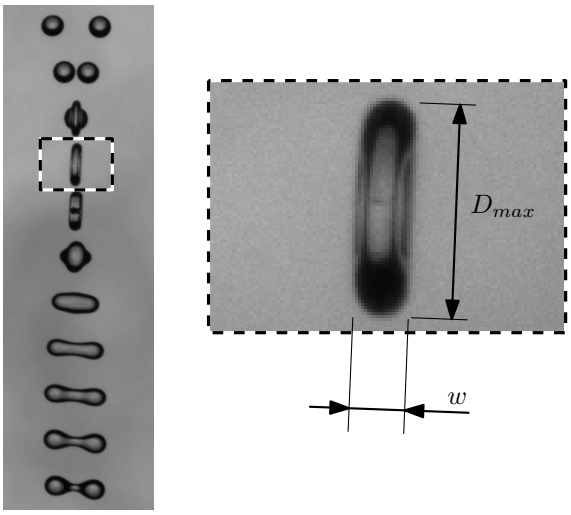

Figure 5.5: First phase of a binary drop collision, where the formed disk reaches its maximum extension.

of

$$S = \frac{1}{2}\pi D_{max}^2 \left[1 + \frac{1}{\beta}\frac{1}{(\beta^2-1)^{1/2}} \ln\left(\beta + (\beta^2-1)^{1/2}\right)\right] \quad \text{with} \quad \beta = \frac{D_{max}}{w} > 1\,. \tag{5.2}$$

Photographs of Ashgriz & Poo (1990) and the work of Roisman *et al.* (2012) showed that the disk looks more like a torus, with a lamella in the middle instead of a hole. Assuming a perfect torus with an infinitely thin lamella, as sketched in figure 5.6, leads to a surface area of

$$S = \pi^2\, w\,(D_{max} - w) + \frac{1}{2}\pi\,(D_{max} - 2w)^2\,. \tag{5.3}$$

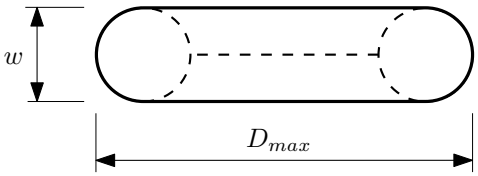

Figure 5.6: Torus with infinitely thin lamella in the centre.

However, for simplicity, a simpler approach is used in this work. The surface area is estimated by an infinitely thin disk:

$$S = \frac{1}{2}\pi D_{max}^2\,. \tag{5.4}$$

This approach looks at the first glance very crude. In fact, the surface areas calculated for the spheroid (see equation (5.2)) and for the torus (see equation (5.3)) are on an average 17.5% and 44% larger, respectively, than the results obtained for the disk (see equation (5.4)). Nevertheless, the qualitative results should be the same as using a more complex surface area like in equations (5.2) or (5.3). Moreover, the shape of the merged complex at the onset of fragmentation is very close to a disk. The reasons for this approach are, on the one hand, as already mentioned, simplicity, and on the other that the disk width w lies in most cases only between 15 and 20 px. Assuming an error of ± 1 px for the measurement of w leads to a relative error between 5 and 6.7%. On the contrary, the maximum diameter is typically in the order of $D_{max} = 80$ px, leading to a relative measurement error of only 1.25%. By using equation (5.4) for the calculation of the surface area, the relatively large measurement error of the disk width is not considered.

5.2.1 Binary drop collisions

Below the amount of energy dissipated in the first phase of binary head-on collisions of equal-sized droplets is investigated. To do so, two different approaches are considered.

Modelling of the viscous loss

Following the approach of Jiang *et al.* (1992), the initial energy of the droplets can be balanced to the energy of the merged disk at its maximum deformation by

$$E_{ini} = \sigma S + \Phi_1 \,, \tag{5.5}$$

where E_{ini} represents the initial kinetic and surface energies of the droplets, S is the surface area of the deformed disk according to equation (5.4) and Φ_1 stands for the dissipated energy and is a function of the dynamic viscosity. The initial energy of the droplets can be calculated by

$$E_{ini} = 2\left[\frac{1}{6}\pi D^3 \frac{1}{2}\rho\left(\frac{U}{2}\right)^2 + \pi\sigma D^2\right] , \tag{5.6}$$

assuming equal-sized droplets. Introducing equation (5.6) into equation (5.5) and normalizing it by $2\pi\sigma D^2$ leads to the non-dimensional equation

$$\underbrace{\frac{S}{2\pi\sigma D^2}}_{\hat{S}} = 1 + \underbrace{\frac{We}{48}}_{We^*}\left(1 - \underbrace{\frac{48\,\Phi_1}{2\pi\sigma D^2\, We}}_{\hat{\alpha}}\right) , \tag{5.7}$$

which can be written as

$$\hat{S} = 1 + We^*(1 - \hat{\alpha})\,. \tag{5.8}$$

Here, $\hat{S}$ represents a non-dimensional surface area, We^* is the Weber number divided by the constant factor 48 and $\hat{\alpha}$ can be seen as a dissipation coefficient.

In figure 5.7, the obtained results for binary head-on collisions are plotted as $\hat{S}$ depending on We^*. These are the results from the measurements of the map of regimes (see figure 4.11) and from the measurements of the onset velocities (see table 4.2). The results for glycerol 50%, marked by grey filled circles, spread over a wide range of We^* and liquids with dynamic viscosities smaller and larger than 5.24 appear only around

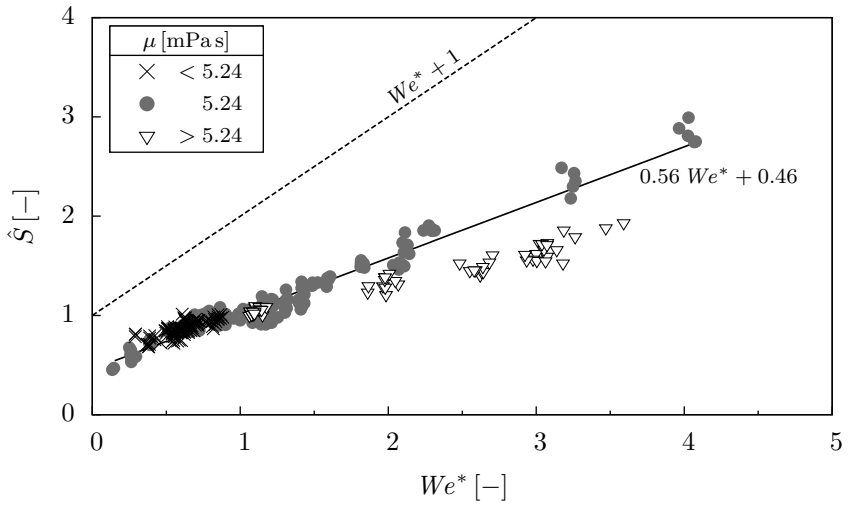

Figure 5.7: Evolution of $\hat{S}$ with We^* for the determination of the viscous loss in the first phase of binary drop collisions. The dashed line stands for the lossless case. The solid line represents the correlation of the experimental data marked by the grey filled circles.

certain Weber numbers. The lossless case ($\hat{\alpha} = 0$) is marked by a dashed line. The fitted solid line belongs to the grey data points with $\mu = 5.24\,\mathrm{mPa\,s}$.

The model by Jiang *et al.* (1992) predicts that the energy dissipation at the maximum deformation of the disk is independent of the dynamic viscosity and can be characterised by a single dissipation coefficient $\hat{\alpha}$. However, Willis & Orme (2003) disproved this statement and showed that the viscous dissipation depends on μ. This can be seen in figure 5.7 as well. For a viscosity of $\mu \leq 5.24\,\mathrm{mPa\,s}$, the data points fit to a single line, but for higher viscosities a deviation from the line can be observed, implying increasing viscous losses with increasing dynamic viscosity. This is a limitation of the model of Jiang *et al.* (1992), since the dependency of $\hat{\alpha}$ on μ is not considered. For low Weber numbers $We^* < 1$ the difference in dissipated energy for various liquids is not very large, but technically speaking, the dissipation coefficient $\hat{\alpha}$ has to be determined for each liquid. In the case of glycerol 50%, using equation (5.4) for the calculation of the surface area, a value of $\hat{\alpha} \approx 0.44$ is obtained.

Modelling of the maximum diameter

An alternative method to model the first phase of the collision can be found in the work of Chandra & Avedisian (1991). They modelled the maximum diameter of a

drop impinging on a solid surface. Their approach is used in the current section to predict the maximum diameter in the first phase of binary drop collisions. It is based on energy conservation, as given in equation (5.5). The initial energy and the surface area are given by equations (5.6) and (5.4). The viscous dissipation can be estimated by

$$\Phi_1 = \phi V t \,, \tag{5.9}$$

where ϕ is the viscous dissipation function, V the combined liquid volume and t the time taken by the disk to reach its maximum extension. The volume can be calculated by

$$V = \frac{1}{3}\pi D^3 \approx \frac{1}{4}\pi D_{max}^2 \, w \,. \tag{5.10}$$

The estimation of the viscous dissipation function ϕ and the time t is a very delicate issue. Chandra & Avedisian (1991) assumed for the former

$$\phi \approx \mu \left(\frac{U_\infty}{L_\infty} \right)^2 \,, \tag{5.11}$$

where U_∞ is a characteristic velocity and L_∞ a characteristic length scale. For binary drop collisions these quantities are $U_\infty = U/2$ and $L_\infty = w/2$. The time is estimated by $t \approx 2D/U$.

Pasandideh-Fard *et al.* (1996) enhanced the model of Chandra & Avedisian (1991)

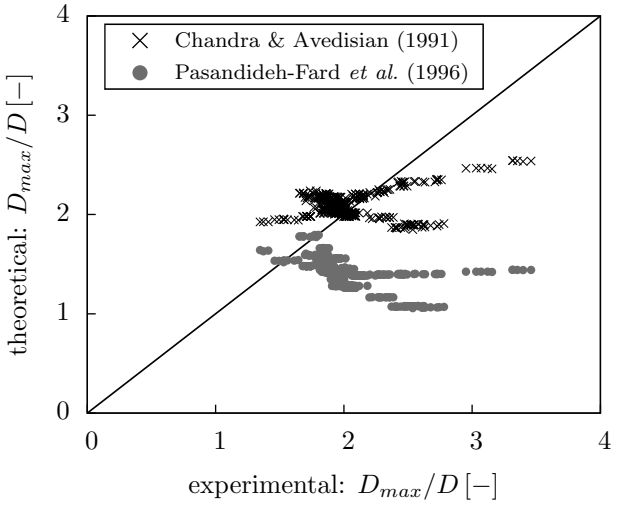

Figure 5.8: Predicted maximum diameter using two models of the literature compared to experimental results. The diagonal indicates perfect agreement between modelled and measured maximum diameters.

by estimating the characteristic length in equation (5.11) by $L_\infty = (2D_{PF})/(\sqrt{\mathrm{Re}_{PF}})$, which is equivalent to the boundary layer thickness at the solid-liquid interface. The time is approximated to be $t = (8\,D_{PF})/(3\,U_{PF}\,)$. Adapting these quantities for binary drop collisions leads to $L_\infty = (2\sqrt{2}D)/(\sqrt{\mathrm{Re}}\,)$ and $t = (16\,D)/(3\,U)$. Unfortunately, the models of Chandra & Avedisian (1991) and Pasandideh-Fard *et al.* (1996) are not appropriate to describe D_{max} for binary liquid drop collisions. The predicted diameters are not conform with our measurements, which can be seen in figure 5.8. This indicates that the velocity gradient at binary drop collisions (see equation (5.11)) and at the impact of a drop onto a solid wall are not the same. This seems reasonable, because at the wall a no-slip boundary condition can be assumed, which is not the case for the collision of two drops.

In order to describe the maximum diameter for binary drop collisions an empirical ansatz is introduced to calculate the viscous dissipation. For this all the quantities in equation 5.9 are calculated using the characteristic parameters D and U, which leads to

$$\phi = \varepsilon \frac{1}{2} \pi \mu U D^2\,, \tag{5.12}$$

where ε is a constant factor which will be empirically determined. Substituting equation (5.6), (5.4) and (5.12) into equation (5.5), and multiplying it with $2/\pi\sigma D^2$, leads to

$$\frac{D_{max}}{D} = \sqrt{\frac{1}{12}\,We + 4 - \varepsilon \frac{We}{Re}}\,. \tag{5.13}$$

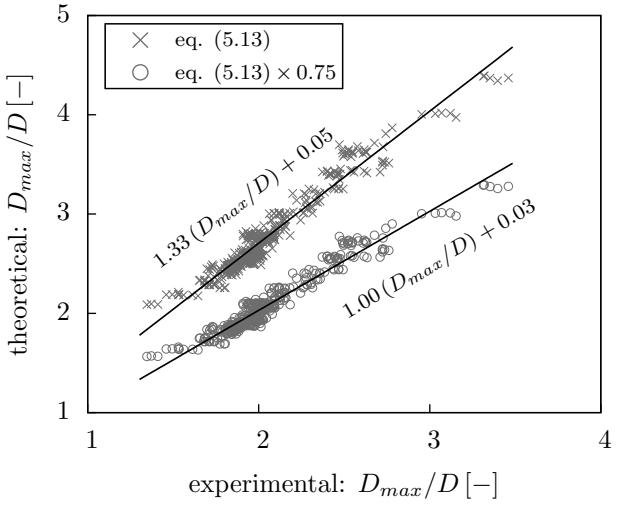

Figure 5.9: Predicted maximum diameter compared to experimental results. Empirical tuning leads to a value for ε of 2.3.

In figure 5.9, the predictions of equation (5.13) are compared to the experimental data. The data points are brought to a single line with the help of an empirically determined value of $\varepsilon = 2.3$. The slope of the line with a value of ≈ 1.33 shows a discrepancy between theoretical prediction and experiment. This disagreement can be eliminated by multiplying the theoretical results for D_{max}/D with a prefactor of 0.75 on the grounds that the surface area of the complex was approximated quite crude to the one of a disk in the first place (see equation (5.4)). Thus, the obtained agreement with the experimental data appears to be very good.

5.2.2 Ternary drop collisions

In this section, the amount of dissipated energy in the first phase of ternary liquid drop collisions is investigated. Analogous to the binary case (see section 5.2.1) two different approaches are considered.

Modelling of the viscous loss

Below, the approach of Jiang *et al.* (1992) is applied to the first phase of ternary liquid drop collisions. For the initial energy, the surface energy of the central droplet is added to equation (5.6), which leads to

$$E_{ini} = 2\left[\frac{1}{6}\pi D^3 \frac{1}{2}\rho\left(\frac{U}{2}\right)^2 + \frac{3}{2}\pi\sigma D^2\right]. \tag{5.14}$$

Applying the same procedure as in section 5.2.1, the non-dimensional energy balance for ternary collisions yields to

$$\hat{S} = 1.5 + We^*(1-\hat{\alpha}). \tag{5.15}$$

In figure 5.10, the results for $\hat{S}$ are plotted against We^*. Similar to the binary case, these are the results obtained from the measurements for the map of regimes (see figure 4.26) and from the measurements of the onset velocity (see table 4.4). The lossless case with $\hat{\alpha} = 0$ is marked by a dashed line. The solid line represents the curve fitted for the data points marked by grey filled circles. The data corresponds very well to the solid line with a loss coefficient of $\hat{\alpha} \approx 0.28$. However, as already discussed in section

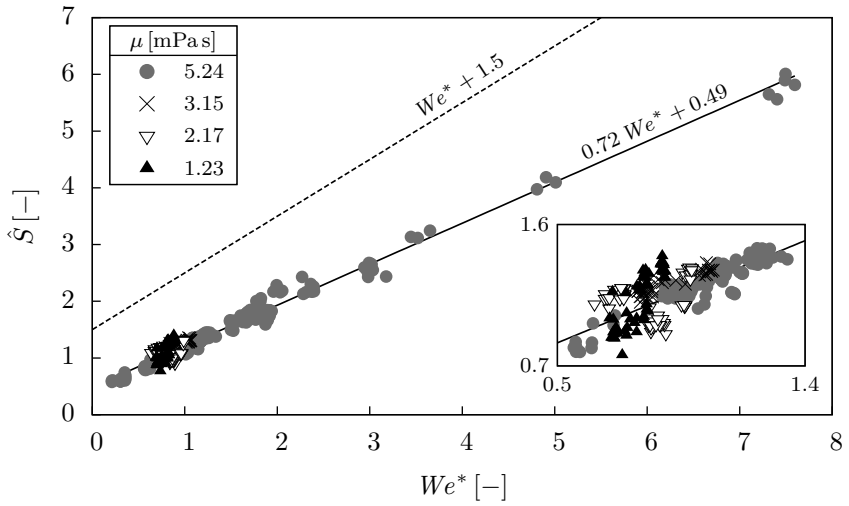

Figure 5.10: Evolution of $\hat{S}$ with We^* for the determination of the viscous loss in the first phase of ternary drop collisions. The dashed line stands for the lossless case. The solid line represents the correlation of the experimental data marked by grey filled circles.

5.2.1 the amount of dissipated energy in the first phase at binary collisions depends on the dynamic viscosity, leading to a different $\hat{\alpha}$ for each liquid. Thus, it is very likely that it is valid for ternary collisions as well. It is interesting to note that, for a given liquid, say glycerol 50%, the loss of kinetic energy in the first phase is larger for binary ($\hat{\alpha} \approx 0.44$) than for ternary collisions ($\hat{\alpha} \approx 0.28$). Possibly, this can be explained by a smaller velocity gradient at ternary collisions because of the central droplet.

Modelling of the maximum diameter

The empirical model for the maximum diameter of the disk, based on the work of Chandra & Avedisian (1991), is applied to ternary drop collisions analogous to the binary case given in section 5.2.1. The energy is balanced as given in equation (5.5), calculating the initial energy according to equation (5.14). The surface area of the disk is defined by equation (5.4) and the viscous dissipation is calculated analogous to equation (5.12). Multiplying with $2/\pi\sigma D^2$ and rearranging leads to an equation for the maximum diameter of

$$\frac{D_{max}}{D} = \sqrt{\frac{1}{12}\,We + 6 - \varepsilon\frac{We}{Re}}\,. \tag{5.16}$$

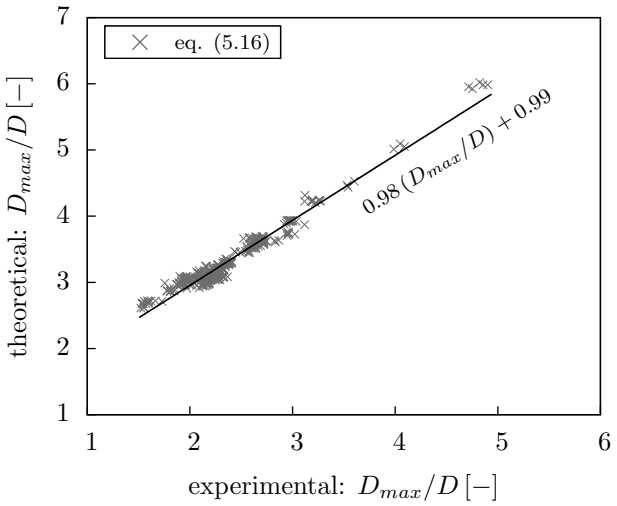

Figure 5.11: Predicted diameter according to equation (5.16) with $\varepsilon = 0.25$ compared to experimental results.

In figure 5.11, the results of equation (5.16) are compared to the experimental results. The prefactor ε is empirically tuned to a value of 0.25. The slope of the fitted line shows very good agreement of the calculated and the measured values, but the intersect is close to a value of one. This cannot be corrected by a constant prefactor as in the binary case (see figure 5.9). This discrepancy cannot be explained yet, but it indicates that the approach for the viscous dissipation given by equation (5.12) is not appropriate to model the viscous loss for ternary drop collisions. Furthermore, the fact that there seems to be a fundamental difference between binary and ternary drop collisions in terms of viscous losses during the first phase of the collision, as indicated comparing figure 5.7 to 5.10 and figure 5.9 to 5.11, is supported.

5.3 Second phase of the collision

In the second phase of the collision, the deformed disk retracts due to surface tension forces and relaxes into a cylindrical shaped complex (see figure 5.1). This cylinder may breakup into two equal-sized droplets. For the second phase no theoretical model is deduced, but an experimentally observed transition criterion describing the transition between coalescence and separation is presented.

5.3.1 Binary drop collisions

There are several options to represent the transition between coalescence and separation for binary head-on collisions. Jiang *et al.* (1992) plotted a critical transition Weber number ($We^* = We/48$) as a function of the dynamic viscosity divided by surface tension. However, this type of representation is not appropriate to represent results obtained with different droplet sizes or liquids with different surface tension. This can be seen in figure 5.12, where the results of Jiang *et al.* (1992) are marked by grey diamonds. It can be observed that their results agree quite well with the present measurements at an equivalent droplet diameter of 358 μm. However, the results obtained for other droplet diameters differ from them because the droplet diameter is not considered on the abscissa. Moreover, the influences of dynamic viscosity and surface tension are not correctly accounted for. This can be seen when comparing the results obtained with glycerol and silicon oil as the liquids at a droplet diameter of $D \approx 357 \mu m$ and $\mu\,\sigma^{-1} \approx 0.14\,\mathrm{s\,m^{-1}}$.

Qian & Law (1997) developed a transition criterion showing a linear dependency of Weber number on the Ohnesorge number (see section 2.4.2). This correlation was observed for binary collisions during this work as well (see figure 4.36). However, this kind of representation only works for binary collisions and only when one single liquid is involved. Thus, presenting the onset of fragmentation as a function of an onset

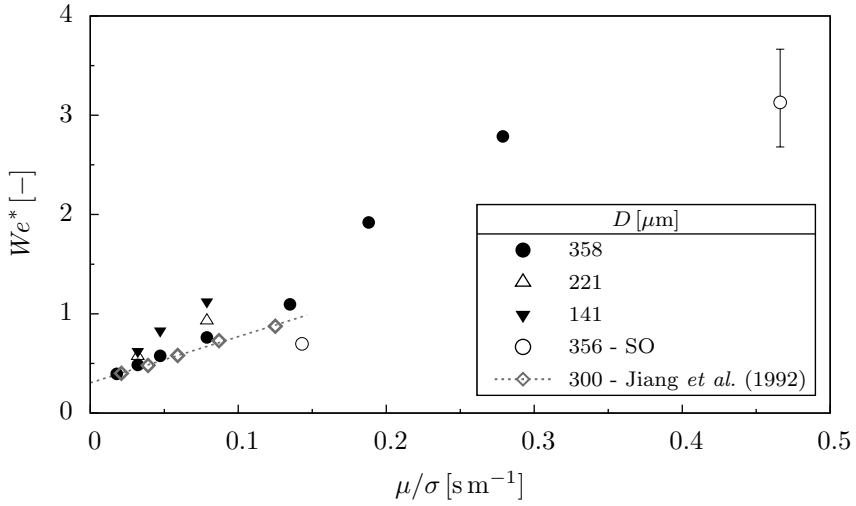

Figure 5.12: Evolution of the transition Weber number with the dynamic viscosity divided by surface tension as proposed by Jiang *et al.* (1992). The used liquids are listed in table 3.2.

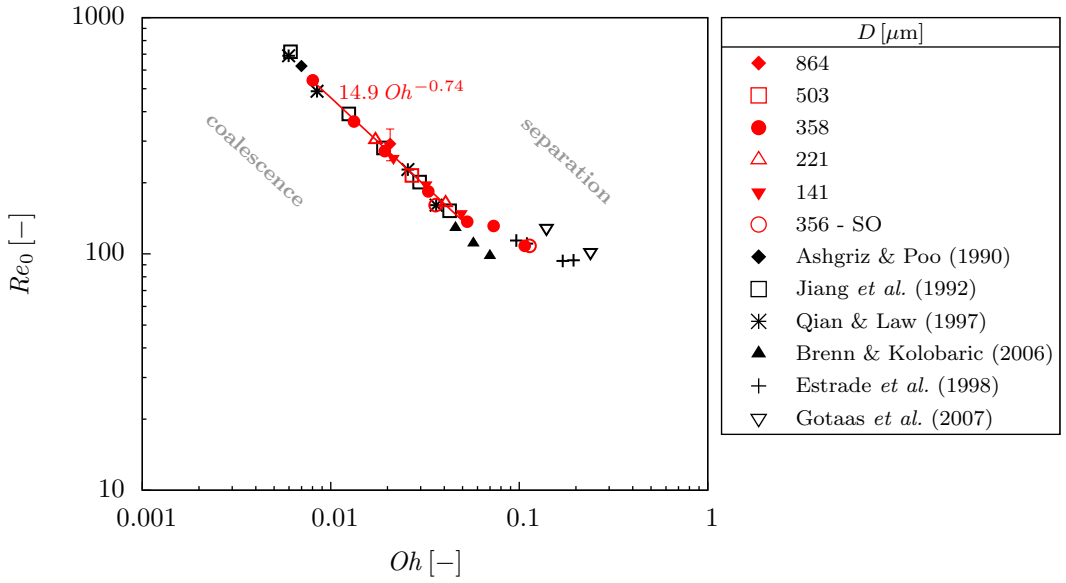

Figure 5.13: Correlation of the onset Reynolds number with the Ohnesorge number for binary head-on collisions of equal-sized droplets. The used liquids are listed in table 3.2.

Reynolds number Re_0 and Ohnesorge number is preferred in this study. Figure 5.13 shows the onset Reynolds number as a function of Ohnesorge number for the present results of binary drop collisions. It can be seen that a power law with an exponent of -0.74 appears for low Ohnesorge numbers ($Oh < 0.06$). The obtained results agree very well with results from the literature.

5.3.2 Ternary drop collisions

The onset of fragmentation for ternary head-on collisions cannot be described in terms of Weber number and Ohnesorge number (see figure 4.43). It has to be represented in terms of an onset Reynolds number and Ohnesorge number, which can be seen in figure 5.14. At a given Ohnesorge number for $Re < Re_0$ coalescence occurs, whereas for $Re > Re_0$ the collision results in separation. For the performed measurements a power law with an exponent of -0.93 appears.

In conclusion, representing the onset of fragmentation for head-on drop collisions in terms of Reynolds number and Ohnesorge number appears to be generally applicable. For binary and ternary drop collisions with a single liquid, and binary drop collisions

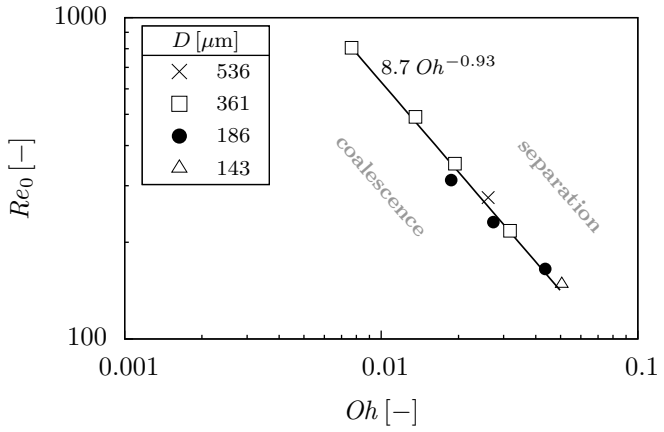

Figure 5.14: Evolution of the onset Reynolds number with the Ohnesorge number for ternary head-on collisions of equal-sized droplets. The used liquids can be found in table 3.2.

with two immiscible liquids, power laws with different exponents occur in the (Re, Oh) chart describing this boundary. Planchette *et al.* (2012) developed a transition criterion characterising this correlation for binary collisions with two immiscible liquids. For binary and ternary drop collisions with a single liquid no theoretical models exist in the literature considering the scaling law between Reynolds number and Ohnesorge number. We believe that this would be promising a approach to model the transition between coalescence and separation for head-on collisions.

6 Summary and conclusions

In the present study binary and ternary drop collisions of the same liquid at well-defined conditions of impact were investigated. The collisions were achieved using piezoceramic drop generators which produced stable monodisperse liquid droplet streams. Collision parameters were obtained by analysing acquired photographs. The objectives of the present study were to compare the collision outcomes occurring at ternary drop collisions and their transitions to the ones of binary collisions.

A (X, We) nomogram was plotted to represent the regime map of ternary drop collisions at an average droplet diameter of $D \approx 379\,\mu$m using glycerol 50% as the liquid. Similar to binary drop collisions, four main regimes, namely coalescence, bouncing, stretching separation and reflexive separation, were observed. The transitions in the collision regime map bear resemblance to the transitions observed for binary drop collisions. However, two significant differences were observed. First of all, due to the central droplet at ternary collisions, more initial kinetic energy is required for separation to occur than in the binary case. Secondly, at small Weber numbers the transition between coalescence and bouncing is shifted to larger non-dimensional impact parameters with decreasing Weber number at the ternary case, whereas the opposite is true for binary collisions.

The onset of fragmentation at head-on collisions was investigated for a wide range of liquids and droplet diameters. The results obtained for binary drop collisions show a linear correlation between Weber number and Ohnesorge number which can also be found in the literature. On the contrary, the onset of fragmentation at ternary head-on collisions cannot be explained in terms of these two non-dimensional numbers. In that case, a power law between Reynolds number and Ohnesorge number with an exponent close to -1 can be used to describe the fragmentation threshold. This power law was observed for binary head-on collisions as well, but with an exponent close to -0.75. The difference in the exponents can be explained due to different flow fields in the

merged droplet. Note that the onset of fragmentation for binary head-on collisions of immiscible liquids can also be represented by (Re, Oh).

Upon further investigation of head-on collisions it was shown that the viscous loss during the first phase of the collision, where the merged disk reaches its maximum extension, is larger for binary than for ternary collisions. This can be explained by the absence of the central droplet at the binary case, resulting in a larger velocity gradient. Moreover, an empirical model for the maximum diameter of the disk formed after the impact, based on theoretical models predicting the maximum diameter of a droplet impinging on a solid wall, was introduced for binary drop collisions. This could not be applied for ternary collisions. This indicates that the first phase of binary and ternary drop collisions differs fundamentally. On the contrary, it has been shown that a fragmentation criterion, defined by the critical length-to-diameter ratio of the liquid cylinder, which is formed in the second phase of the collision, can be applied to binary and ternary drop collisions in a range of low Ohnesorge numbers ($Oh < 0.06$). Similar to the classical Rayleigh criterion, the critical value of this length-to-diameter ratio is π.

Overall, the collision behaviour of ternary head-on collisions differs from binary head-on collisions, especially in the first period after the impact. Measuring the onset of fragmentation for binary and ternary head-on collisions leads to a power law between the Reynolds and Ohnesorge numbers with an exponent close to -0.75 and -1, respectively. A theoretical model considering these power laws for miscible liquids has not been developed yet, but we believe that this would be a promising approach to model the transition between coalescence and separation for head-on collisions.

Bibliography

Ashgriz, N. & Poo, J. Y. (1990) Coalescence and separation in binary collisions of liquid drops. *Journal of Fluid Mechanics* **221**, 183–204.

Brazier-Smith, P. R., Jennings, S. G. & Latham, J. (1972) The interaction of falling water drops: coalescence. *Proceedings of the Royal Society of London. A* **326**, 393–408.

Brenn, G., Durst, F. & Tropea, C. (1996) Monodisperse sprays for various purposes - their production and characteristics. *Particle & Particle Systems Characterization* **13**, 179–185.

Brenn, G. & Frohn, A. (1989) Collision and coalescence of droplets of various liquids. *Journal of Aerosol Science* **20**, 1027–1030.

Brenn, G. & Kolobaric, V. (2006) Satellite droplet formation by unstable binary drop collisions. *Physics of Fluids* **18**. 087101.

Brenn, G. (2011) Droplet collision. In *Handbook of Atomization and Sprays: Theory and Applications*. Ed. by N. Ashgriz. New York: Springer. Chap. 7, pp. 157–181.

Chandra, S. & Avedisian, C. T. (1991) On the collisions of a droplet with a solid surface. *Proceedings of the Royal Society of London. A* **432**, 13–41.

Chen, R.-H. & Chen, C.-T. (2006) Collisions between immiscible drops with large surface tension difference: diesel oil and water. *Experiments in Fluids* **41**, 453–461.

Estrade, J.-P., Berthoumieu, P., Lavergne, G. & Biscos, Y. (1998) Experimental investigation of dynamic binary collisions of various liquids. In *8th International Symposium on Flow Visualization*. Ed. by G. M. Carlomagno & I. Grant.

Fraser, R. P. & Eisenklam, P. (1953) Research into the performance of atomizers for liquids. *Journal of the Imperial College Chemical Engineering Society* **7**, 52–68.

Gao, T.-C., Chen, R.-H., Pu, J.-Y. & Lin, T.-H. (2005) Collision between an ethanol drop and a water drop. *Experiments in Fluids* **38**, 731–738.

de Gennes, P.-G., Brocçhard-Wyart, F. & Quéré, D. (2004) Capillarity and wetting phenomena: Drops, Bubbles, Pearls, Waves. New York: Springer.

Gotaas, C., Havelka, P., Jakobsen, H. A., Svendsen, H. F., Hase, M., Roth, N. & Weigand, B. (2007) Effect of viscosity on droplet-droplet collision outcome: Experimental study and numerical simulation. *Physics of Fluids* **19**. 102106.

Jiang, Y. J., Umemura, A. & Law, C. K. (1992) An experimental investigation in the collision behaviour of hydrocarbon droplets. *Journal of Fluid Mechanics* **234**, 171–190.

Ko, G. H. & Ryou, H. S. (2005) Modeling of droplet collision-induced breakup process. *International Journal of Multiphase Flow* **31**, 723–738.

Le, H. P. (1998) Progress and trends in ink-jet printing technology. *Journal of Imaging Science and Technology* **42** (1), 49–62.

Lefebvre, A. H. (1989) Atomization and sprays. New York: Hemisphere Publishing Corporation.

Mackay, G. D. M. & Mason, S. G. (1963) The gravity approach of coalescence of fluid drops at liquid interfaces. *The Canadian Journal of Chemical Engineering* **41** (5), 203–212.

Montgomery, D. N. (1970) Collision and coalescence of water drops. *Journal of Atmospheric Sciences* **28**, 291–293.

Notz, P. K. & Basaran, O. A. (2004) Dynamics and breakup of a contracting liquid ligament. *Journal of Fluid Mechanics* **512**, 223–256.

von Ohnesorge, W. (1936) Die Bildung von Tropfen an Düsen und die Auflösung flüssiger Strahlen. *Zeitschrift für angewandte Mathematik und Mechanik* **16** (6), 355–358.

Orme, M. (1997) Experiments on droplet collisions, bounce, coalescence and disruption. *Progress in Energy and Combustion Science* **23**, 65–79.

Pasandideh-Fard, M., Qiao, Y. M., Chandra, S. & Mostaghimi, J. (1996) Capillary effects during droplet impact on a solid surface. *Physics of Fluids* **8** (3), 650–659.

Planchette, C. (2011) Collisions de gouttes asymétriques. PhD thesis. Université de Paris-Est Marne-la-Vallée.

Planchette, C., Lorenceau, E. & Brenn, G. (2010) Liquid encapsulation by binary collisions of immiscible liquid drops. *Colloids and Surface A: Physicochemical and Engineering Aspects* **365**, 89–94.

Planchette, C., Lorenceau, E. & Brenn, G. (2012) The onset of fragmentation in binary liquid drop collisions. *Journal of Fluid Mechanics* **702**, 5–25.

Plateau, J. A. F. (1873) Statique expérimentale et théorique des liquides soumis aux seules forces moléculaires. Paris: Gauthier-Villars.

Qian, J. & Law, C. K. (1997) Regimes of coalescence and separation in droplet collision. *Journal of Fluid Mechanics* **331**, 59–80.

Rayleigh, Lord (1878) On the instability of jets. *Proceedings of the London Mathematical Society* **10**, 4–13.

Rayleigh, Lord (1879) On the capillary phenomena of jets. *Proceedings of the Royal Society of London* **29**, 71–97.

Rayleigh, Lord (1896) The Theory of Sound. 2nd ed. Vol. II. London: Macmillan & Co.

Reitz, R. D. (1978) Atomization and other breakup regimes of a liquid jet. PhD thesis. Princeton University.

Roisman, I. V., Planchette, C., Lorenceau, E. & Brenn, G. (2012) Binary collisions of drops of immiscible liquids. *Journal of Fluid Mechanics* **690**, 512–535.

Saroka, M. D. (2001) Three-dimensional numerical investigation of drop collisions in a vacuum. PhD thesis. State University of New York at Buffalo.

Spurk, J. H. & Aksel, N. (2007) Strömungslehre: Einführung in die Theorie der Strömungen. 7th ed. Berlin Heidelberg: Springer.

Stone, H. A., Bentley, B. J. & Leal, L. G. (1986) An experimental study of transient effects in the breakup of viscous drops. *Journal of Fluid Mechanics* **173**, 131–158.

Stone, H. A. & Leal, L. G. (1989) Relaxation and breakup of an initially extended drop in an otherwise quiescent fluid. *Journal of Fluid Mechanics* **198**, 399–427.

Walzel, P. (2010) Spraying and atomizing of liquids. In *Ullmann's Encyclopedia of Industrial Chemistry*. Weinheim: Wiley-VCH.

Weber, C. (1931) Zum Zerfall eines Flüssigkeitsstrahles. *Zeitschrift für angewandte Mathematik und Mechanik* **11** (2), 136–154.

Willis, K. D. & Orme, M. (2000) Experiments on the dynamics of droplet collisions in a vacuum. *Experiments in Fluids* **29**, 347–358.

Willis, K. D. & Orme, M. (2003) Binary droplet collisions in a vacuum environment: an experimental investigation on the role of viscosity. *Experiments in Fluids* **34**, 28–41.